

Dissertation
submitted to the
Combined Faculties for the Natural Sciences and for Mathematics
of the Ruperto-Carola University of Heidelberg, Germany
for the degree of
Doctor of Natural Sciences

presented by
Diplom-Physicist: Roland Krug
born in: Möhringen
Oral examination: 12. February 2003

**Determination of Aortic Elasticity
from MR- and CT- Images
Using an
Automatic Active Contour Model**

Referees: Prof. Dr. Dr. Christoph Cremer

Prof. Dr. Lothar Rudi Schad

Bestimmung der Elastizität der Aorta aus MR- und CT- Bildern mittels eines automatischen Active Contour Modells

Die Bestimmung der Aortenelastizität ist ein wichtiges Hilfsmittel zur frühzeitigen Diagnose von Arterienerkrankungen. Die Elastizität wird gewöhnlich über Compliance-Messungen quantifiziert, dabei wird die relative Änderung des Gefäßquerschnitts während des Herzzyklus oder die Pulswellengeschwindigkeit des Blutes bestimmt. In dieser Arbeit wurde die Compliance mit 3 MR Methoden (FLASH, TrueFISP und Pulse-wave) und zusätzlich im CT bestimmt. Es wurde ein Algorithmus entwickelt, der die Aortenwand aus MR- und CT- Bildern automatisch segmentiert. Kleine Änderungen des Aortenquerschnitts während der Herzphase konnten mit einem relativen Fehler von 1%, abhängig von der Bildqualität, sowohl im MR als auch CT bestimmt werden. Die Zuverlässigkeit des Algorithmus wurde an einem CT Phantomsetup getestet. Der Vergleich mit einer Threshold-Methode ergab für die Compliance eine Übereinstimmung von $0,5 \cdot 10^{-5} \text{ Pa}^{-1}$ im Confidenz-Interval bei einem Mittelwert von $C=3,0 \cdot 10^{-5} \text{ Pa}^{-1}$. Die Compliance Messungen an Probanden ergaben bei einer optimierten Zeitauflösung von 60ms einen relativen Fehler von 7% jeweils für TrueFISP ($1,0 \times 1,0 \times 10 \text{ mm}^3$, $\text{SNR} > 12$), FLASH ($0,7 \times 0,7 \times 10 \text{ mm}^3$, $\text{SNR} > 12$) und die CT-Messung ($0,39 \times 0,39 \times 10 \text{ mm}^3$, $\text{SNR} > 25$) und über 9% für die Pulswellenmessung. In einer Studie mit zehn Probanden wurden Werte zwischen $C=3 \cdot 10^{-5} \text{ Pa}^{-1}$ und $C=8 \cdot 10^{-5} \text{ Pa}^{-1}$ gefunden, je nach Alter des Probanden. Die beste Übereinstimmung der Messwerte zeigten die TrueFISP- und die Pulswellen-Methode (Confidence-Interval von $1 \cdot 10^{-5} \text{ Pa}^{-1}$). Für die FLASH Methode ergaben sich Werte von jeweils über $2 \cdot 10^{-5} \text{ Pa}^{-1}$. Eine Altersabhängigkeit der Aortenelastizität konnte sowohl im MR als auch im CT festgestellt werden.

Determination of Aortic Elasticity from MR- and CT- Images Using an Automatic Active Contour Model

The possibility to monitor changes in aortic elasticity in humans has important applications for clinical trials predicting arterial diseases before they become morphologically apparent. The elasticity is usually quantified by compliance measurements. Therefore, the relative temporal change in vessel cross-sectional area through the cardiac cycle or alternatively, the pulse-wave velocity has to be determined. In this work we determined the compliance via 3 MR methods (FLASH, TrueFISP and pulse-wave) and additionally CT. We developed an algorithm for the automatic segmentation of the artery wall from MR and CT images. Thus, the reliable detection of the aortic cross sectional area over the entire heart cycle was possible for both MR and CT with a relative error of about 1% depending on image quality. The reliability of the method was first evaluated by means of a CT phantom setup. The comparison to a threshold segmentation revealed an agreement of compliance of $0.5 \cdot 10^{-5} \text{ Pa}^{-1}$ (confidence-interval) at a mean value of $C=3.0 \cdot 10^{-5} \text{ Pa}^{-1}$. Optimizing the temporal resolution to 60ms we obtained a relative error of about 7% from TrueFISP- ($1.0 \times 1.0 \times 10 \text{ mm}^3$, $\text{SNR} > 12$), FLASH- ($0.7 \times 0.7 \times 10 \text{ mm}^3$, $\text{SNR} > 12$) and CT- ($0.39 \times 0.39 \times 10 \text{ mm}^3$, $\text{SNR} > 25$) measurements at volunteers. Pulse wave measurements yielded an error of more than 9%. In a study of ten volunteers, a compliance between $C=3 \cdot 10^{-5} \text{ Pa}^{-1}$ and $C=8 \cdot 10^{-5} \text{ Pa}^{-1}$ was determined, depending on age. The results of the TrueFISP and the pulse-wave measurements agreed very well (confidence interval of $1 \cdot 10^{-5} \text{ Pa}^{-1}$) while the results of the FLASH method more clearly deviated from TrueFISP and pulse-wave (confidence interval more than $2 \cdot 10^{-5} \text{ Pa}^{-1}$) An increasing in compliance with age could be found from MR and CT measurements.

Meinen Eltern

„Trennen und Zählen lag nicht in meiner Natur“

Johann Wolfgang von Goethe

Chapter 1 Table of Contents

INTRODUCTION	1
CHAPTER 1 FUNDAMENTALS	5
1.1 Physiological Principles	6
1.1.1 Cardiovascular Principles	6
1.1.2 Arterial Pulse Pressure and Elasticity	7
1.1.3 Cardiovascular Diseases Affecting Aortic Elasticity	9
1.1.4 Quantifying Elasticity	11
1.2 Physical Principles of Magnetic Resonance Imaging	14
1.2.1 Overview	14
1.2.2 Proton Spin and Magnetic Resonance	15
1.2.3 Spin Precession	18
1.2.4 Spin Relaxation	20
1.2.5 Image Reconstruction	23
1.3 Principles of Computed Tomography	26
1.3.1 Image Representation in CT	26
1.3.2 Principle of Image Acquisition	28
1.3.3 Hounsfield Scale	29
1.4 Principles of Digital Image Processing	32
1.4.1 Basic Concepts	33
1.4.2 Unitary Transforms	34
1.4.3 Linear Shift-Invariant Filters	35
1.4.4 Properties of LSI Operators	36
1.4.5 Data Processing Methods in MRI	37

CHAPTER 2 MATERIALS AND METHODS 43

2.1	Magnetic Resonance Imaging	44
2.1.1	MRI Hardware	44
2.1.2	Gradient Echo Sequences.....	45
2.1.3	FLASH and TrueFISP	48
2.1.4	ECG-Synchronization.....	49
2.2	Methods in CT	53
2.2.1	Technical Concepts.....	53
2.2.2	Spiral Computed Tomography.....	55
2.2.3	ECG-correlated Cardiac Imaging	56
2.3	Image Processing Techniques	58
2.3.1	Active Contours.....	58

CHAPTER 3 MEASUREMENTS AND RESULTS 63

3.1	Active Contour Algorithm.....	64
3.1.1	Development of an Active Contour Algorithm.....	64
3.1.2	Image Simulation.....	67
3.2	MR Measurements.....	71
3.2.1	Imaging Techniques.....	71
3.2.2	MR Image Acquisition	78
3.3	Determination of Aortic Compliance Using MRI.....	82
3.3.1	Automatic Image Segmentation of the Aortic Boundary	82
3.3.2	Determination of Aortic Cross Sectional Area.....	83
3.3.3	Determination of Aortic Compliance from Ten Healthy Volunteers	85
3.4	Results from CT Measurements	94
3.4.1	CT Measurements with Phantom Setup	94
3.4.2	CT Measurements with Patients	100

CHAPTER 4 DISCUSSION103**CHAPTER 5 SUMMARY AND OUTLOOK113**

LIST OF FIGURES	117
LIST OF TABLES	119
LIST OF REFERENCES	121
ACKNOWLEDGEMENT	127

Introduction

Recently, there has been a lot of progress in non-invasive imaging of the vascular system using Magnetic Resonance Imaging (MRI) and Multi-Slice Computed Tomography (MSCT). Although these methods allow to depict vessel anatomy very accurately, they do not provide information about the function of the vessel wall. One interesting parameter of the vessel wall is its elasticity. Elasticity of the aortic wall is an important functional parameter which is negatively correlated with hypertension, cardiovascular disease, as well as with age [32]. It is thus an adequate parameter to detect and monitor atherosclerotic heart disease [9]. The possibility of discovering early changes in vessel elasticity has important applications for clinical trials in estimating the efficiency of plaque-reducing therapies and for the study of pathogenesis of arteriosclerosis. For example, a decreased compliance of the aorta might be able to predict atherosclerotic changes before they become morphologically apparent, and might be useful in the characterization of aortic aneurysms.

The elasticity is usually quantified by compliance measurements where the relative temporal change of the aortic cross section through the cardiac cycle is divided by the blood pressure change in the vessel. However, the arterial compliance can be measured in two ways. First, by determining the pulse-wave velocity in the vessel using Doppler ultrasound [43] and MR techniques [29, 15, 16, 40, 45], where the compliance can be calculated directly from the velocity of the flow waves coming from the heart. Secondly, by measuring the change in cross-sectional area through the cardiac cycle, using imaging methods such as x-ray [24], magnetic resonance imaging [29, 8, 37] or ultrasound [14]. All these methods are non-invasive and do not require the use of contrast agent. Consequently they are ideal for studying healthy

subjects or asymptomatic patients in early stages of the disease. Furthermore, the aortic cross-sectional area can be measured from multi-slice CT (MSCT) based on retrospective multi-phase ECG-gating [6]. This CT method has the advantage that it can be easily integrated into a routine CT angiography study.

MR cross section measurements of the aorta are usually made by averaging images around the diastole and systole of the heart and outlining the aortic wall manually or with a semi-automatic technique [25]. Manually outlining the inner wall boundary is a very time-consuming process and is reliant on operator variability and bias. In this work, a method was developed for automated detection of the aortic boundary from MRI and CT images through the complete heart cycle, using advanced image analysis techniques based on active contours [23]. Active contours are a model based approach for feature segmentation, which considers prior knowledge of the resulting contour (e.g. smoothness and curvature) and posterior image information. This so-called ‘snake’ model was used and adapted to our problem.

The algorithm was first applied to simulated images with various signal-to-noise ratios. A further goal of this work was to acquire MR images during the entire heart cycle with sufficient spatial and temporal resolution. Although conventional spin-echo sequences deliver higher contrast between the endothelium and lumen, gradient-echo sequences have the advantage of recording images throughout the entire cardiac cycle. To obtain data ‘in-vivo’ a pilot study with 10 healthy volunteers was conducted. For each subject, vessel distension and cross section were recorded from retrospective ECG-gated MRI black and bright blood images. The compliance was then calculated from this data and blood pressure measurements. The results were then compared with the corresponding data obtained from pulse-wave velocity measurements at the same subjects.

Multi-slice CT compliance measurement has the advantage that morphological and functional information can be acquired at the same time using ECG-gated data acquisition during CT angiography. However, this method has not yet been applied

to compliance measurement. In this work we applied our contour algorithm to time-resolved CT images obtained from angiography measurements. An experimental validation of this method in a phantom setup is provided. Also, preliminary results of its application to patient data are presented.

Chapter 1

Fundamentals

In this chapter the principles of the methods applied in this work are presented. The first section gives a brief overview of the physiological basics and describes the cardiovascular system. Especially the importance of the elasticity of vessels, in particular of the aorta, is emphasized. Furthermore, cardiovascular diseases affecting changes in aortic elasticity are explained. The elasticity is quantified by compliance measurements. In principle, there are two different possibilities to obtain compliance. First by measuring the change in cross-sectional area through the cardiac cycle and secondly by determining the pulse-wave velocity in the vessel. Both methods are applied in this work with MR imaging. The first technique was additionally conducted by CT measurements.

In the second section of this chapter, the physical principles of MRI are discussed. Spin precession and relaxation processes are essential basic concepts of MRI. A short introduction to spin precession, relaxation and image reconstruction is given. More details can be found in [11] and [42]. Subsequently, basic concepts of CT are presented. A very detailed introduction to this subject can be found in [22].

The last paragraph of the chapter introduces basic concepts of image processing. In particular ‘linear shift invariant filters’ are discussed there. For more details in the field of digital image processing e.g. [19] can be recommended.

1.1 Physiological Principles

1.1.1 Cardiovascular Principles

The heart consists of four chambers. These are the left and right atrium and the left and right ventricle. The venous blood from the body to the heart is returned by the superior and inferior vena cavae. The right atrium receives this blood. It is a chamber with very high compliance so that it can accommodate the blood coming from the vein and maintain a pressure less than 3 mmHg. The actual pressure within the right atrium depends upon the compliance of the atrium and the blood volume within it.

Coming from the right atrium, the blood flows via the tricuspid valve into the right ventricle. From here the blood reaches the lungs across the pulmonary artery, which is separated from the ventricle by the semilunar pulmonic valve. Then it returns again to the heart, entering the left atrium via four pulmonary veins. Because the left atrium is quantitatively less compliant than the right atrium, the left atrial pressure is between 3 and 10 mmHg. Blood then flows via the mitral valve into the left ventricle. From the left ventricle the blood is ejected across the aortic valve into the aorta.

The aorta carries blood to the rest of the body. The part traveling through the chest is called the thoracic aorta. The part that travels through the abdomen, or stomach area, is called the abdominal aorta. In the lower abdomen the aorta splits into two arteries called the iliac arteries. Smaller arteries, like the renal arteries, branch off the aorta to carry blood to the kidneys and other organs.

1.1.2 Arterial Pulse Pressure and Elasticity

The arterial pulse pressure is defined as the difference between the systolic and diastolic arterial pressures. As blood is ejected into the aorta, the aortic pressure rises until the systolic pressure is attained. With the decrease of the ventricular outflow, the aortic pressure decays until the lowest pressure is reached just before the next ventricular ejection. This so-called diastolic pressure is determined by the systemic vascular resistance, the stroke volume and the heart rate.

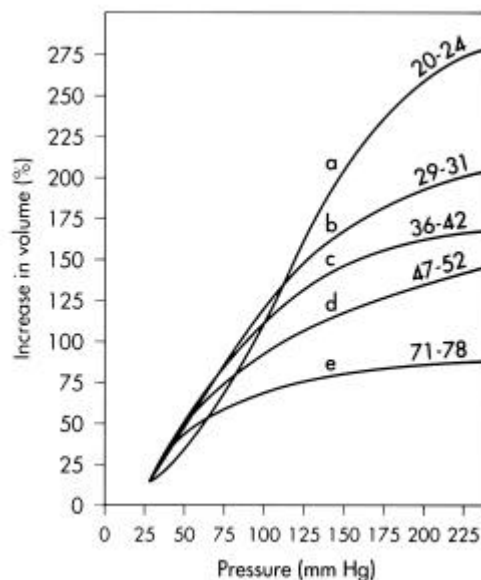


Fig. 1.1: Volume-pressure Relationship of the Aorta

The relationship between vessel volume and blood pressure for subjects of different age is shown. The slope is not linear because of the heterogeneity of the blood vessel tissue. Only in the physiological relevant section between 75-140 mm Hg, a linear relationship can be assumed. Also, a decrease in elasticity with age is discernible from the figure [13].

The difference in pressure between diastole and systole of the heart is determined by the elasticity of the aorta and the ventricular stroke volume. The maximum change in

aortic pressure represents the aortic pulse pressure. The aorta has the highest elasticity in the arterial system. This is partly due to a relatively high proportion of elastin fibers versus smooth muscle and collagen.

The aorta dampens the pulsatile output of the left ventricle and reduces thereby the pulse pressure. Assuming the aorta as a rigid tube, the pulse pressure would be very high. The walls of the aorta expand to accommodate the blood coming from the left ventricle of the heart. The more elastic the vessels are, the more blood from the systole can be stored in the aorta.

Hence, there is also a flow during diastole resulting in a more continuous blood flow [1]. Also, the more compliant the aorta, the smaller the pressure change during ventricular ejection. The slope of the volume-pressure relationship as shown in Fig. 1.1 determines the elasticity (compliance) of vessels. The curves reveal an important characteristic: Compliance decreases at higher pressure and volume. The vessel wall becomes stiffer.

However, Fig. 1.1 describes merely static compliance generated by expanding a vessel by a known volume. The change in pressure is then measured at steady-state. If the initial higher pressure is used instead of the steady-state pressure, the vessel will appear stiffer and compliance will be lower. Therefore, there is a dynamic component to compliance depending upon the rate by which the change in volume occurs.

Furthermore, it can be derived from Fig. 1.1 that aortic compliance decreases with age due to structural changes producing age-dependent increases in pulse pressure. For a given stroke volume a highly compliant aorta will have a smaller pulse pressure resulting in a smaller change between systolic and diastolic blood pressure.

The total flow of blood through a vessel element with length l and radius r can be quantified by the Hagen-Poiseuille equation as

$$\dot{V} = \frac{\mathbf{p} \cdot r^4}{8 \cdot \mathbf{h} \cdot l} \Delta p \quad (1.1)$$

where Δp is the decrease in blood pressure along the vessel element and \mathbf{h} depicts the viscosity of the blood. With this, a resistance can be defined as

$$R = \frac{\Delta p}{\dot{V}} = \frac{8 \cdot \mathbf{h} \cdot l}{\mathbf{p} \cdot r^4} . \quad (1.2)$$

Arteries with small radii and cross sectional areas lead to high resistance in blood flow. Therefore, the main difference in blood pressure occurs at small capillaries and arteries: The larger an artery, the lower the contribution to the entire blood resistance. For the aorta, the resistance can be neglected.

1.1.3 Cardiovascular Diseases Affecting Aortic Elasticity

Arteriosclerosis, the primary cause of myocardial infarction and most cerebral infarctions, is the leading cause of mortality and morbidity in the Western world [38]. Arteries may be affected by various diseases which change the elasticity of the aorta boundary. Thus, an early possibility to monitor changes in aortic elasticity as developed in this work has important impact on medical therapies. An overview is given in the following.

Aneurysm

A build-up of fatty materials in the blood vessel can form plaques on the aortic wall. Plaque destroys the elastic support of the artery wall. Cigarette smoking, high blood pressure and irritation of the artery wall can contribute to the weakening of the aorta

boundary. As a result, an aneurysm forms when a part of the thoracic or abdominal aorta weakens. Then the wall stretches and expands like a balloon. As a result, the aortic wall becomes thinner and weaker and a rupture is possible, causing massive internal bleeding which is a life threatening situation. Often, aortic aneurysms produce no symptoms until they rupture. It is a subject of current clinical research to investigate the relationship between aneurysm and change in compliance as a risk factor for it.

Stenosis

The terminus 'stenosis' refers to a critical narrowing of an artery. A stenosis can become critical when the radius of the aorta is reduced by at least half of its value. A radius reduction of more than 75 % significantly reduces blood flow, which can lead to chronic myocardial hypoxia. During the time blood is flowing through the valves, stenosis leads to a pressure gradient across the valve. The magnitude of this pressure gradient depends upon the severity of the stenosis and the flow rate across the valve. Aortic valve stenosis is characterized by the left ventricular pressure, which is much greater than aortic pressure during left ventricular ejection. The aortic pressure is slightly reduced. The pressure gradient across the stenotic lesion results from increased resistance and turbulence. Compensatory increase in end-diastolic volume and pressure will occur. Long-term consequences include hypertrophy and heart failure.

Marfan Syndrome

Marfan syndrome is a heritable disorder of connective tissue resulting in a highly variable degree of premature aortic medial degeneration and a high risk of subsequent dissection or rupture. Biophysical properties of the aorta as the compliance, may contribute to evaluate the risk for aortic rupture. Most mortality due to aortic rupture is related to aortic aneurysm.

Hypertension

High blood pressure (hypertension) is a leading cause of morbidity and mortality in the Western world. Hypertension can affect other organ systems of the body such as kidney, brain and eye. It is usually asymptomatic until its damaging effects (such as stroke, myocardial infarction, renal dysfunction, etc.) occur. Hypertension is often defined as a diastolic blood pressure over 90 mmHg or a systolic pressure over 140 mmHg. With most patients, the cause of their hypertension is unknown.

Ischemia and Hypoxia

Elasticity of the aortic wall is an important functional parameter which is negatively correlated with ischaemic heart disease. Ischemia is insufficient blood flow to provide adequate oxygenation. This always results in tissue hypoxia (reduced oxygen) or anoxia (absence of oxygen). The most common causes of ischemia are acute arterial thrombus formation and stenosis.

Ventricular Hypertrophy

Ventricular Hypertrophy means an increase of ventricular mass, the ventricle can become stiff and compliance is reduced. Ventricular Hypertrophy is an adaptation by the ventricle to increased stress, such as chronically increased volume load or increased pressure load. This adaptation can become pathological and ultimately lead to a deterioration in function.

1.1.4 Quantifying Elasticity

The ability of a blood vessel wall to expand and contract passively with changes in pressure constitutes an important function of large arteries and veins. This ability of a vessel to change the elasticity is quantified as the vessel compliance C . The elasticity

of a vessel is determined by the physical properties of the wall tissue and by the state of ventricular relaxation. Compliance is hence a measure of the elastic property of the artery. It may be thought of as the opposite of stiffness and a very stiff artery is said to have low compliance. In principle, there are two methods to determine compliance. Via cross sectional area measurement or via pulse-wave velocity measurement.

Cross Sectional Area Measurement

Compliance is determined by measuring the relative change in vessel cross-sectional area ΔA as the blood pressure pulsates during a heart cycle. With the systolic-diastolic change in blood pressure Δp and the aortic cross-sectional area A during diastole we can determine compliance [32] as

$$C = \frac{\Delta A}{A\Delta p}. \quad (1.3)$$

‘In vivo’, compliance is typically measured by using diagnostic imaging methods. The difference in blood pressure Δp is measured using sphygmomanometry directly at the subject. As the pressure pulse moves away from the heart the systolic pressure rises and the diastolic pressure falls. Due to the resistance of the arteries there is also a small decline in mean arterial pressure as the pressure pulse travels down the arteries. Therefore, a sphygmomanometer on the upper arm is used for arterial pressure measurement. The result will be slightly different than the real pressure in the aorta.

In literature, different methods for the calculation of compliance can be found. For example, in [37] compliance is defined as the change in vessel cross-sectional area ΔA divided by the difference in blood pressure Δp . Dividing then the result by the minimum of the aortic cross-sectional area A (diastole) results in the ‘aortic distensibility’ in [37] which is called ‘compliance’ in this work.

Pulse Wave Velocity Measurement

Another method to determine aortic compliance is based on pulse-wave velocity measurements. It is a rather indirect method. A characteristic for the blood flow in arteries is the pulsatile movement. To study the physical laws governing this pulsatile flow, the form and the propagation in the arterial system of both the pressure wave and the flow wave must be known.

The velocity of pulse-waves can be measured using MR methods [5]. If the vessel wall is completely stiff, the wave would propagate without delay. Since the wall of the aorta is elastic, the velocity of the pulse-wave is finite and can be measured. In order to obtain compliance from pulse-wave velocity measurements, the following approximation is used [40]:

$$C = \frac{1}{c^2 \rho}. \quad (1.4)$$

It involves the blood mass density ρ which can be assumed to be constant and the pulse-wave velocity c . The latter is determined by performing time-resolved MR phase-contrast flow measurements at different positions along the vessel and dividing the spatial distance Δx by the measured temporal delay Δt of the waves. The above relation is only valid for pulse-wave velocities much higher than the velocity of the blood, which we assume to be correct in our case.

1.2 Physical Principles of Magnetic Resonance Imaging

1.2.1 Overview

Magnetic resonance imaging (MRI) is a quite new physical application in medicine. It is based on the effect, that the spin of a hydrogen nucleus, the proton, precesses in a magnetic field about that field with the so-called ‘Larmor frequency’ ν_L . For a static field, the free precession is constant. The Larmor frequency depends linearly on the magnitude of the field itself. This property of the spin is used to locate an object in a spatially varying magnetic field. Such a field is called ‘magnetic field gradient’ and manipulates the spin orientation. The changes in orientation can then be measured through the interaction of the proton’s magnetic field with a coil detector.

In MRI, the resolution (less than one mm) in the images does not depend upon the transmitted wavelength of the rf-field (in the order of meters), as explained below. While atomic nuclei with an angular momentum $l \geq 1$ interact with both the electric and the magnetic component of the rf-pulse, protons with spin $\frac{1}{2}$ only interact with the magnetic component of the electromagnetic rf-pulse.

The main advantage of MRI lies in the sensitivity to a broad range of tissue properties such as the sensitivity to proton densities, relaxation times, temperature, proton motion and chemical shift. This large set of parameters determines the image contrast. In this section, a brief overview of the physical principles of MRI will be given (for more detail see [11, 42]). At the end of the chapter, spatial localization of the spins, frequency encoding and image reconstruction methods based on the Fourier transform will be discussed in detail.

1.2.2 Proton Spin and Magnetic Resonance

Living tissue consists of water in magnitude of about 60 % to 80 %. Thus, although other nuclei such as ^{23}Na and ^{31}P are also possible for imaging, the dominant nucleus used in MRI is the proton in hydrogen. All other nuclei are usually available in much lower concentrations. The proton has spin $\frac{1}{2}$ (^{23}Na has spin $\frac{3}{2}$ and ^{31}P has spin $\frac{1}{2}$) and all nuclei with an odd number of nucleons ($\frac{2}{3}$ of all stable nuclei) have a resulting spin I . A nucleus with an even number of protons and even numbers of neutrons has a total magnetic momentum of zero. (However, in general, the unpaired proton and neutron in odd-odd nuclei do not conspire to give zero spin).

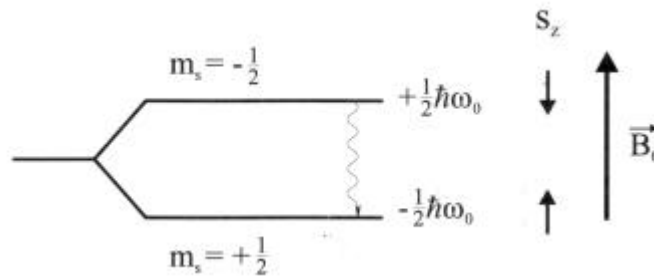


Fig. 1.2: Zeeman Energy Levels

In the lower energy state, the spin is parallel to the external field B_0 . The spin is anti parallel to the external field in the upper energy state. If the resonance condition is fulfilled, a rf-photon can induce transitions between the two energy states [11].

There is always a magnetic moment, which is proportional to the angular momentum I of the hydrogen proton,

$$\vec{m} = g \cdot \hbar \cdot \vec{I} = g \cdot \vec{J} \quad (1.5)$$

with $\hbar \equiv h/(2\pi) = 1.055 \cdot 10^{-34} \text{Ws}^2$ in terms of Planck's quantum constant h and the gyromagnetic ratio g . The proton has a g value of ca. $2.68 \cdot 10^8 \text{rad/s/Tesla}$ and is smaller for other nuclei. If an external magnetic field \vec{B} is applied on protons, they

align along the magnetic field lines and the magnetic moment \vec{m} yields to a potential energy, described by the Hamiltonian

$$H = -\vec{m} \cdot \vec{B}. \quad (1.6)$$

For the spin vector of the proton, only two discrete orientations relative to the magnetic field direction are allowed. Consequently, a discretization of the energy levels of the proton's magnetic moment interaction with the field \vec{B} is related. A measurement of the z component of the angular momentum \vec{J} leads to the expression $J_z = m \cdot \hbar$, where m are half-integer multiples in the case of the proton:

$$m = \pm \frac{1}{2} \Rightarrow \begin{array}{l} \text{spin parallel to field (lower energy)} \\ \text{spin anti-parallel (higher energy)} \end{array} \quad (1.7)$$

Thus, the magnetic moment is discretized with the magnetic quantum number m. If there is no outside interaction, each m value above is equally probable. Solving the Schrödinger equation we obtain discrete energy eigenvalues according to

$$E_m = -\hbar \cdot m \cdot B_z \quad (1.8)$$

assuming that $\vec{B} = B_z \cdot \vec{e}_z$. Considering the energy difference between the two energy states of the quantum system (Fig. 1.2), we find

$$\Delta E = \frac{1}{2} \cdot \mathbf{g} \cdot \hbar \cdot B_z + \frac{1}{2} \cdot \mathbf{g} \cdot \hbar \cdot B_z = \mathbf{g} \cdot \hbar \cdot B_z. \quad (1.9)$$

Hence, transitions are associated with the emission or absorption of photons with the frequency

$$\mathbf{v}_L = \mathbf{g} \cdot B_z. \quad (1.10)$$

Where \mathbf{v}_L is the so-called 'Larmor frequency'. In the classical description of the spin system, this frequency resembles the precession frequency of a proton in an external magnetic field (resonance condition). The precession frequency $f = \mathbf{v}_L / (2\pi)$

for protons is 42.6 MHz per one Tesla for resonance condition. For a 1.5 Tesla field, typically used in clinical MRI, the spins precess at a frequency of about 64 MHz. This implies a wavelength of the rf-pulse of more than 4.5 meters. The wavelength falls below 1 meter for higher magnetic fields above 7.0 Tesla.

In order to set the magnetization vector into precession, it must be tipped away from the external field direction. This is accomplished by applying a radiofrequency magnetic field for a short time perpendicular to the static field, a so-called 'rf-pulse', which is produced from a 'transmit' coil. Classically spoken, the magnetization vector is rotated away from its alignment along the longitudinal direction of B_0 . But again, it is important that the rf-pulse fulfills the mentioned resonance condition, i.e. it is tuned to the Larmor frequency. Only then does the precessing spin (in the classic description of the system) gain a continuously synchronized push in transversal direction.

To get spatial information from our sample, we can encode the spatial coordinates with spectral components, i.e. with different frequencies. Applying a spatially changing magnetic field by means of an additional linear gradient coil across the sample, we get a signal with spatially varying frequency components. It is then

$$\mathbf{v}(x) = \mathbf{g} \cdot B(x) \quad (1.11)$$

and the spatial information (here in x-direction) is encoded in the spectral variance. With this method applied in different directions, three-dimensional imaging can be realized, where the choice of any gradient direction is possible.

1.2.3 Spin Precession

In the presence of an external torque applied on the classical spin system, the total angular momentum \vec{N} changes according to $\vec{N} = d\vec{J}/dt$. Exercising a torque on a current loop in a constant magnetic field is given by $\vec{N} = \vec{m} \times \vec{B}$. With these results, we find the following fundamental equation

$$\frac{d\vec{m}}{dt} = \mathbf{g} \cdot \vec{m} \times \vec{B} \quad (1.12)$$

which describes the precession process.

We introduce now the local magnetic moment per unit volume, as the total magnetization of an ensemble of spins, with the same phase. We can then write for the magnetization vector \vec{M} :

$$\vec{M} = \frac{1}{V} \cdot \sum_{\substack{\text{protons} \\ \text{in } V}} \vec{m} \quad (1.13)$$

Neglecting the interaction of protons with their environment, we obtain the temporal evolution of the magnetization as

$$\frac{d\vec{M}}{dt} = \mathbf{g} \cdot \vec{M} \times \vec{B} . \quad (1.14)$$

The solution of this equation is a precession of the magnetization around the constant magnetic field B_0 with the Larmor frequency. We assume now that the precession takes place at a small angle around the static field direction. We now apply an additional magnetic field B_1 perpendicular to the static field and synchronized with the Larmor frequency. This field, tips the spin down to a larger angle as seen in Fig. 1.3. Let B_1 be linearly polarized along the x-axis in a rotating (with ω_F)

reference frame denoted by primed quantities (x',y',z'). Equation (1.14) changes then to transforms:

$$\frac{d\vec{M}'}{dt} = \mathbf{g} \cdot \vec{M}' \times \begin{bmatrix} B_1 \\ 0 \\ B_0 - \frac{V_{rf}}{\mathbf{g}} \end{bmatrix} \quad (1.15)$$

If the rf-pulse frequency is equal to the Larmor frequency, there is only a precession of the magnetization about the rotating x' -axis. Its magnitude and z -component are fixed, but the direction in the x - y -plane is changing.

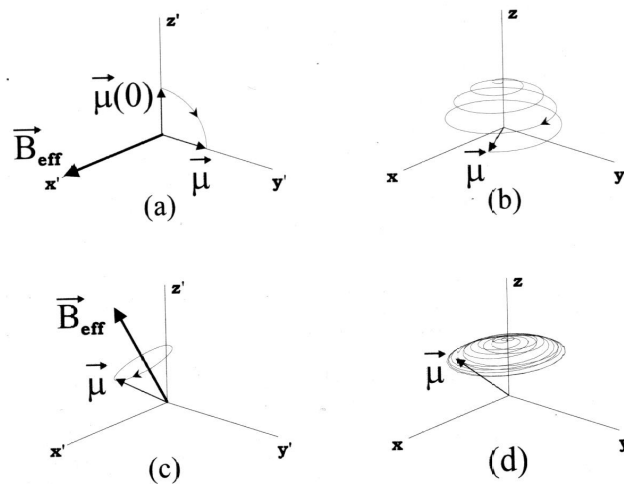


Fig. 1.3: On-resonance Spin Flip

The longitudinal magnetic moment $\vec{\mu}$ is tipped in the transversal direction by a $\pi/2$ rf-pulse. This is shown in the rotating frame (a) as a pure rotation about the x' axis and in the laboratory (b) frame as a downwards spiral. If the resonance condition is not fulfilled, a precession about the total magnetic field takes place (c). In the laboratory frame, the resulting movement is a superposition of this precession with the rotation of the frame as shown in (d) [11].

Thus, the angle α between magnetization and z -axis changes temporally like $\alpha = \mathbf{g} \cdot B_1 \cdot t$. Only if B_1 is applied for a finite time, it is called a rf-pulse. To get a

flip angle, that is $\alpha = 90^\circ$, a magnitude of $B_1 = 5.9 \text{ mT}$ is required over 1.0 ms time. In the semi-classic model, only transitions between the two allowed spin states take place during the rf-pulse. To get a 90° transversal magnetization, the two energy states of the spin system have to be equally occupied. To invert the magnetization vector by a 180° -pulse, the higher energy state of the spin system has to be predominant. Hence, a macroscopic transversal magnetization equal to the magnitude of the longitudinal magnetization is possible.

1.2.4 Spin Relaxation

So far, the interactions of the proton spin with its surrounding atoms, like the exchange of energy and the change in spin precession frequency due to local fields, were not considered. First, we consider the longitudinal relaxation. After tipping the magnetization with a rf-pulse to a certain flip-angle, the longitudinal magnetization returns to its equilibrium value M_0 . This is due to the interactions of the spins with their surroundings, the so-called ‘spin-lattice interactions’. The time rate of regrowth (the spin-lattice relaxation time) is determined by T1 (Fig. 1.4)

The equilibrium depends on the absolute temperature T and the external field, described by Curie’s law for $\hbar \nu_0 \ll kT$ (where $k = 1.38 \cdot 10^{-23} \text{ Joule / K}$ is Boltzmann’s constant):

$$M_0 = C \cdot \frac{B_0}{T} \quad \text{with} \quad C = \frac{N}{V} \cdot \frac{I(I+1)g^2\hbar^2}{3k_B} \quad (1.16)$$

with N as the total number of magnetic moments in a sample volume V . The quotient N/V is also called the spin density ρ . At room temperature, only a very small part of spins parallel to B_0 exceed anti-parallel spins.

For a typical field strength of 1.5 Tesla, there are about five in one million excess parallel spins, which is already a considerable amount in the order of 10^{19} spins in

one mole of water. The resulting Bloch equation receives an additional term, considering the relaxation effects:

$$\frac{dM_z}{dt} = \mathbf{g} \cdot (\vec{M} \times \vec{B})_z + \frac{M_0 - M_z}{T_1} \quad (1.17)$$

Now we consider the transverse decay of the magnetization due to spin-spin interaction. Local magnetic field fluctuations make that the spins experience different field strength and thus precess at different Larmor frequencies.

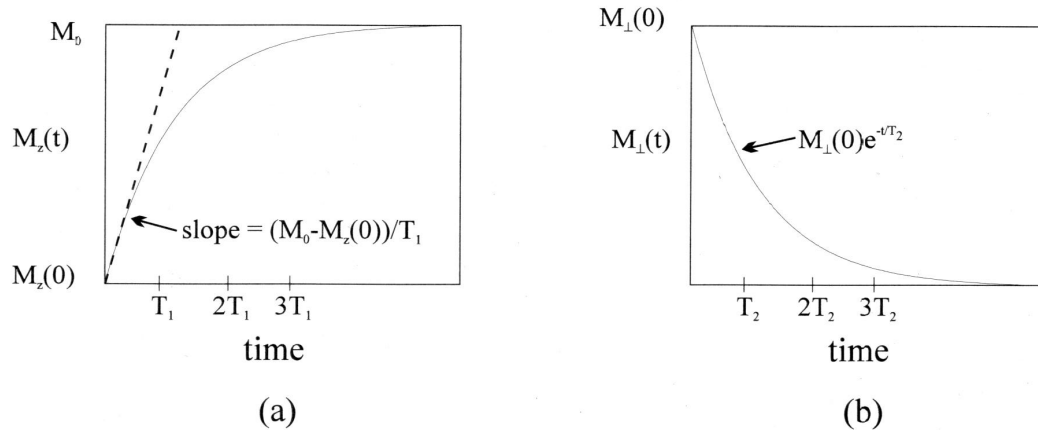


Fig. 1.4: Spin Relaxation Process

Picture (a) demonstrates the regrowth of the longitudinal magnetization to the initial equilibrium and is described by the time scales T_1 , which is empirically determined. The transversal magnetization decays during the time scales T_2 as seen in (b). The intrinsic losses in phase coherence are not recoverable and are related to local time-dependent field variations [11].

These field fluctuations stem from the superposition of the applied magnetic field and the field of the surrounding spins. Hence, the spins lose their coherence in phase and dephase with the spin-spin relaxation time T_2 (Fig. 1.4). This fanning out of clusters of spins is accompanied by a reduction of the transverse magnetization.

The Bloch equation now becomes:

$$\frac{dM_{\perp}}{dt} = \mathbf{g} \cdot (\vec{M} \times \vec{B})_{\perp} - \frac{M_{\perp}}{T2} \quad (1.18)$$

This is only correct for a perfectly homogenous B_0 field. In reality, a much faster decay of signal is observed due to field inhomogeneities of the B_0 field and $T2$ is replaced by the smaller relaxation time $T2^*$:

$$\frac{1}{T2^*} = \frac{1}{T2} + \mathbf{g} \cdot \Delta B_0. \quad (1.19)$$

Since these static inhomogeneities described by ΔB_0 do not fluctuate statistically, this dephasing effect can be reversed by rephasing the spins. This is achieved by applying an additional 180° rf-pulse.

Table 1.1: Relaxation Parameters

Approximate relaxation parameters $T1$ and $T2$ in milliseconds for different human tissues at a static magnetic field of $B_0 = 1,5$ T and a temperature of 37°C [36, 11].

Tissue	T1 (ms)	T2 (ms)
Gray matter	950	100
White matter	600	80
Skeleton muscle	900	50
Cerebrospinal fluid (CSF)	4500	2200
Fat	250	60
Blood (arterial)	1200	100
Blood (venous)	1200	200

With this so-called spin-echo method, a refocusing of the spins takes place and an echo-signal occurs at the echo time TE. All these relaxation processes can phenomenological be described in one equation:

$$M_z(t) = M_0 \left(1 - e^{-TR/T1}\right) \cdot e^{-TE/T2} \quad (1.20)$$

where TR is the time between two successive rf-pulses where relaxation can take place, and TE is the echo time. Both, the regrowth of longitudinal magnetization to its equilibrium M_0 , as well as the decay of the transversal component, display an exponential form.

1.2.5 Image Reconstruction

To obtain spatial information of our subject, we have to encode the spins in the spatial directions. Since the Larmor frequency of the spins depends linearly on the magnitude of the applied magnetic field, it is possible to locate the spins in a spatially varying field because of their different precession frequency. The so-called 'linear magnetic field gradient' (G_x, G_y, G_z) is superimposed to the static field. Then, the Larmor frequency of the spin depends linearly on its position.

Slice Selection

First we select a two-dimensional slice from the object

$$\nu_L(z) = \mathbf{g} \cdot (B_0 + z \cdot G_z) \quad (1.21)$$

where the spatially constant gradient in z-direction $G_z \equiv \partial B_z / \partial z$ is called slice selection gradient. Thus, only the spins with frequency ν_L are stimulated by the rf-pulse. To compensate the deviation from Larmor frequency at the extremities of the slice selection gradient, the gradient is turned 180° after the rf-pulse. Hence, after half of the excitation time, the spins rephase again.

Read-Out Direction

Now all spins in the selected slice precess with the same Larmor frequency in the static B_0 -field. With an additional field gradient along the x -axis, the Larmor frequency is unambiguously related to the spatial information in x -direction through

$$\mathbf{v}_L(x) = \mathbf{g} \cdot (B_0 + x \cdot G_x) \quad (1.22)$$

This relation between the spatial position of the spins and their precessional frequency is called ‘frequency encoding’. The signal is detected while the so-called ‘read-out’ gradient is applied. The accumulated phase up to a time t is given by:

$$\mathbf{f}_G(x, t) = -\mathbf{g} \cdot x \int_0^t G_x(t') \cdot dt' = k_x \cdot x \quad (1.23)$$

and due to the field gradient. This means that in the middle of the sample where the magnetic field gradient is zero, there is no additional phase accumulation. Hence, the spins’ position is labeled by the accumulated phase ϕ . In practice, the total resulting signal is sampled in discrete time steps Δt during the acquisition time. During this time, the spins continue precessing with different Larmor frequencies and thus accumulating different phases ϕ .

Phase-Encoding Direction

To encode the missing y -direction, a further but varying magnetic field gradient G_y is applied before reading out the signal. The phase is getting an additional shift, according to the gradient strength and the duration time of the gradient

$$\Delta \mathbf{f}_{(y)} = \mathbf{g} \cdot \Delta G_y \cdot t_y \cdot y = \Delta k_y \cdot y \quad (1.24)$$

After switching off the so-called ‘phase encoding gradient’, all spins continue precessing with the initial Larmor frequencies. But the phase has accumulated space depending values. These values are related to the basic functions of the discrete

Fourier transformation, as we will see in the next chapter. With the k-components $k_y = \mathbf{g} \cdot G_y \cdot t_y$ and $k_x = \mathbf{g} \cdot G_x \cdot t_x$ resulting from equation(1.24), all the basic vectors in the Fourier transform can be depicted during read-out. The total time depending complex signal is thus

$$s(t) \propto \int M_T(x, y) e^{ik_x x} e^{ik_y y} dx dy \quad (1.25)$$

and will be sampled in defined time steps by the coil detector. Resulting from this time sampling, we get the spatial resolution via

$$\Delta x = \frac{2p}{k_{\max}} = \frac{2p}{\mathbf{g} \cdot G_x \cdot N \cdot \Delta t} \quad (1.26)$$

for every read-out step in x-direction.

1.3 Principles of Computed Tomography

The discovery of x-rays by Professor Wilhelm Conrad Röntgen 1895 was the beginning of a new era in medicine. For the first time it was possible to obtain images of the inside of the human body. The main disadvantage of the conventional x-ray technique is its limitation due to the two dimensional projection of the human body. The third dimension is not considered, and hence a part of the information is lost on the recorded image. This problem has been resolved with the technique of x ray computed tomography.

The first realization of this concept was conducted by A.M. Cormack and later G.N. Hounsfield [17], who is now generally recognized as the inventor of computed tomography. Both scientists were awarded the Nobel Prize for medicine in recognition for their outstanding achievements.

1.3.1 Image Representation in CT

With Computer tomography (CT) it was possible for the first time to image slices through the human body instead of superposition images of complete body sections. It has replaced classical x-ray imaging in many fields in medicine diagnostic. CT first became feasible with the development of modern computer technology.

However, the principle idea of image reconstruction in CT was already published in 1917 by the bohemian mathematician J. H. Radon [35]. He proved that a layer of an object can be reconstructed from integral values along any number of lines passing through the same layer.

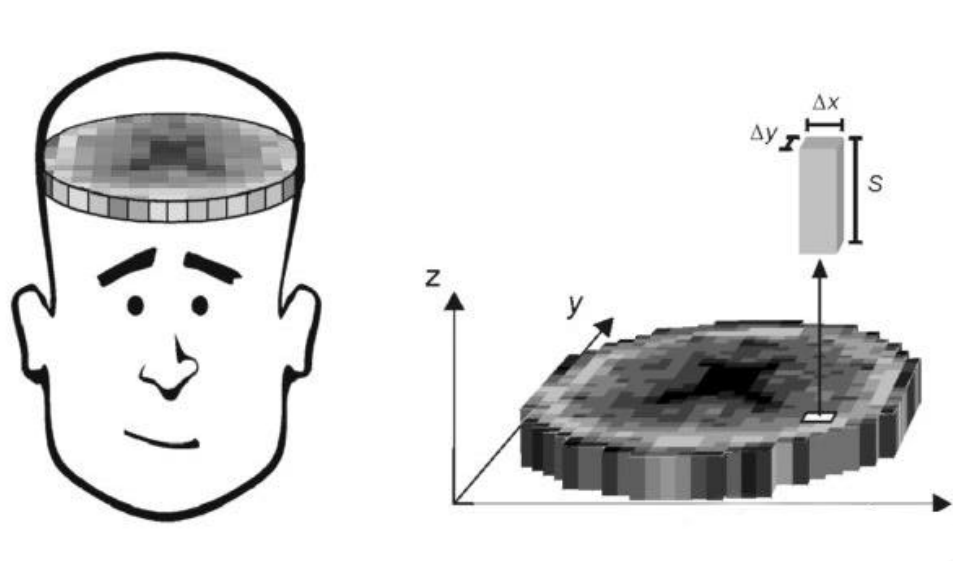


Fig. 1.5: Computed Tomography

A transverse slice of the human body (e.g. here the head) can be acquired in discrete digital form. The resulting image consists of discrete voxels representing the magnitude of attenuation of x-rays in the human body [22].

To understand computed tomography we can view the human body to be built up by a finite number of discrete slices and volume elements as seen in Fig. 1.5. Each volume element (voxel) represents the linear attenuation coefficient of the x-rays at a certain position in the body. Thus, the spatial distribution of the linear attenuation coefficient of different tissue in the human body is projected. The voxel size is determined by the selected matrix size, the slice thickness and the field of view. In computed tomography, a matrix size of 512×512 is common.

1.3.2 Principle of Image Acquisition

To calculate the attenuation value along every x-ray in CT, the attenuated intensity I and the primary intensity I_0 have to be measured. The intensity falls off exponentially with absorber thickness. The attenuation is then given as the product of the linear attenuation coefficient μ and the absorber thickness d . The distribution of μ along the ray path is normally not known. The two-dimensional distribution of an object can be determined from a finite number of line integrals over μ along the ray path.

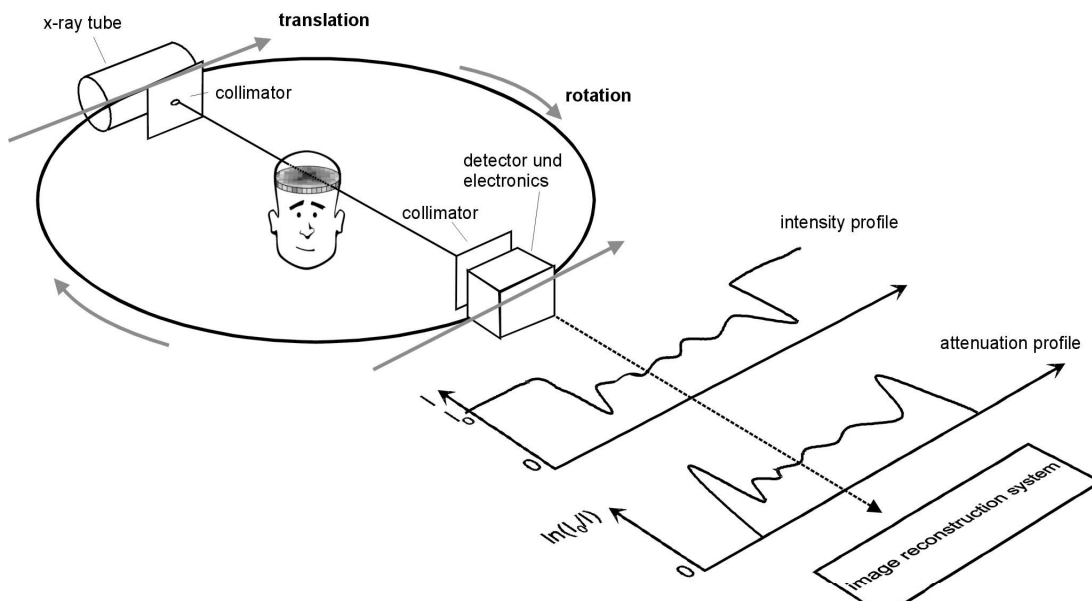


Fig. 1.6: CT Measurement Setup

Object attenuation measurements for different angular positions. A pencil beam samples the object along the ray paths. The resulting intensity after attenuation is registered by the collimator which is placed opposite [22].

The linear attenuation coefficient also depends strongly on energy. This has to be considered when integrating over the ray path. Furthermore, a dependence on time can be provoked e.g. by contrast media.

Considering all dependencies, we get $\mathbf{m}(x, y, z, E, t)$ for the attenuation coefficient. In the simple case of measuring \mathbf{m} for a given slice position z , we can write for the attenuation of the intensity

$$I = I_0 \cdot \exp\left(-\int \mathbf{m}(x, y) ds\right) \quad (1.27)$$

over one ray path, where $\mathbf{m}(x, y)$ is the local linear attenuation coefficient. From the measured intensity value I and the primary intensity I_0 , we can get a projection of the attenuation coefficients $\mathbf{m}(x, y)$ as

$$-\ln\left(\frac{I}{I_0}\right) = \int \mathbf{m}(x, y) ds. \quad (1.28)$$

Having obtained all projections, the spatial distribution of the attenuation coefficients can be reconstructed [35] and the CT image can be depicted.

To record a CT image with high quality, a sufficient number of projections in all directions has to be conducted as shown in Fig. 1.6. An angular range of at least 180° degree is necessary to obtain all information from the object. The object is scanned by a pencil beam emitted from a radiation source with adequate collimation. A detector placed opposite registers the intensity coming from the object. In the same way, several projections are measured for different angular positions. Normally a range of 360° is applied today. Modern CT scanners typically measure 800-1500 projections with 600-1200 data points per projection.

1.3.3 Hounsfield Scale

Since the spatial distribution of the linear attenuation coefficients is not very descriptive and strongly dependent on the spectral energy, the so-called Hounsfield scale is used to display the image. In order to make it possible to compare images from different scanners with different voltages, the coefficient values are displayed

relative to the attenuation coefficient m_w of water (Fig. 1.7). These so-called Hounsfield units are defined as follow:

$$H = 1000 \cdot \left(\frac{m}{m_w} - 1 \right) \quad (1.29)$$

Hence, water and water-equivalent tissue have the Hounsfield value of 0 HU by definition. Since the attenuation coefficient of air is nearby equal to zero, the Hounsfield value of air is -1000 HU. These two values are independent of the x-ray energy they constitute the fixed points for the Hounsfield scale.

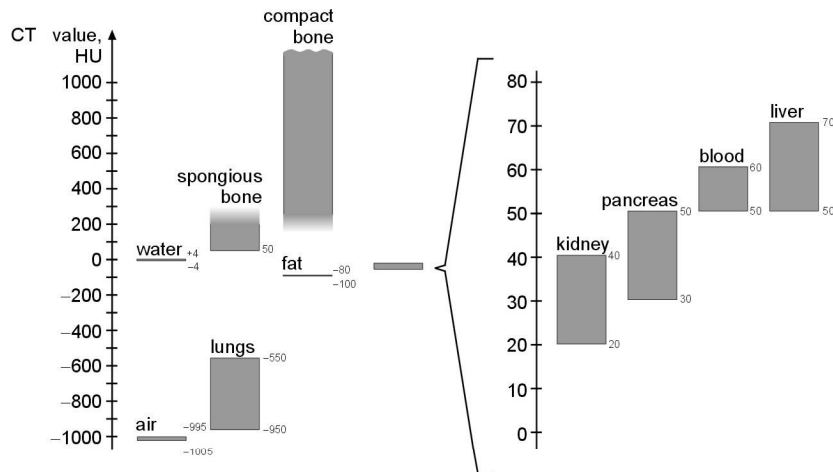


Fig. 1.7: The Hounsfield Scale

The attenuation coefficient value of water is defined as zero. Lung tissue and fat exhibit negative Hounsfield values. Whereas most other tissues as muscle, soft tissues and bone exhibit positive CT values [22].

Lung and fat tissue exhibit negative attenuation coefficients because of lower tissue density. Whereas higher effective atomic number of calcium, bone and calcifications make the Hounsfield value increase considerably up to 2000 HU. However, the Hounsfield scale has no upper limit. On CT scanners, a typical range from -1024 HU to $+3071$ is provided today. Hence, 4096 (12 bit) gray values are required to store the image. Since the human eye can only discern between 60 to 80 gray values, the

levels have to be windowed to a interval of interest. The window must be adapted according to the tissue to record. To display small attenuation differences as in the brain, a narrow window is required. For lung and skeleton acquisition, a wide window is better as shown in Fig. 1.8.

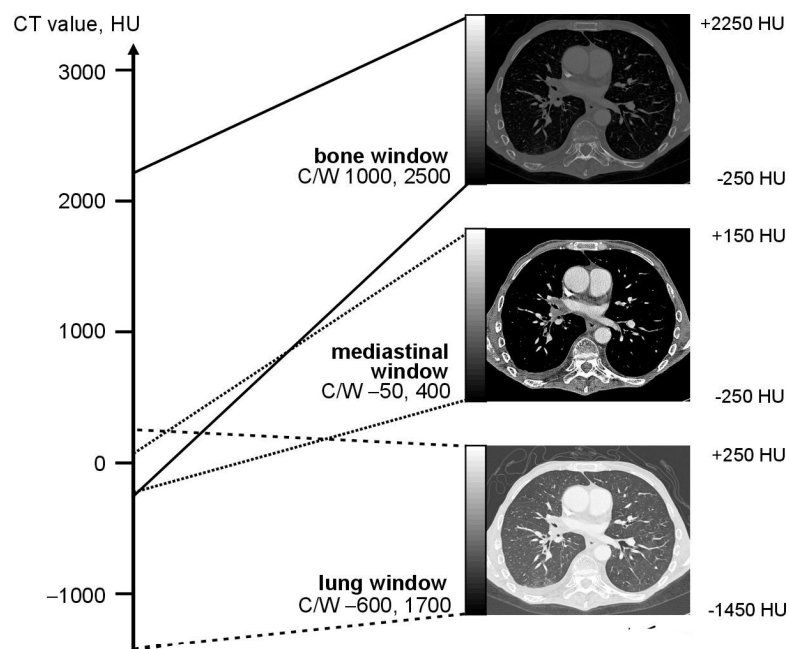


Fig. 1.8: Windowing of CT Hounsfield Values

By choosing the center and width of the window, the relevant image information can be amplified. Since human beings can only discern about 80 gray levels but a CT image consist of 4096 gray levels, there is much more information hidden in the entire CT image. This information can be visualized by changing the visualization window [22].

1.4 Principles of Digital Image Processing

In the last years the applications of digital image processing in medicine have increased at a tremendous rate. In conventional diagnostics, the data coming from the acquisition device is perceived by the physician and is interpreted with the help of a large amount of 'a priori' knowledge to give a diagnostic finding. During the last years, a steadily rising number of attempts have been made to support this process by the application of computers.

Today a large part of information about the patient is drawn from image data which are represented in a digital form. In modern medicine, digital imaging has become a crucial method for diagnostics and therapy. Therefore, image processing is a very important tool to extract information from the measured data. In this way a wide range of new possibilities in medical diagnosis and therapy was found.

Because of the integration of different techniques such as image analysis, texture recognition and visualization, a large number of new methods could be established. In the first part of this chapter, some basic definitions and approaches will be given to become familiar with the notation used in digital image processing. Then the Fourier transform will be introduced, which is of paramount importance for MRI and image processing in general. Thirdly, neighborhood operations, as well as the powerful concept of linear shift-invariant operations are discussed (for a deeper study see e.g. [19]).

1.4.1 Basic Concepts

Images can be thought of as a spatial distribution of gray values within a plane. A digital image with two dimensions $M \times N$ can be described as a function

$$f : \underline{M} \times \underline{N} \rightarrow \underline{G} \quad (1.30)$$

where in medical images a set of $g = 12$ bit (thus 4096 gray values) is common with $g \in G$. As these images are digitized, the elements $m \in \underline{M}$ and $n \in \underline{N}$ are discrete variables of the function $f(m, n) = g$. In CT, the image elements m and n usually have values from 0 to 512, whereas in MR (magnetic resonance), a range of 256×256 is a more common choice. Digital images are thus represented as two-dimensional arrays of points or pixels (picture elements). On a rectangular grid, which is the simplest and most common representation to locate a pixel, the matrix notation is used for the image array. The result is that m denotes the position of the row from top to bottom and n the position of the column from left to right. This approach can be easily expanded to three and more dimensions. For a three dimensional scene, the expression 'voxel' (volume element) is used to denote an element of the 3D grid. Although three lattices with regular polygons are possible (triangular, square and hexagonal grid), almost exclusively square lattices are used.

Basic concepts of image processing include the important Low-Level Transformations. These transformations are described by operators which self-transform the image within the spatial representation. We can distinguish three cases of self-transformation. The simple homogenous point operators, depending only on the gray value at the same position of source and target image. This can be performed very easily by means of Look-Up-Tables (LUT), for which of every discrete pixel value g the corresponding value is stored. This is applied very often in medicine, e.g. to stretch acquired gray values to a new gray value window (histogram

stretching) or to assign pseudo color values to an image. Thus, diagnostic interpretations of medical images can be improved (see also Fig. 1.8).

Another self-transformation is performed by global operations. In this case, for every pixel of the target image all pixels from the source image have to be considered. If only a part of the source image is used, we speak of a local operation. These neighborhood operations can be described as filtering the image with a so-called filter mask and will be explained in more detail below.

Up to now, all image transformations are described in a spatial system, where the result of these operations can be directly seen and understood. However, the information inherent in an image can be depicted in different ways, though less illustrative for our perception. One alternative image representation is the wave number or Fourier representation. Spatial and Fourier representation can be converted into each other without loss of information. They are both totally equivalent descriptions of a digital image and are transformed via the well-known Fourier transform (FT). In particular, in MRI the FT plays an important role in image reconstruction.

1.4.2 Unitary Transforms

Unitary transformations are defined for vector spaces over the field of complex numbers, for which an inner product is defined. If a coordinate transform preserves the inner product, the length and the orthogonality of the image vector is also preserved. The Fourier transform is an example of a unitary transform.

The discrete Fourier transform DFT for the one-dimensional vectors g and \hat{g} is defined as

$$\hat{g}_u = \frac{1}{\sqrt{N}} \cdot \sum_{n=0}^{N-1} g_n \cdot \exp\left(-\frac{2\pi i n u}{N}\right), \quad 0 \leq u \leq N \quad (1.31)$$

when g is the following N-dimensional complex-valued vector $g = [g_0, g_1, \dots, g_{N-1}]^T$.

The advantage of the Fourier transform is the fact that if a signal is shifted in space, its Fourier transform is only multiplied with a complex phase factor (shift theorem). All base functions of the FT are eigenvectors of the shift operator [18], as pointed out in the following:

$$O(s) \exp(-2\pi i k x) = \exp(-2\pi i k s) \exp(-2\pi i k x) \quad (1.32)$$

The phase factor $\exp(-2\pi i k s)$ is the eigenvalue of the shift operator $O(s)$. The complex exponentials $\exp(-2\pi i k x)$ are the base functions of the Fourier transform. They are the eigenfunctions of all linear shift-invariant operators or convolution operators. Thus, a convolution operator applied to a periodic signal also changes only the phase and amplitude of this signal. Such a complex factor is the wave number dependent eigenvalue or transfer function of the convolution operator.

1.4.3 Linear Shift-Invariant Filters

Neighborhood operations combine the picture elements of a small neighborhood in a certain way, forming a new image. They extract a certain feature of interest from the image and are therefore also called image filters. Characteristic for such an operation is the size of the operator mask and the position of the pixel receiving the result. Linear and shift-invariant filters are of paramount importance for low level image processing. It can be proven [20] that a linear shift-invariant operation must necessarily be a convolution operation in space domain. Only a convolution operator is both linear and shift-invariant.

Shift-invariant operators deliver a response that does not explicitly depend on their position. Thus, the output of a shifted signal is the same but shifted. An operator that is both linear and shift-invariant is called an LSI operator or LTI (linear time-invariant) operator for time series. For an LSI filter H with a nonzero odd-sized coefficient mask $(2R+1) \times (2R+1)$, the convolution with a two-dimensional image G can be written introducing the convolution operator ‘*’:

$$G'_{mn} = \sum_{m'=-R}^R \sum_{n'=-R}^R H_{m',n'} G_{m-m',n-n'} = H * G. \quad (1.33)$$

1.4.4 Properties of LSI Operators

Assuming that G_1 and G_2 are two complex-valued images, a and b are two complex-valued scalars and T is a transformation operator which transforms the images. Let T be a LSI operator, then the following important properties are valid:

The principle of Linearity. A system is linear, if the principle of superposition is fulfilled. Let G_1 and G_2 be images, then $aG_1 + bG_2$ is also an image and it is

$$T(aG_1 + bG_2) = aT(G_1) + bT(G_2). \quad (1.34)$$

The principle of Distributivity over addition. Two linear local operators T_1 and T_2 can be summarized by adding up the matrices:

$$(T_1 + T_2)(G) = T_1(G) + T_2(G) \quad (1.35)$$

The principle of Associativity. For two local linear operators T_1 and T_2 , there is always a local operator T and it is

$$T(G) = T_1(T_2(G)). \quad (1.36)$$

Because of associativity, every complex operator can be composed of several more simple operators. This property of LSI operators increases efficiency and speed of

implemented algorithms. The matrix corresponding to the operator T results from a convolution of the matrices corresponding to the operators T_1 and T_2 . Because of this associativity, a complex operator can be composed out of more simple operators. Thus, efficiency and speed of the algorithm can be achieved.

The principle of Commutativity. The commutativity of convolution operators can easily be shown in Fourier domain, where the operation is reduced to a simple multiplication. Thus, the order in which LSI operators are applied to an image is of no importance to the resulting image:

$$T_1(T_2(G)) = T_2(T_1(G)). \quad (1.37)$$

With this concept, also the principles of imaging can be treated as an LSI system. This leads us to the notion of the point spread function (PSF), which describes the imaging of a point and thus the complete imaging system. In case of image formation, the PSF smears an image and thus reduces the resolution. Its Fourier transform is known as the optical transfer function OTF. Convolution with the PSF in the space domain translates to multiplication with the OTF in Fourier space.

1.4.5 Data Processing Methods in MRI

In this section basic image processing methods especially important for MRI are discussed. The continuous signal induced by the transversal magnetization and detected in the receive coil must be sampled and truncated. Effects such as aliasing and phase imaging must be carefully considered when reconstructing the image

Sampling and Aliasing

The MR signal is generally recorded over a uniformly spaced grid in k-space. The sampling function is a grid of even spaced delta functions laid across the continuous signal. The sampled image is thus the product of the so-called 2D δ comb (bed-of-

nails function) and the image. Hence, the result is zero, except at the points where the data was sampled. Considering only one dimension, the sampling function can be written as

$$f(k) = f(k) \cdot \sum_{m=-\infty}^{+\infty} \mathbf{d}(k - m\Delta k), \quad (1.38)$$

with a generic constant spacing Δk . The inverse 1D Fourier transform is given by

$$F(x) = \sum_{n=-\infty}^{+\infty} \mathbf{d}(x - n / \Delta k) \quad (1.39)$$

and is also a sampling function. In order to better understand the sampling process and to become familiar with the aliasing problem, a closer look at the discrete Fourier Transform is helpful. We consider a one-dimensional signal $G(x)$ which is sampled at discrete points Δx . Then we have a discrete signal $G(x) \rightarrow G_n$ with $x = n \cdot \Delta x$. The complex basis functions of the discrete Fourier transform are sampled sine and cosine functions of different wavelengths:

$$g(k) = \sum_{n=-\infty}^{+\infty} G_n \exp(-ikn\Delta x) = \sum_{n=-\infty}^{+\infty} G_n \exp\left[-in \Delta x \left(k + \frac{2\mathbf{p}}{\Delta x}\right)\right]. \quad (1.40)$$

We therefore get a periodic structure with the following repetition period:

$$g(k) = g\left(k + \frac{2\mathbf{p}}{\Delta x}\right). \quad (1.41)$$

It is thus sufficient to limit the k -values from $k = 0$ to $k_{\max} = 2\mathbf{p} / \Delta x$. Vice versa, sampling in the Fourier space results in a band-limited function $G(x)$ with $x_{\max} = 2\mathbf{p} / \Delta k$. In practice we can of course only handle finite image matrices. The conclusion to be drawn from this paragraph is that the scales in space and wave number domain are reciprocal to each other.

To reconstruct an image without losing information or getting distortion of the signal we must restrict the maximum wave number k_{\max} of the image to less than half of the grid constants Δk of our bed-of-nails function. This fact is known as the ‘sampling theorem’ and is equal to a restriction of the first Brillouin zone around the central grid point of our sampling function. If the spectrum of the image does not match the first Brillouin zone, it overlaps with its periodically repeated copies. Hence, it is not possible to assign the overlapping parts to the image or a copy of it. The maximum wave-length that can be sampled without errors lies at the border of the first Brillouin zone and is called the Nyquist wave number. Aliasing effects distort the image due to a back shift of the k-vectors outside the first Brillouin zone. These vectors appear in the first Brillouin zone at the same position as in the copy. Thus, they do not only have different wavelength, but also another direction. They differ from their true wave number by a grid translation vector on the reciprocal grid.

Field of View

Since we are only able to use finite image matrices, we must limit the window to a finite window size or ‘field of view’. This restriction can be viewed as a multiplication of the sampled image with a box function. This corresponds to a convolution in Fourier space with a so-called 2D sinc function resulting in a reduction of the wave number resolution in the spectrum of about half-width of this sinc function.

In MRI, the signal is generally collected along the read direction by taking data at uniform intervals Δt in time. This results in a uniformly spaced k-space sampling with the resolution $\Delta k = \mathbf{g}G_R \Delta t$ and the measured signal $s(n\Delta k)$. The magnetization gradient G_R does not have to be confused with the complex-valued images G_1 and G_2 .

This leads to a band-limited spin density $\hat{\mathbf{r}}(r)$ in the space domain, which is not to be confused with the original image spin density $\mathbf{r}(r)$ (see also next paragraph). Considering only one dimension, the now reconstructed (using the discrete Fourier transform) spin density for finite sampling is

$$\hat{\mathbf{r}}(x) = \hat{\mathbf{r}}\left(x + \frac{2\mathbf{p}}{\Delta k}\right), \quad (1.42)$$

with a field of view (FOV) of $L = 2\mathbf{p} / \Delta k$ in one dimension. This is the spatial interval over which the reconstructed image repeats over the entire space domain. To avoid aliasing, the object has to fit the FOV. If there are overlaps, it means that the rf-coil picked up signal from a region larger than the FOV. Those overlapping parts of the object are mapped back into the FOV and the resulting image is aliased. The left edge maps into the right side of the FOV. The other edges behave accordingly. To increase the FOV, Δk has to be decreased. If only the gradient strength is decreased, a zoom effect results. The number of sampling points remains the same, but only a smaller FOV fulfills the Nyquist theorem. Aliasing can only be avoided when the sampling rate is improved (Δt is decreased) simultaneously. Then, the total FOV gets again larger.

The recorded k-space signal is truncated by the applied gradient. The final expression for the acquired signal corresponding to finite sampling is thus the product of the continuous signal with the sampling function and a window function. In case of a rectangular gradient lobe (boxcar gradient) the window function is a sinc function in Fourier space. Hence, the final expression for the spin density function is the convolution of the real spin density with the sampling function and the calculated sinc function. Only in the limit of an infinite boxcar gradient the narrowly peaked sinc function is approaching a delta function. The windowing of the k-space signal leads to the x-space image blurring. Hence, there is a lower limit for the spatial resolution in the image.

Phase Imaging

The signal $s(k)$ (considering only one dimension) acquired by the MR system is the Fourier transform of the spin density $r(r)$ and thus an inverse Fourier transform has to be conducted by the reconstruction computer of the system to get a spatial image $\hat{r}(r)$. This is of course only an approximation of the original image $r(r)$ due to sampling effects and additional image noise.

The obtained image $\hat{r}(r)$ can also be a complex quantity, whereas the original image $r(r)$ must, of course, be real. Additional information is stored in the phase of the complex reconstructed image $\hat{r}(r)$. For example, an uncentered gradient-echo results in a linear phase shift of the spatial image 'shift theorem'. If the echo is shifted like $s(k) = s(k - k_0)$ along the read direction, the phase of the reconstructed image will change by

$$\Delta f(x) = 2\pi k_0 x. \quad (1.43)$$

This yields to so-called 'aliasing bands'. As the phase image usually is mapped into the interval $[-\pi, \pi]$, phase differences of 2π result in the same phase value 'phase aliasing'. An echo shifted sample point from the center yields a phase shift in the phase image and thus gives information about the sequence acquisition.

Chapter 2

Materials and Methods

In this chapter, the basic methods applied in this work are discussed. In the first section, system architecture of MR-tomography i.e. the process from spin preparation until image recording, will be described. As a next step, the basic MRI sequence applied in this work is presented, which is the gradient-echo sequence. Two types of gradient-echo sequences are used in this work. ‘The Fast Low Angle Shot’ (FLASH) and the ‘Fast Field-Echo Imaging with Stationary Precession’ (TrueFISP) sequence will be introduced. Furthermore, the technique of ECG-synchronization applied with both imaging sequences is explained.

In the second section of this chapter, the methods used for CT imaging are described. Primarily, the principles of ‘spiral computed tomography’ are presented. Also, an ECG-synchronization technique has to be used for cardiac imaging in CT.

At the end of the chapter, image processing methods will be presented. ‘Active contours’ is an appropriate and modern approach in image processing for feature segmentation. The concepts of this technique will be discussed, such as ‘prior knowledge’ imaging, contour iteration and interpolation methods.

2.1 Magnetic Resonance Imaging

2.1.1 MRI Hardware

The MR images were acquired on a clinical 1.5 Tesla entire-body scanner (Symphony Siemens AG, Erlangen, Germany) with a maximum gradient strength of 30 mT m⁻¹ and a maximum slew rate of 125 mT m⁻¹ ms⁻¹. A phased-array body coil with four elements was employed for signal acquisition.

The relation between the magnetic field B and an electric current is depicted by the law of Biot and Savart'

$$d\vec{B} = \frac{\mu_0 \cdot I}{4\pi r^3} \cdot \vec{r} \times d\vec{l}, \quad (2.1)$$

with the electric current I and the vector \vec{r} between the current element $d\vec{l}$ and the position where the magnetic field is measured. Because there is always a stray field outside the magnet, the magnets have to be shielded by either an iron shield (passive shielding) or by extra coils (active shielding). These coils have a larger diameter and carry opposite current. For the passive shielding, up to 20 tones of iron are required for a 1.5 Tesla system. Both shielding techniques decrease the field inside the primary coil.

To reach a magnitude of 1.5 Tesla and more, modern MRI systems use superconductive magnets. The coils must be immersed in liquid helium of a temperature below 4.3 K. To guarantee high homogeneity of the magnetic field, a so-called 'shimming' is necessary. For this, normal conductive coils compensate these inhomogeneities (active shimming).

2.1.2 Gradient Echo Sequences

The imaging sequence is a protocol that describes the entire set of events generated by the MR system. All combined rf-pulses and gradient waveforms are defined in such sequences. Basically, there are two types of sequences: The spin-echo sequence and the gradient-echo sequence. The difference is the method to obtain the echo. With a spin-echo sequence, this is managed by means of a 180° rephasing rf-pulse.

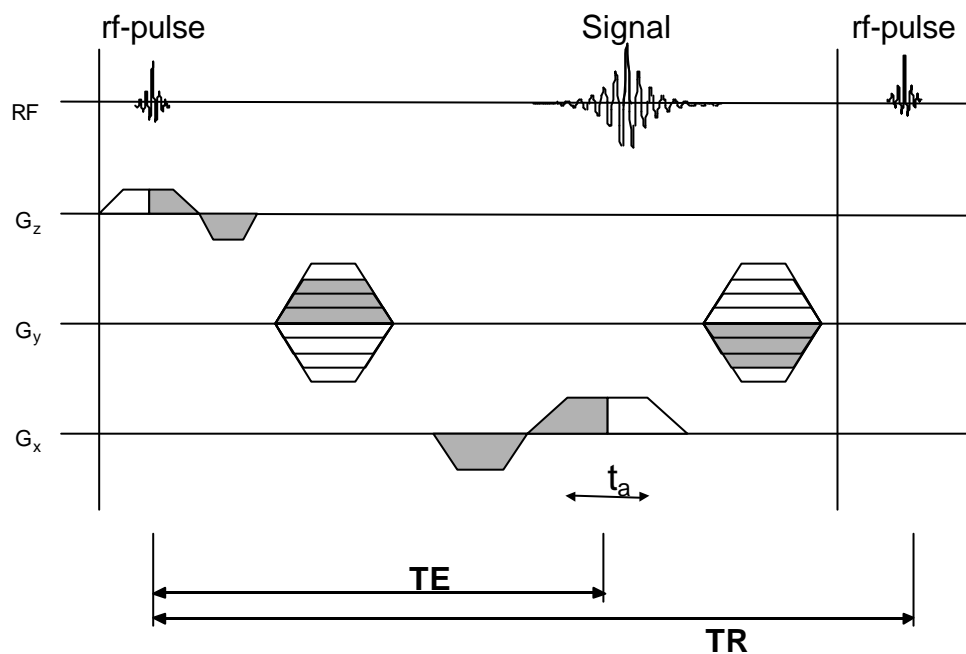


Fig. 2.1: Gradient Echo Sequence

The excitation pulse with which a sequence starts generates the transverse magnetization. The magnetization profile of a single k-line is acquired by changing the phase-encoding gradient G_y after each rf-pulse. The gradient-time integral has the same value in each interval between the rf-pulses (gray areas). The sequence recurs after each rf-pulse.

The gradient-echo sequence does not apply this pulse, but reverses the read-out gradient polarity by 180° as described below. But while the gradient-echo refocuses the phase due to the application of the gradient, it does not refocus the dephasing

induced to static-field inhomogeneities as the spin-echo does. Hence, problems caused by dephasing can occur more often.

Since the gradient-echo sequence is a very fast technique, it is used in this work to record the movement of the aorta. We applied two types of gradient-echo sequences, the FLASH (Fast Low Angle Shot) sequence [12] and the TrueFISP ('true' Fast Field-Echo Imaging with Stationary Precession) sequence [34]. Both are introduced in the following. The first step is the excitation of the slice selection by G_z . By means of the rf-pulse, the magnetization of this slice is turned by a flip angle α . Since there is no real reason to restrict the excitation angle to 90° in this type of sequence, the decrease in the longitudinal magnetization is limited. That is the reason why this sequence type is called FLASH (Fast Low Angle Shot).

So a short repetition time TR is possible without too strong saturation taking place. Also, it is not necessary to wait for equilibrium state before exciting the next profile. Since the T1 relaxation is not complete, a dynamic equilibrium will arise. Banding effects over the entire image may occur if TR is too short i.e. equal to T2. They are induced by transverse magnetization from earlier excitations. Also, the echo time TE can be set very small to avoid almost a loss of signal due to T2* relaxation.

After a number of excitations a dynamic equilibrium called 'steady state' builds up. Then, the same magnetization appears after each excitation. The slice selection gradient is always inverted for half the pulse duration after the rf-excitation. Thereby the spin-dephasing at the extremities of the gradient is reversed and the spins are rephasing. The rephasing gradient and the phase-encode gradient can be switched at the same time, since their effects are linear and hence additive when the rf power is absent.

As seen in Fig. 2.1, the phase encoding gradient is inverted after acquisition, accelerating the steady state process. For FLASH sequences, a spoiling gradient will be set in the direction of the slice selection gradient. This destroys the remaining transverse magnetization.

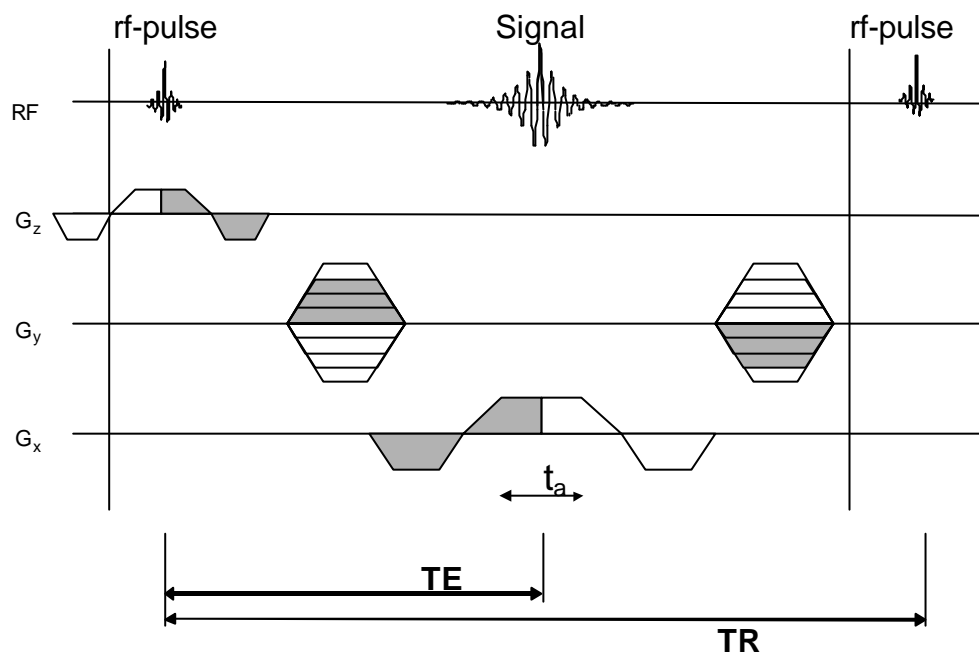


Fig. 2.2: TrueFISP Sequence

A typical TrueFISP sequence is depicted. All image gradients are balanced i.e. the total area of every gradient is zero for every acquisition. Thus, all excited spins reach steady-state free precession (SSFP) equilibrium, and banding effects due to different local magnetic fields can be avoided.

Additionally, by means of permanent phase changes of the rf-pulse (rf-spoiling), this residual magnetization can be reduced. In contrast, the TrueFISP sequence uses the remaining signal for the next excitations, as will be discussed in the next section.

2.1.3 FLASH and TrueFISP

After applying the excitation rf-pulse with a certain flip angle α , the longitudinal magnetization is reduced by a factor $\cos(\alpha)$, while a transversal magnetization M_T proportional to $\sin(\alpha)$ is built up. After a couple of rf-pulses, the spin system reaches the steady state. At the echo time TE the signal can be described by

$$M_T(t) = M_0 e^{-TE/T2^*} \frac{(1 - e^{-TR/T1}) \sin \mathbf{a}}{1 - e^{-TR/T1} \cos \mathbf{a}}. \quad (2.2)$$

The signal can be maximized by adapting the flip angle according to T1. The result of this optimization is the so-called Ernst-angle and is determined by

$$\frac{\partial S}{\partial \mathbf{a}} = 0 \quad \Rightarrow \quad \mathbf{a}_E = \arccos(e^{-TR/T1}) \quad (2.3)$$

assuming that the transversal magnetization between two rf-pulses vanishes completely by spoiling the signal. Spoiling by gradients (or also by rf phase cycling of the excitation pulse) minimizes the coherence between the actual FID (free induction decay) and the transverse magnetization resulting from earlier excitations.

If this spoiling is not applied and TR is on the order of T2 (TrueFISP Fig. 2.2), an additional transverse magnetization will persist before every excitation and thus more signal will be available. After several rf-pulses, this transverse magnetization consists of a number of echoes, caused by the preceding excitations. Assuming very small repetition time TR (smaller than T2), the relative complicate signal behavior [11] can be approximated with

$$M_T(t) \cong \frac{M_0 \cdot \sin \mathbf{a}}{\left(\frac{T1}{T2} + 1\right) - \cos \mathbf{a} \cdot \left(\frac{T1}{T2} - 1\right)}. \quad (2.4)$$

Thus the contrast obtained with a TrueFISP sequence is neither T1 nor T2 weighted. The obtained T2/T1 weighted steady state is another form of contrast. Tissues with a

very high T2/T1-ratio therefore have high signal. The optimal flip angle is determined by

$$\cos \alpha_E \cong \frac{(T1/T2)-1}{(T1/T2)+1}. \quad (2.5)$$

Due to the position dependence of the steady-state magnetization, there are bands with varying contrast formed in the image. However, if all gradients have a zeroth moment of zero over every TR (i.e. they are all balanced), all excited spins reach a 'steady-state with free precession' equilibrium (SSFP). This SSFP depends only on the precession angle with no gradients on the so-called 'free precession angle' and is hence unaffected by a particular gradient structures (Fig. 2.2). Thus, banding effects can be weakened.

2.1.4 ECG-Synchronization

Although the gradient-echo sequences are very fast, their temporal resolution is not sufficient to record the heart beat in real time. However, to improve temporal resolution, we need to synchronize the sequence to the rhythm of the myocard.

This can be achieved by means of electrocardiogram gating (ECG). With this method, the weak signals due to depolarization and repolarization waves in the heart can be recorded. In particular, a peak which appears at the beginning of the heart beat, referred to as the R-peak, is used for triggering Fig. 2.3.

ECG Triggering and Gating

The stroboscopic effect, obtaining measurements for one image at a specific heart phase from different heart beats, is related to the idea of triggering the heart beat.

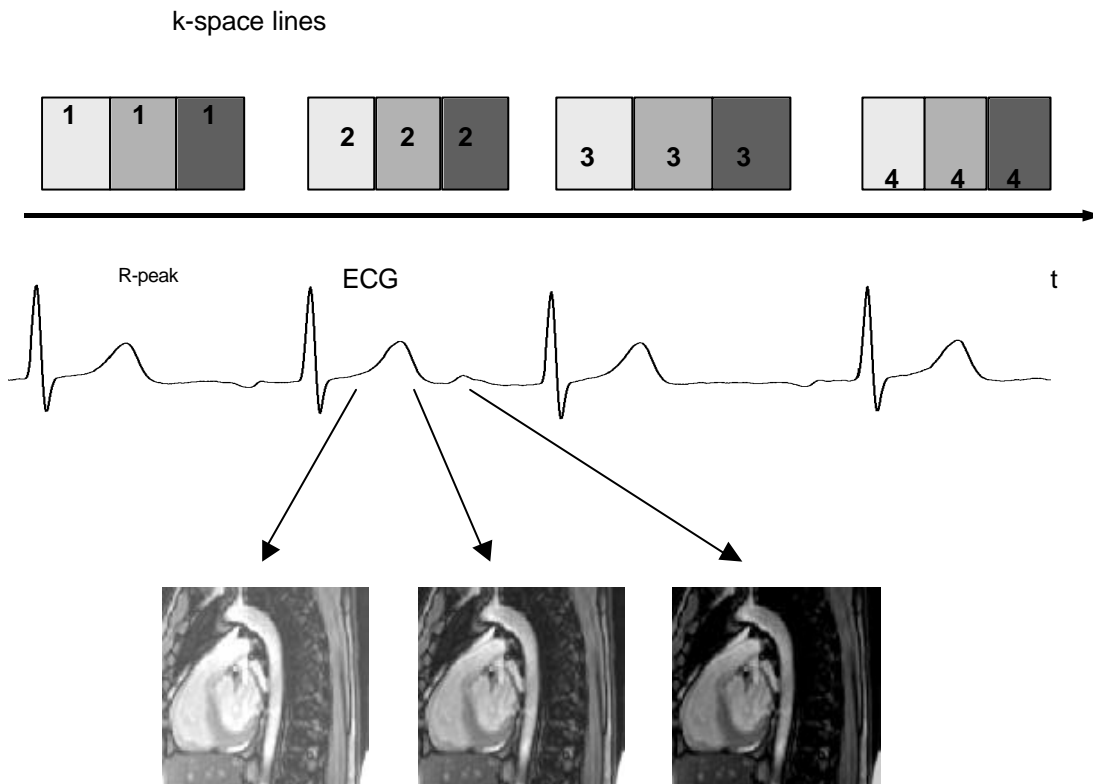


Fig. 2.3: Principle of ECG-triggering

Every R-peak of the ECG induces the repeated acquisition of a certain k-space line. To reconstruct the entire image, just as many heart beats as k-space lines are needed. In this example four lines are required and three images can be acquired. The data have to be sorted corresponding to the correct image. So, data for one image are obtained from measurements at a specific heart phase from different heart beats. The brightness of the depicted images indicates their belonging to a certain heart phase for the sake of clarity.

When the signal is triggered, every R-peak activates the repeated acquisition of one particular k-space line. The number of acquisitions and thus the number of images is limited by the time of the heart phase and the duration of the acquisition.

As a result, the temporal resolution corresponds to the repetition time TR of the sequence. This process is repeated for the following heart beats until sufficient profiles are measured for the reconstruction of the image. However, the recorded k-space lines have to be sorted correctly to build up the image.

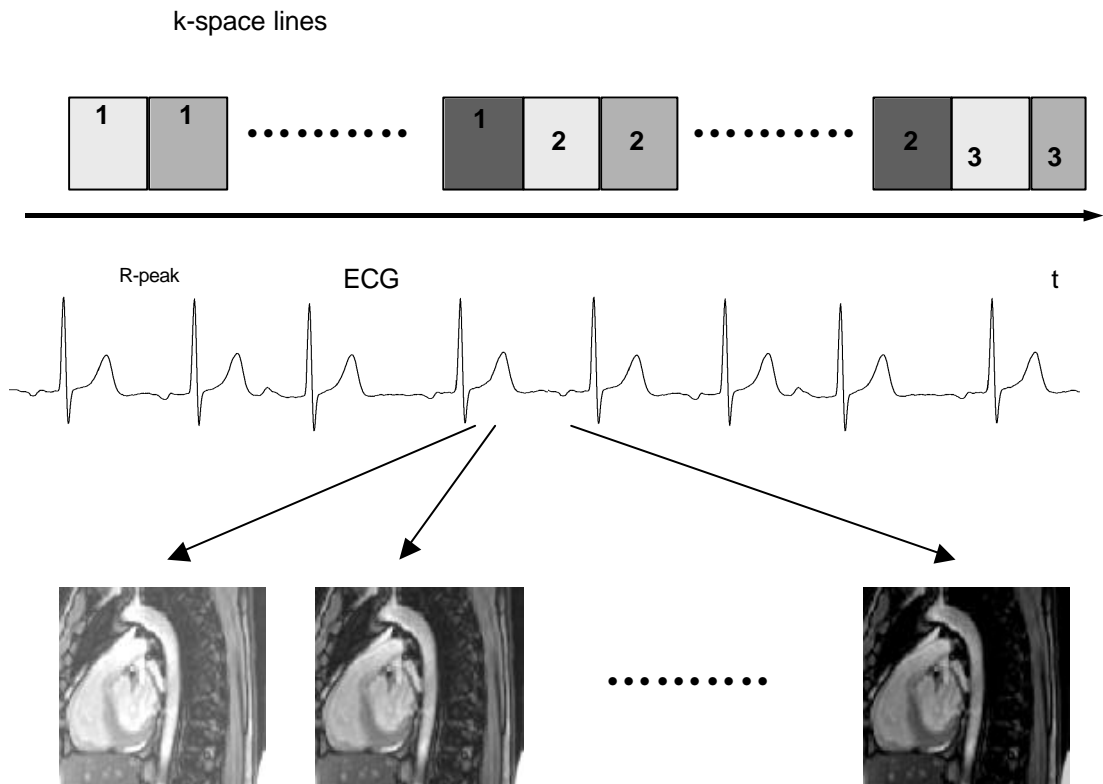


Fig. 2.4: Principle of ECG-gating

The acquisition of the data takes place continuously and is not influenced by the ECG-signal. Every k-space line is recorded repeatedly with a defined number depending on the required time resolution and acquisition duration. The ECG is stored and the distance to the last R-peak is calculated for every line in k-space. Again the recorded data have to be sorted corresponding to the heart phase. Hence, a steady state can be achieved and the time resolution can be improved. Again, the brightness of the images indicates to which heart phase it belongs.

There is another disadvantage of this method apart from the limited temporal resolution. Since there is still no saturation the first image after the R-peak is relatively bright and the time series is not homogenous. A solution to this problem

will be a continuous data acquisition, so that the 'steady state' can be achieved (Fig. 2.4).

Every line in k-space is registered continuously over several heart beats, but without influence from the ECG. The acquired k-space lines are rearranged into time slots of known phase. The heart phase can be assigned to every recorded line because of the parallel recording and storing of ECG. Thus, each image is built up from k-space lines taken at the same heart phase.

This method is called 'retrospective triggering'. After several heart beats the acquired data is distributed relatively regularly over the heart cycle. Although the total acquisition time increases due to the augmented temporal resolution, we get a better signal-to-noise ratio. This is due to the corresponding data set that can be found at every phase of the heart cycle. Missing data can be interpolated from profiles recorded before and after the phase in demand. After having acquired a sufficient number of images at different heart phases, a cinematic display of the heart motion is possible.

2.2 Methods in CT

2.2.1 Technical Concepts

Today's CT scanners record about 1000 projections. Each of them delivers 1000 values to reconstruct the images. Typical image resolutions of about 0.3 mm result from image matrices of 512×512 points. The main improvement of computed tomography concerns the velocity, from which the projections can be acquired.

Hounsfield originally used only one detector according to the translation-rotation principle (Fig. 2.5). Where the object was scanned by the radiation source and the detector in a linear translatory motion. The action was repeated for each rotation step. To speed up this original setup, more detectors were added for the second generation and the pencil beam was replaced by a small fan beam (Fig. 2.5).

Modern CT scanners use the fan beam system together with a rotating detector arc. As a result, a complete projection can be recorded simultaneously and the available x-ray power is utilized much more efficiently. Also, the translatory motion becomes unnecessary. The system only exercises in a rotatory motion, in which an image scan time of 20 seconds can be achieved. While in the 3rd generation (Fig. 2.5) both the x-ray tube and the detector rotated around the patient, the next generation used ring-like stationary detectors. They fully encircled the patient, allowing only the x-ray tube to rotate around the patient (Fig. 2.5). During this rotation, which takes approximately one second, fan-like projections are acquired. Between the detector elements, collimators are installed absorbing the scattered x-rays, which is why the 3rd generation is the standard scanner configuration today.

The detector system is one of the most important and technologically critical components of the entire CT scanner system. Two detector types are predominant in

computed tomography. One detector type with ionization chambers filled with the noble gas xenon under high pressure. The other type with scintillation detectors in the form of crystals.

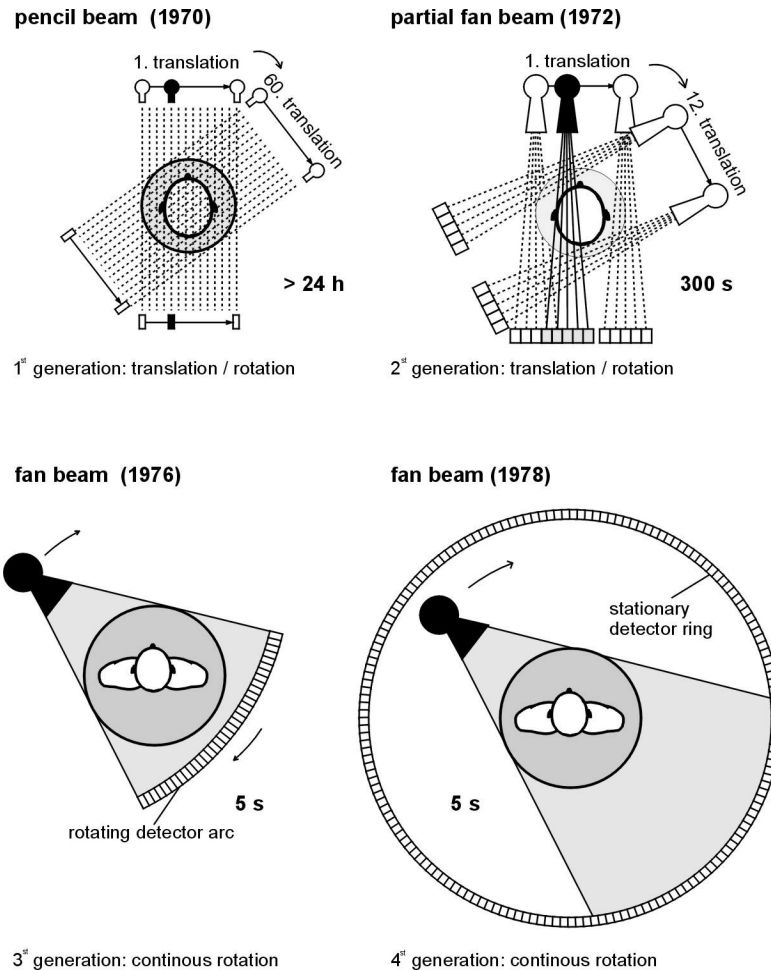


Fig. 2.5: Different Scanner Generations

There are four scanner generations known in CT. The original Hounsfield scanner (top, left) used a pencil beam. The next generation included several detectors and a fan beam system (top, right). The next step added rotating detectors (bottom, left) and finally the 4th generation applied stationary detector rings (bottom, right) [22].

The first mentioned ionization chambers have the advantages of simple construction and a more regular sensitivity. The temporal response and the low afterglow favor this technique. All multi-row detectors and all new detector systems however, are

built with ceramics or scintillation crystals. These systems cannot be manufactured with xenon chambers.

2.2.2 Spiral Computed Tomography

In the beginning of computed tomography, only single slices were recorded and the patient had to be moved forward for the next slice. This method was very time-consuming and was replaced by spiral CT. With this method, a fast and continuous scanning of complete volumes is possible.

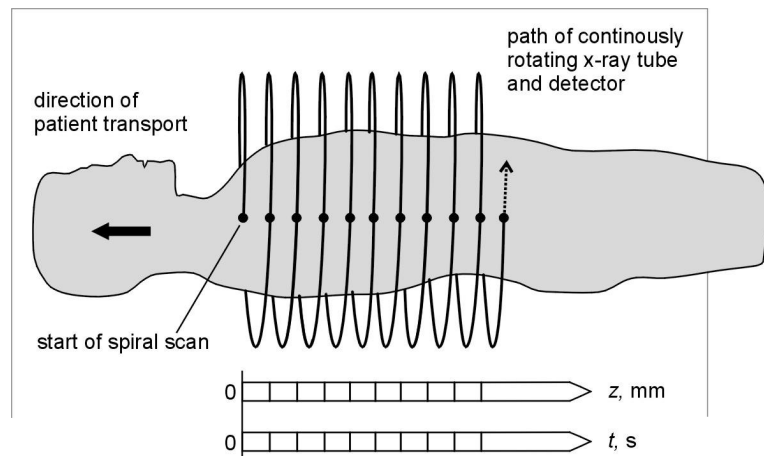


Fig. 2.6: Principle of Spiral CT

The continuously rotating x-ray tube scans the patient while the table is moved horizontally as indicated by the arrow. By this method the entire volume of the patient can be acquired in short time [22].

With spiral computed tomography, a volume of the patient is recorded continuously in space and time as can be seen in

Fig. 2.6. The ratio of table movement per rotation, in units of the slice thickness, is generally termed the pitch or pitch factor. Usually, pitch factors between 1 and 2 are chosen.

The speed of such a scanner is typically one or two slices per rotation, resulting in a velocity up to 20 mm/s for a 1 sec scanner (one rotation per second) with a single-row detector. The x-ray beam follows a spiral trajectory. This results in motion artifacts when reconstructing the image. As a result, an interpolation of the data has to be applied. This preprocessing step is also called z-interpolation. In the simplest way linear interpolation is applied between data measured for a given angle close to the desired table position. The slice profile grows a little thicker but the image can be reconstructed at any position.

The latest developments of spiral CT are the multi-slice spiral CT scanners. Instead of one detector row, several of these rows are placed side by side. Thus, it becomes possible to acquire several slices per rotation.

2.2.3 ECG-correlated Cardiac Imaging

As the time for one cardiac cycle is typically less than one second for typical heart frequencies, it is not possible to record the heart motion without artifacts. As previously described for MR cardiac imaging, in CT ECG triggering or rather ECG gating must also be used. Hence, the ECG signal is recorded synchronously with the CT measurement.

During the data acquisition, for every projection the distance relative to the last R-peak is recorded. The image of a certain heart phase is then formed by sorting the data corresponding to the specified heart phase but from different heart cycles (Fig. 2.7). Short intervals of the ECG are mostly sufficient and allow a significant reduction in effective scan times.

Temporal resolution depends on the relation between heart rate and scanner rotation time. The selection of data belonging to a certain heart phase, allows to improve temporal resolution at the expense of spatial resolution.

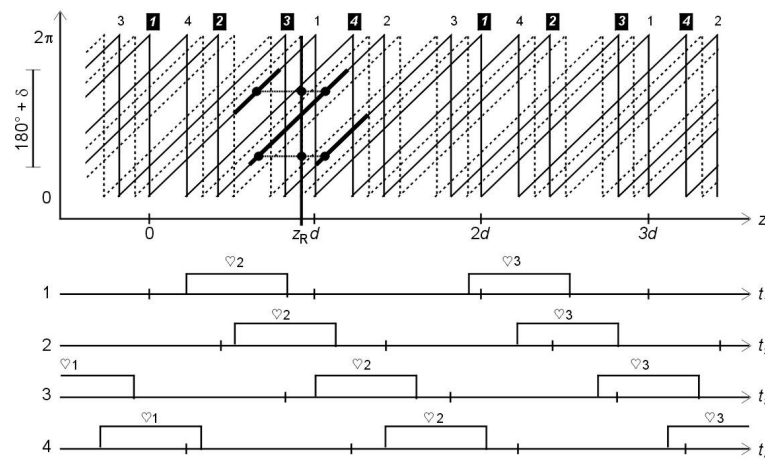


Fig. 2.7: Retrospective Cardiac Gating and CT Image Formation

The upper row shows a plot of detector angles for each of the 4 detectors as a function of table position z . The dotted lines indicate opposite projections (where x ray tube and detector are interchanged). Only a projection data range of slightly more than 180° is used for ECG gated image reconstruction. The same projection angle is available at different heart phases. Thus, each measured projection can be assigned a time within the cardiac cycle were it was acquired. For each angle within the selected interval (circular dots), a number of possible data values are available. These values differ in temporal and spatial distance to the desired reconstruction position z . The values are then filtered so that the projections which fit best contribute most to the image [22].

For a typical interpolation range of 4 rotations the temporal resolution ranges between 90 and 250 ms. With a heart rate of for example 70 beats per minute a temporal resolution of 140 ms is obtained. Applying additional oversampling, e.g. 20 time frames can be calculated, resulting in smooth area-versus-time-curves.

2.3 Image Processing Techniques

2.3.1 Active Contours

Prior information is not only a topic of Computer Vision as the human visual system also makes use of it to interpret an image. Without prior information some images do not mean anything to us, and only after having received any clue does the meaning pop out of the image. In this work, prior knowledge is applied to detect the shape and outline of the aorta. By means of the most general prior knowledge about the smoothness and continuity of the aortic border, that is, geometrical knowledge.

If the form and size of the expected contour is given, it has to be matched to the edge presented in the image. The challenge is to recover the border of an object undamaged and free of gaps. By varying elastic parameters, the strength of prior assumptions such as smoothness and curvature of the contour can be controlled. A milestone on visual analysis of shape and a fundamentally new approach was the introduction of the so-called ‘snake’ concept in [23].

A ‘snake’ or ‘active contour’ is an elastic contour which is fitted to features detected in an image, the ‘posterior’ information. Mathematically, the ‘snake’ is a parametric curve $\mathbf{r}(i)$ which consists of a set of vertices i with $0 \leq i \leq n$, connected by edges or spline segments [23]. As a characteristic feature, for example, the image gray value gradient or other image textures can be used. Although there are other ‘active contour’ models such as ‘deformable templates’ and ‘dynamic contours’, in this work the notion ‘snake’ and ‘active contour’ [2] are used synonymously.

The principle of feature detection is that first an operator has to be designed which produces an output signal where the desired feature is present. This results in a ‘feature map’ where the strength of a particular feature is emphasized at each pixel,

as shown in Fig. 2.8. The operator used here was the so-called Sobel operator, which additionally averages the image in the direction perpendicular to the differentiation as described in [19].

At first it is important to take a closer look at such image features regarding the presence of the desired shape information. Although the feature map enhance desired features, most of the time they do not unambiguously detect them. Because of gaps and spurious fragments as seen in Fig. 2.8, the gradient image is not sufficient to determine all edges and shapes that appear in the image. Some geometrical structures can even be distorted, e.g. as a result of noise or patient movement.

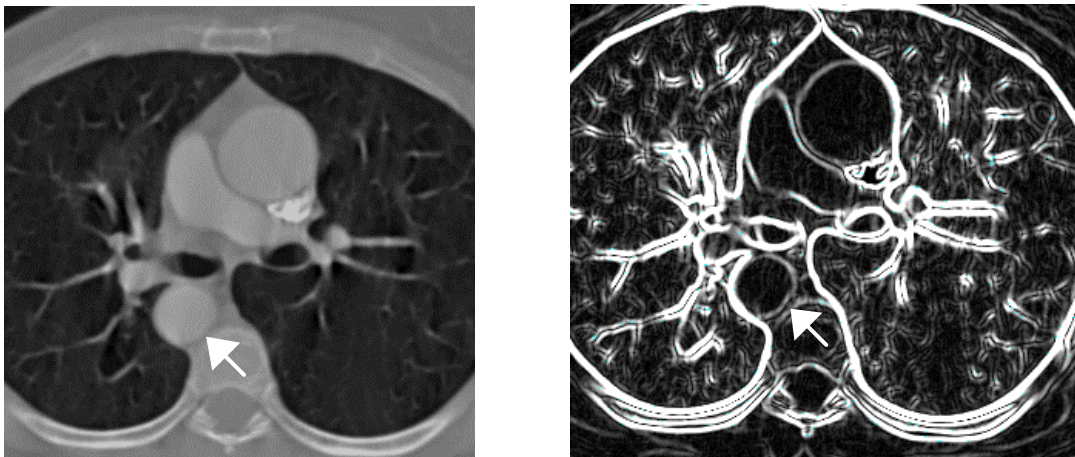


Fig. 2.8: Image Feature Map

These two CT images explain the convolution-operation with a certain ‘mask’ or ‘operator’ with the original image (left) resulting in the ‘feature map’ (right). The image feature chosen here was the gray value gradient. The Sobel operator used here codes the strength of the gray value gradient in the image at each pixel. The aorta is marked by the white arrow.

Thus, these ‘low-level’ feature detection processes are not useful to accurately detect the aortic border. Utilizing only what is available in the image itself, is not

sufficient,. A new approach is in demand that also considers priori properties of the desired contour.

The idea of an active contour is to take a feature map such as the image on the right of Fig. 2.8 and use it like a ‘landscape’ on which the snake can slither. Let $F(\mathbf{r})$ be the feature image and $\mathbf{r}(i)$ the deformable curve slithering on this feature map. In the example of Fig. 2.8, $F(\mathbf{r})$ tends to attract the contour toward the object edges. Because of the high values of F at these positions, the curve tends to maximize $F(\mathbf{r})$ over all vertices $\mathbf{r}(i)$. Since the response image F can be seen as an energy landscape, an appropriate energy function representing the contour properties has to be developed.

Our model is, therefore, active and always tends to minimize its energy functional, expressed by

$$E = \sum_{i=0}^n E_{contour}(\mathbf{r}(i)) + E_{image}(\mathbf{r}(i)) = \min . \quad (2.6)$$

The contour energy $E_{contour}$, represents the energy of the curve due to bending and smoothness at each vertex $\mathbf{r}(i)$, whereas the image energy E_{image} (representing the feature map F) is equal to the gray values along the parameter curve $\mathbf{r}(i)$ of the feature map F . When equation (2.6) is solved iteratively the active contour will tend to settle on a ridge of this feature map F . There are normally additional weighting parameters which balance the relative influence of each energy term.

Thus, the image energy is counterbalanced by the internal contour energy which tends to preserve smoothness of the curve and is normally described in [23] as:

$$E_{contour} = \mathbf{a} \cdot \mathbf{r}'(i)^2 + \mathbf{b} \cdot \mathbf{r}''(i)^2 \quad (2.7)$$

where the spatial derivatives \mathbf{r}' and \mathbf{r}'' have to be approximated over all vertices $\mathbf{r}(i)$ spaced at intervals of length h by

$$\mathbf{r}'(i) = \frac{\mathbf{r}(i) - \mathbf{r}(i-1)}{h} \quad \text{and} \quad \mathbf{r}''(i) = \frac{\mathbf{r}(i-1) - 2 \cdot \mathbf{r}(i) + \mathbf{r}(i+1)}{h^2} \quad (2.8)$$

as the active contour represented by the vertices $\mathbf{r}(i)$ must occur over discrete time and space steps.

In equation (2.7) the first-order term is controlled by \mathbf{a} and the second-order term by \mathbf{b} . They may be allowed to vary along the vertices of the snake. By adjusting the weights \mathbf{a} and \mathbf{b} the property of the curve can be controlled. Increasing \mathbf{b} smoothes the snake but also encourages it to regress towards a straight line. Whereas setting \mathbf{b} to zero at a certain point $i = i_0$ will allow the snake to kink and develop a corner. Increasing \mathbf{a} increases the tendency of the curve to contract and even to collapse to a point. The variables $\mathbf{r}(i)$ are regarded as vertices from which the continuous curve can be modeled as a polynomial 'spline curve' as it is common in computer graphics. The spline passes close, but not necessarily through, the nodal points. Thus, a certain degree of smoothness can be reached. A spline of order d is a piecewise polynomial function, consisting of concatenated polynomial segments. Each of these spans or B-splines has the polynomial order d . The B-splines are joined together at knots or vertices. Thus, simple shapes can be represented by a contour with few splines.

Chapter 3

Measurements and Results

In this chapter, the results from MR and CT compliance measurements are presented. The first section describes the developed algorithm for aortic boundary segmentation in more detail. The ‘active contour’ model as described in chapter 2.3 is used for our approach. To evaluate the algorithm, images with different signal-to-noise ratios were simulated. The reliability of the algorithm was tested, using images with different signal-to-noise ratios.

In the second section of this chapter, MR measurements of the aorta are presented. Results from black- and bright-blood MRI acquired by FLASH and TrueFISP sequences are depicted. Furthermore, compliance from ten healthy volunteers were determined by using MRI aortic cross sectional measurement as well as pulse-wave measurement.

In the last section of the chapter, results from multi-slice CT imaging based on retrospective multi-phase ECG-gating are shown. First, the active contour algorithm was applied on images obtained from phantom measurements. Then, preliminary results from CT measurements applied to two patients are presented.

3.1 Active Contour Algorithm

3.1.1 Development of an Active Contour Algorithm

The algorithm developed in this work is able to segment the aortic boundary from the acquired MR- and CT-images automatically. The operator has to define one ‘seed point’ somewhere in the center of the aorta. After that, the contour inflates such as a balloon [7] until the vessel wall is found. Our deformable contour consists of evenly sampled vertices connected by spline segments. It is thus a discrete contour model [27]. However, in order to better fit the boundary for cross-section calculation, B-Spline interpolation is applied to connect the vertices. The vertices are uniformly sampled along equal angle segments ?? of the ‘balloon’ relative to the ‘seed point’. The number of the segments ?? depends on the desired total number of the vertices.

The final contour is found by means of an iterative process. The driving force behind this process is a sum, determined at each vertex by an image force derived from the gray value gradient, and an internal force derived from the contour shape itself. The final position of the contour is found at the equilibrium of all forces acting on the vertices. This approach is completely analogous to the concept of energy minimization in physics. Here, the total energy is defined as a sum of the internal contour energy and the image energy, each weighted by a factor for all vertices. The image energy is determined from a feature map with high response at image features of a particularly chosen type. In our case, the image edges. It is counterbalanced by the internal energy which tends to preserve the smoothness of the contour. During each iteration step, for each vertex a neighborhood is considered proportional to the contour energy. The point in this neighborhood which gives the smallest value for the total energy, is chosen as the new location of the vertex. This process is repeated

for all vertices of the contour and the new contour energy is computed. From this, a new neighborhood is determined for each vertex.

Assuming that the aortic shape is roughly circular, the internal energy was defined to be small for parts of the outline where the curvature is circular, to avoid the contour to implode due to internal forces. Furthermore, by allowing the vertices r_i of the contour balloon only to move radial from the ‘seed point’ set by the operator, clustering and gathering of the vertices is avoided. The following definition of the internal energy satisfies both conditions made above:

$$E_{\text{contour}} = \frac{1}{2} \cdot \left(\max(|r_i - r_{i-1}|, |r_{i+1} - r_i|) \right)^2 \quad (3.1)$$

Thus we summarized the two terms from equation (2.7) in only one curvature term, which considers continuity and curvature. As we assume a circular shape of the contour, we do not need the weights \mathbf{a} and \mathbf{b} for the contour energy.

As already pointed out, an image potential energy is applied to relate image features to the contour model. In our model, the length of the gray value gradient vector along the radial displacement of the vertices was chosen. In order to get subpixel resolution, bilinear interpolation was applied to the pixels. As a result of this energy, the contour tends to follow a maximum gradient path through the image if no internal energy is considered. For the image energy the following definition was used:

$$E_{\text{image}} = |G_{\sigma} \otimes (\nabla I)_{\text{max}} - G_{\sigma} \otimes (\nabla I)| \quad (3.2)$$

where ∇I is the radial image gradient from the starting point set by the operator convolved with the Gaussian operator G_{σ} with a characteristic width of $\sigma = 3$ subpixels. The image gradient ∇I was here normalized to one for each vertex. Thus, weaker and stronger edges have the same influence on the image energy. This is important as strong edges which correspond e.g. to the interface between the aorta and the lung capacity will otherwise have too much influence on the image energy. By means of normalizing the image energy, its influence is evenly distributed over

the entire contour. As with an inflating balloon, we add a pressure force to the contour. This force (resulting in an energy shift) inflates our balloon from the initial seed point, set by the operator, until the image energy of an edge point presents a local minimum, thus counteracts the inflation force. However, if the edge is too weak, the contour can pass through it.

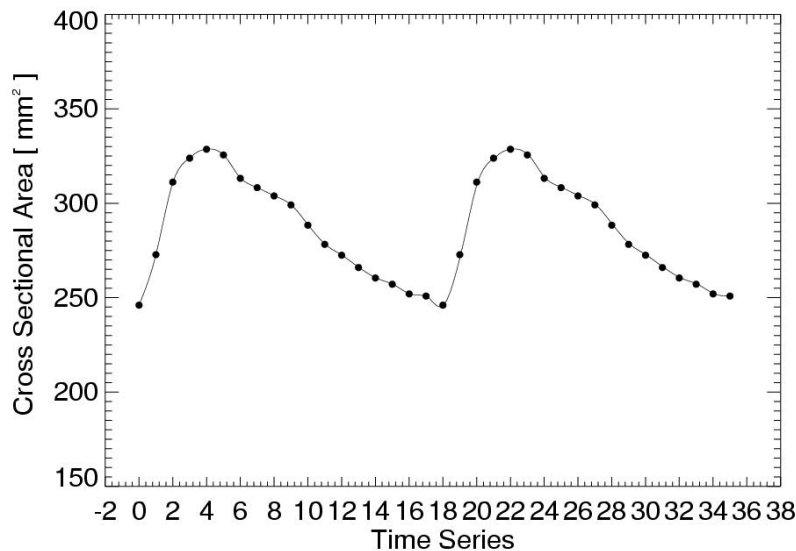


Fig. 3.1: Smoothed Curve from Aortic Cross Sectional Area

A curve of aortic cross sectional area smoothed with interpolated data from 2 heart cycles. A least-squares-fit to a 4 point neighborhood was used resulting in 180 data points. After smoothing, the systolic and diastolic cross section value were determined. The points indicate the originally found data from segmentation before interpolation.

The state of minimum energy reached by the contour is in general one of a large set of possible local minima. By varying the pressure force it is possible to push the model out of a local minimum into another. Based on our experimental observations, adjusting only this parameter is sufficient for tuning the contour.

The resulting contour is found by iteratively minimizing the sum of the weighted contour and the image energy for all vertices. The behavior of the contour can be

influenced by changing a weighting factors of each energy term, concerning whether it should follow more precisely the image features or more the contour properties.

The deformation process itself is performed as a time integration process. This means that the strength of displacement of the vertices at every time step corresponds to their actual velocity. Their velocity is proportional to the actual contour energy at each vertex, after every deformation step. This approach prevents the contour from oscillating around a local minimum of the energy. The sum of the energy terms are evaluated after every time step until an equilibrium of the contour is found, i.e. until the total energy is minimized.

As shown in Fig. 3.1 the cross section of the resulting contour was then plotted for every acquired image through the entire cardiac cycle. To determine the systolic and diastolic cross section more precisely, the same curve was doubled and smoothed by means of a least squares fit to a 4 point neighborhood. This was applied to all vertices (two times the original number of vertices). From the maximum and minimum value of the so smoothed curve, the change in aortic cross section could be calculated more accurately.

3.1.2 Image Simulation

Images with a matrix size of 256×256 pixels and a central circle were simulated as shown in Fig. 3.2. The circle has a radius of 15 pixel. However, since it is not possible to fit a perfect circle on a rectangular grid, linear interpolation was used near the borders of the circle. Assuming that the noise yields a Gaussian distribution, we fixed the gray values difference of the circle and the background to $g = 1000$. Then, Gaussian noise with different standard deviations σ was added.

This leads to different signal-to-noise ratios according to

$$\text{SNR} = \frac{g}{s} \quad (3.3)$$

applying values for s from 100 to 500. With the equation from above we get hence signal-to-noise ratios from 10 to 2.

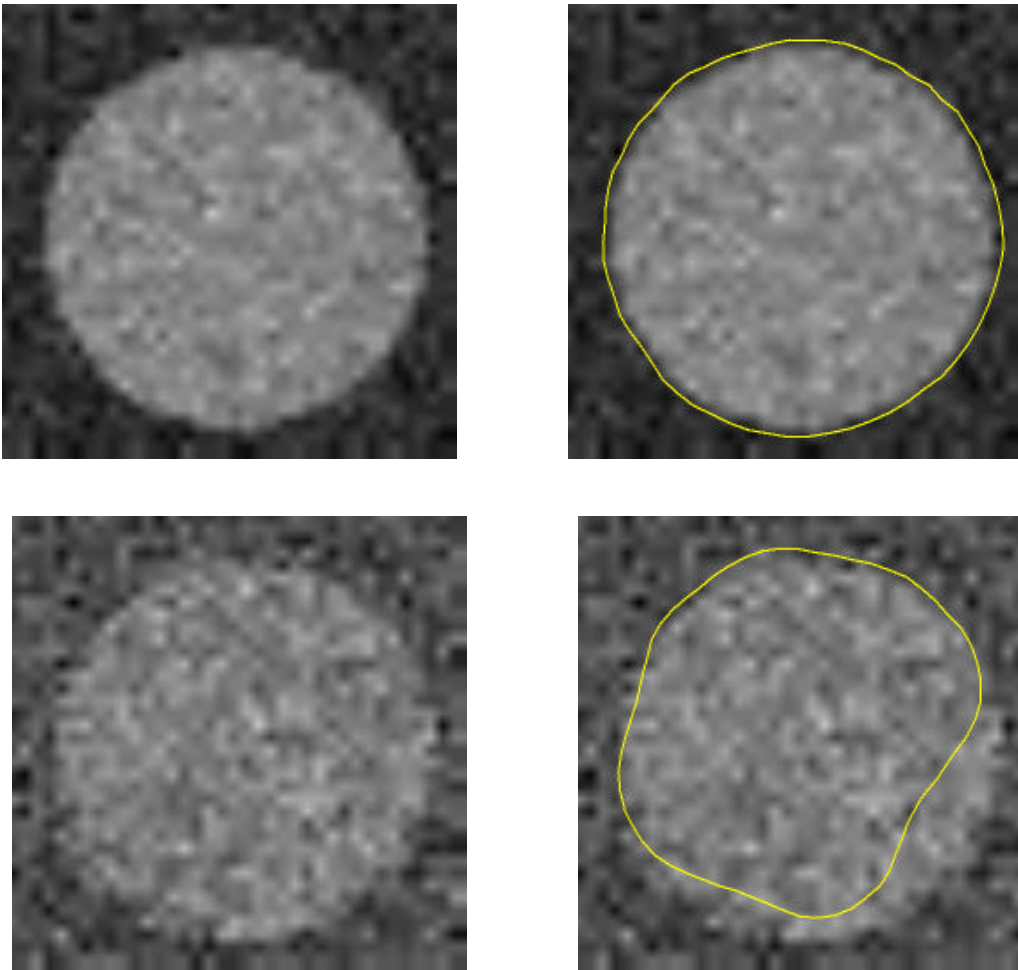


Fig. 3.2: Simulated Images

Images with different signal-to-noise ratio were simulated. The images above have a SNR of 5. As can be seen, the simulated circle (right) can be segmented very accurately (left), whereas a simulated image with SNR of 2 can hardly be recognized by the algorithm. Nevertheless, by increasing the balloon force, it is possible to force the contour to lie nearer the border of the circle but with less accuracy.

The simulations revealed that the right cross section could be found very accurately for values of the signal-to-noise ratio better than 3. Smaller SNR leads to high variances in the resulting cross sectional area as seen in Fig. 3.2. The image histograms shown in Fig. 3.3 emphasize our result. These two histograms belong to signal-to-noise ratios of 2 and 5.

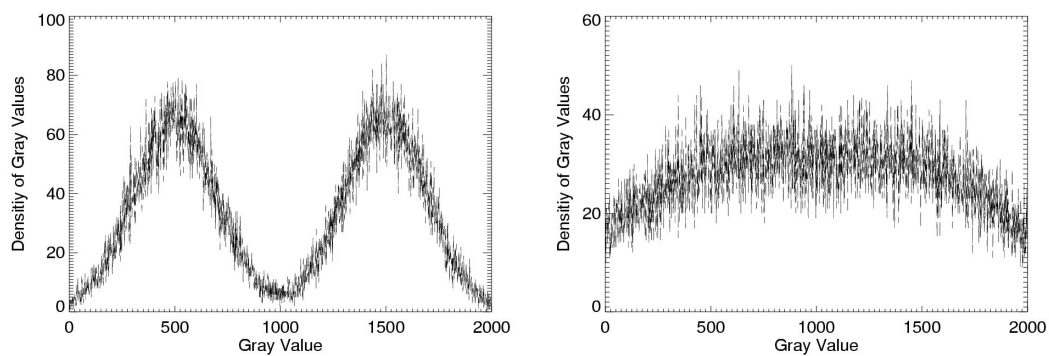


Fig. 3.3: Simulation Histogram

The two images above show the histogram for different signal-to-noise ratios. In order to depict an equal gray value distribution the number of pixels of the imaged circle are set to be identical to that of the black background. The histogram on the left belongs to an image with a SNR of 5, whereas the left histogram reveals a lower SNR of 2.

In contrast to the images shown in Fig. 3.2, we assumed the gray value distribution to be equal for the object and the background. This assumption was only made for the sake of better depiction of the histograms. Otherwise, the second peak would be too weak and hardly visible. If the signal-to-noise ratio is better than 3, the object and the background can be easily separated by the histogram values showing the two peaks clearly separated as can be seen in Fig. 3.3 (left). The area of the depicted circle can roughly be determined by calculating the area enveloped by the corresponding peak. As the object and the background have the same number of pixels, the histogram reveals two equally sized peak areas. The lower the SNR gets, the more difficult it is

to separate the two histogram peaks as seen in Fig. 3.3 (right). Thus, it is no longer possible to distinguish the object from the background using the histogram information. However, the shape of the circle can be still perceived by the eye. The algorithm is able to partially find the right contour as shown in Fig. 3.2 above. Our experiments revealed that a SNR of better than 3 is necessary to find the object's border accurately.

3.2 MR Measurements

In principle, there are two different methods to image blood flow with respect to stationary tissue. The first one is based on phase difference (phase-contrast methods) of the transverse magnetization. As a result of motion, flowing blood experiences a different gradient field with respect to stationary tissue and, therefore, accumulates a different phase.

The second method depends on the difference in signal amplitude arising from the change of position due to the blood flow during the entire measurement (time of flight TOF method). Thus the blood appears either brighter (bright-blood imaging) or darker (black-blood imaging) as described in the following section. The signal contrast of both methods depends on the different steady state condition of the spins in static tissue and the flowing spins of the blood. We used a FLASH sequence with both techniques and a TrueFISP sequence with bright-blood imaging.

3.2.1 Imaging Techniques

Bright Blood Imaging

For fast gradient-echo sequences, the contrast between the flowing blood and its surroundings can be increased by both bright- and black-blood imaging. The bright blood effect arises from non-excited (fresh) blood flowing into the image slice as depicted in Fig. 3.4. This fresh blood gives maximum signal because of its full longitudinal magnetization in the 'steady state'. Hence, the contrast between the flowing blood and its surroundings will increase.

The signal of the stationary tissue will be slightly suppressed because of saturation effects arising from repeated excitations with a relatively short repetition time TR.

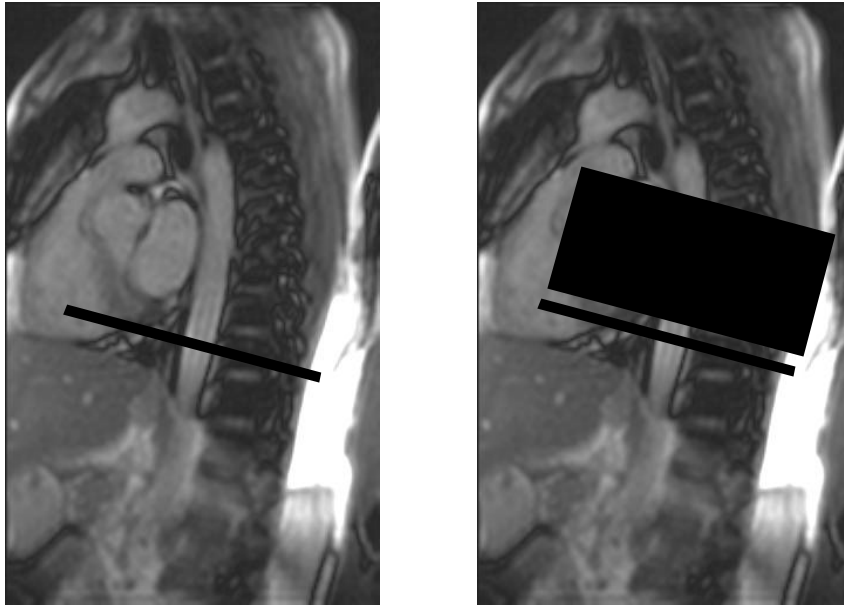


Fig. 3.4: MR Localizer Image of a Sagittal Section

A TrueFISP sequence was applied to acquire a sagittal section to localize the aorta. Thus, the acquisition slice could be set correctly. A Field of View of $375 \times 232 \times 4.5$ mm was used to record the image. The aorta descendent is visible. The acquisition slice is positioned directly over the diaphragm. The left image shows the acquisition of a bright-blood image. The image on the right side depict the set up for black-blood imaging. As can be seen, an additional saturation slice has to be placed above the acquisition slice.

The condition that the inflowing blood will not be excited during its passage through the acquisition slice is

$$v_z \cdot TR > d \quad (3.4)$$

where v_z is the velocity of blood flow in direction of the acquisition slice and d is the thickness of this slice. TR is the repetition time of the sequence. Equation(3.4) gives evidence that all excited blood spins have left the slice before the signal is recorded.

Black Blood Imaging

With black blood imaging, the blood provides no signal and appears black in the image. Usually, the black-blood method is based on a spin-echo sequence. After a slice selective excitation by a 90° pulse, the spins are refocused after the time $TE/2$.

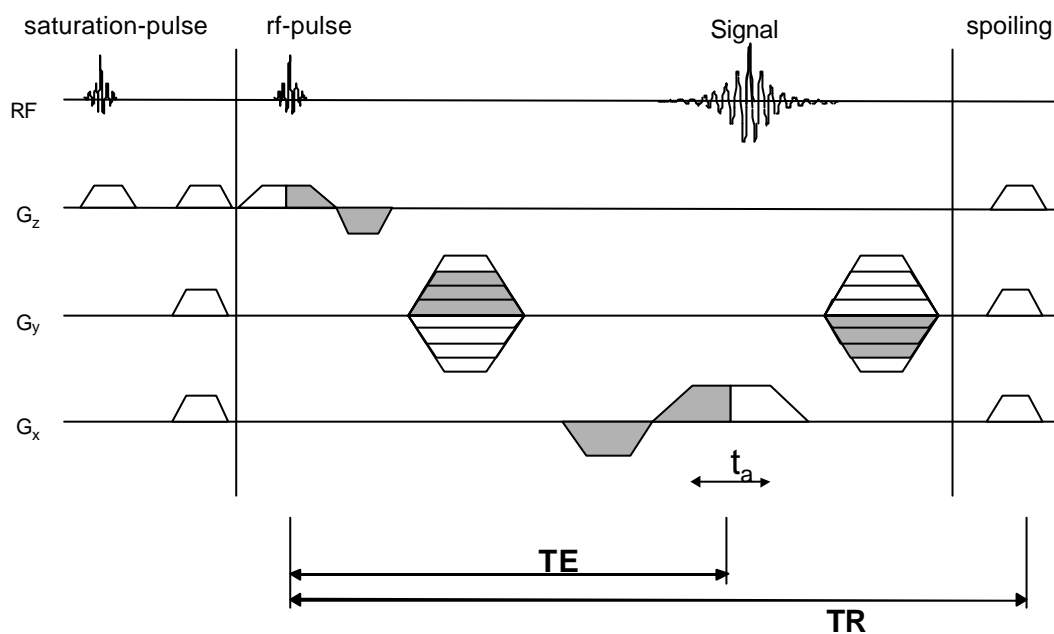


Fig. 3.5: FLASH Sequence with Black Blood Technique

The adapted gradient-echo sequence is depicted. After the first rf-pulse, the blood is saturated with the first saturation gradient applied. Using the FLASH sequence, the signal is completely spoiled with additional gradients after the image is recorded.

When the blood has completely moved out of the selected slice during this time delay, the 180° pulse only refocuses unsaturated fresh blood. Hence, there is no signal from this blood. It appears black on the image.

Although most conventional spin-echo sequences can be used for this technique and the contrast between the endothelium and lumen is very high, we used a gradient-echo sequence for our measurement (Fig. 3.5). The advantage of gradient-echo imaging is that images can be recorded throughout the entire cardiac cycle. With spin-echo sequence recording a whole image set of the heart cycle is very time-consuming as result of a longer TR (about 600ms) and a total acquisition time of about ten minutes for one image with an echo time of $TE=40ms$ [25].

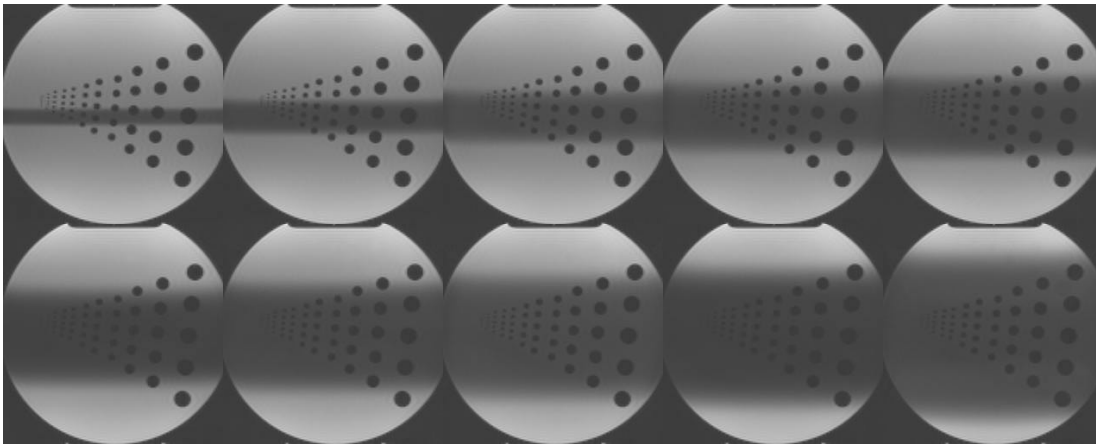


Fig. 3.6: Effective Thickness of Saturation Layer

To investigate the range of a saturation layer applied on the image, ten saturation slices at different thickness were set on the scanner varying from 10 to 100 mm. The effective signal suppression was then calculated from the image gradient.

Thus, the FLASH sequence allows the operator to detect the diastolic and systolic heart phase more accurately. As a result, the time frames when the aortic cross-sectional area is at its largest and smallest extension can be found more precisely. The disadvantage of this method is that due to turbulent blood flow near to a stenosis or a bifurcation artifacts are induced. Due to turbulent flow, a ‘flow void’ (intra-voxel dephasing) [42] occurs behind the stenosis.

Since this flow void cannot be distinguished from the saturated signal of the static tissue (because of relatively long T1 of the blood in Table 1.1), the stenosis is mostly

overestimated with bright blood imaging, whereas with black blood imaging the stenosis is imaged more precisely.

Using the black-blood imaging technique, two layers are required, as can be seen in Fig. 3.4 (right). One to label the blood before flowing into the acquisition slice (saturation layer) and the other where the signal is detected (excitation layer). The blood is labeled by applying the rf-pulse while setting a saturation gradient (spoiler) before the slice selection gradient.

Table 3.1: Values of Saturation Slice Thickness

The values of thickness of the different saturation layer determined from two methods is shown. The upper line depicts the thickness tuned directly at the scanner. The line below indicates the values calculated from the image with edge detection methods.

Thickness (scanner)	10	20	30	40	50	60	70	80	90	100
Thickness (determ.)	12.6	27.2	41.6	53.7	64.6	77.9	89.4	101.5	113.9	140.0

If the saturation layer is placed too close to the acquisition slice, the signal can be reduced considerably. The width of the saturation slice set directly at the tomograph does not correspond to the effective signal suppression. Therefore, the effective thickness of the suppressed signal was measured by means of a phantom (Fig. 3.6).

Ten different widths were selected at the scanner. To determine the effective saturation slice thickness from the obtained image, the image gradient was computed and then the distance of the borders of the slice could be calculated. The values obtained from these measurements are shown in Table 3.1. The calculated values are

systematically higher than the values set at the scanner. This was taken under consideration when setting the saturation slice i.e. the distance to the acquisition slice was increased accordingly. Applying this signal suppression, blood coming from the saturation slice is already saturated and delivers almost no transversal magnetization while image acquisition takes place. To insure that the blood has left completely the selected slice, the following relation has to be fulfilled

$$v_z \cdot T_{sat} > d \quad (3.5)$$

where T_{sat} is the time duration from the saturation pulse until the beginning of acquisition, further d is the slice thickness of the excited slice, and v_z is the blood flow velocity. The saturated blood will give less signal when compared to the surrounding static tissue which gives normal contrast.

ECG Synchronized Images

With ECG gating it is possible to compose a temporal image of the heart from measurements taken in the same heart phase of a number of heart beats. In case of gradient-echo sequences, this is managed by recording only one k-space line after every saturation and excitation pulse. The TR in our sequence (60 ms) is much shorter than the R-R interval of the electrocardiogram (about 750 ms). Thus, it is possible to acquire several k-space lines of the same row in the k-space image but at different heart phases. After having recorded all rows in k-space, the obtained data have to be sorted in the correct way before Fourier transformation.

Both ECG triggering and gating were applied. ECG triggering has some disadvantages. For example, the temporal resolution is limited by TR. Furthermore, the early images after the R-peak have full signal and lower contrast (Fig. 3.7) due to steady state conditions. Since there is no continuous data acquisition, a temporal gap after the last recordings in the heart cycle occurs where the transversal magnetization can build up. Thus, the transversal magnetization cannot reach a steady state. A

solution to this problem is continuous sampling during the heart beat. To acquire a homogeneous time series and to reach a dynamic equilibrium of the magnetization in all images, retrospective ECG gating was applied. Therefore, the data was recorded continuously and independently of the heart beat, but was temporally related to the last R-peak.

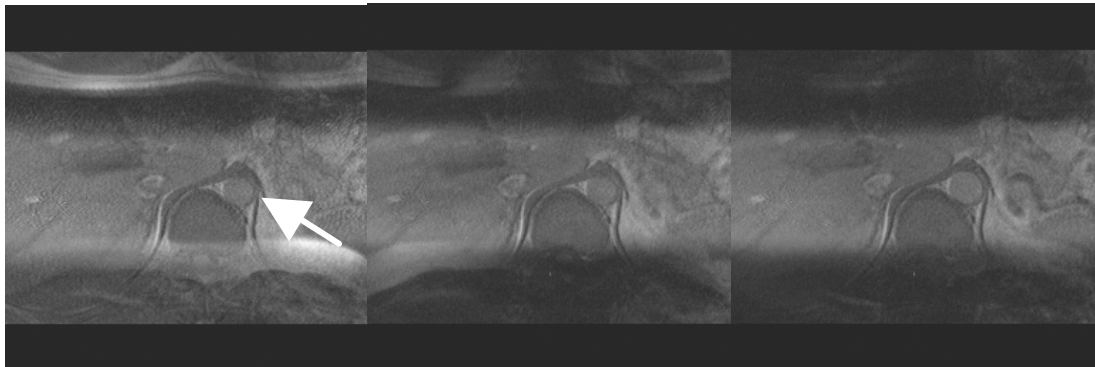


Fig. 3.7: ECG Triggered MR Images

The first three images of a MR image series are shown. The first image on the left has full signal and lower contrast than the following images. This is due to the relatively full longitudinal magnetization before excitation. The magnetization vector cannot reach a steady state, because relaxation always occurs at the end of the heart cycle. The white arrow marks the aorta.

Every line of k-space, starting with the minimum phase encoding gradient, was acquired repeatedly for a fixed number of times (in our case 18 repetitions). This image acquisition was distributed approximately equally within the cardiac cycle. During the measurement, the distance to the previous R-peak was recorded for every line. Images are formed by sorting the lines of raw data into time frames corresponding to a specified heart cycle. To avoid distortions, the ECG system was optically decoupled.

3.2.2 MR Image Acquisition

To localize the desired position of the acquisition slice, a so-called ‘localizer’ sequence was applied first as shown in Fig. 3.4. For this the TrueFISP sequence type was used. Ten sagittal image sections were recorded with a voxel size of $2.9 \times 2.9 \times 4.5 \text{ mm}^3$ using a 80×128 matrix. The total scan time for the localizer image was 8.5 seconds. Further scan parameters include $TE = 1.28 \text{ ms}$, $TR = 400 \text{ ms}$, flip angle $\alpha = 55^\circ$ and bandwidth = 1150 Hz/pixel.

Pulse Wave Velocity Measurements

Compliance can also be determined from pulse-wave velocity [5]. Only the phases of the complex MR signal of the recorded images as can be seen in Fig. 3.8 are used for blood flow determination.

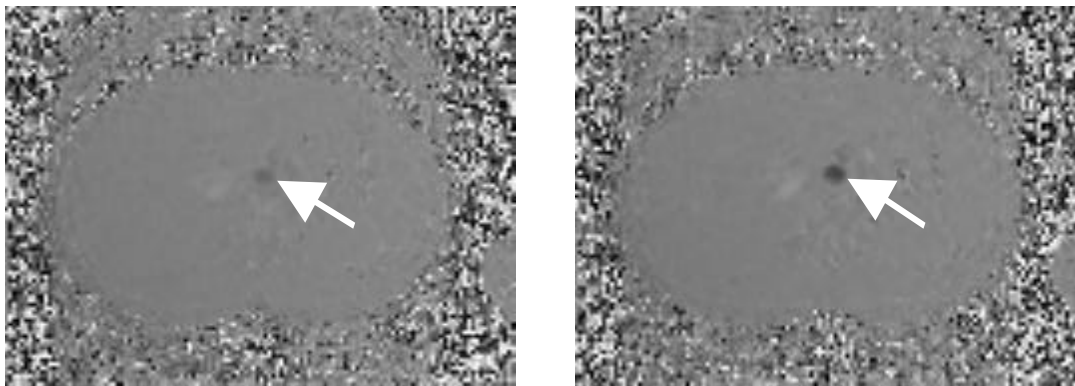


Fig. 3.8: Phase Images

The figures show two phase images from a total of 140 acquired images. The velocity of the blood flow corresponds directly to the phase of the complex MR signal (white arrow). The difference in phase from the left and right image above is proportional to the velocity of the spins.

By means of special gradient switching [31], the phase is proportional to the velocity of the spins and defined modulo 2π . The velocity corresponding to a phaseshift of π ,

the so-called 'velocity encoding' (VENC) was chosen to be 50 cm/s. For higher velocities, a phaseshift of 2π has to be considered when calculating the blood flow velocity (see also Fig. 3.15). As a velocity quantification pulse sequence we used a gradient-echo phase contrast sequence of the FLASH type. A slice of 6 mm thickness was excited by a $\alpha = 15^\circ$ flip angle. Other parameters were TE=2.9 ms, TR=11 ms, bandwidth=1370 Hz/pixel.

A matrix size of 256 by 192 at a 75 % rectangular field of view of 34 cm in read out direction and 25.5 cm in phase encoding direction was applied, as high spatial resolution is not required for phase imaging. Normally these pulse sequences use the phase difference of a velocity encoded and a velocity compensated scan. But in order to save measurement time, only velocity-sensitive data were acquired. With this method retrospective gating was applied to obtain images according to the heart phases.

FLASH and TrueFISP Images

For image acquisition we used a 2D-FLASH sequence for black – and bright blood imaging (FOV: $18 \times 18 \text{ cm}^2$, matrix: 256×256 , slice thickness: $d = 1 \text{ cm}$) and a 2D-TrueFISP for bright blood imaging (FOV: $25 \times 25 \text{ cm}^2$, matrix: 256×256 , slice thickness: $d = 1 \text{ cm}$). The repetition time was TR = 60 ms for the FLASH sequence and TR = 56 ms for the TrueFISP including 13 segments per excitation. Further sequence parameters include: TE = 5 ms (TrueFISP: TE = 2 ms) and bandwidth = 130 Hz/pixel (TrueFISP: bandwidth = 888 Hz/pixel).

For the black blood technique we found that a flip angle of $\alpha = 30^\circ$ provides the best contrast. It is slightly higher than the Ernst angle $\alpha = 23^\circ$ calculated from equation (2.3) using T1 values of muscle tissue from Table 1.1.

Also for the bright blood imaging the flip angle and the slice thickness were adapted to optimize contrast for image processing. In order to get more signal for the inflowing blood, the flip angle was chosen to be high. Values of $\alpha = 40^\circ$ and $d = 1.2 \text{ cm}$ were found to deliver optimal contrast for image processing. Applying bright-blood technique to the TrueFISP sequence, a flip angle of $\alpha = 55^\circ$ was the best choice, as the Ernst angle calculated from equation (2.5) is also higher for TrueFISP.

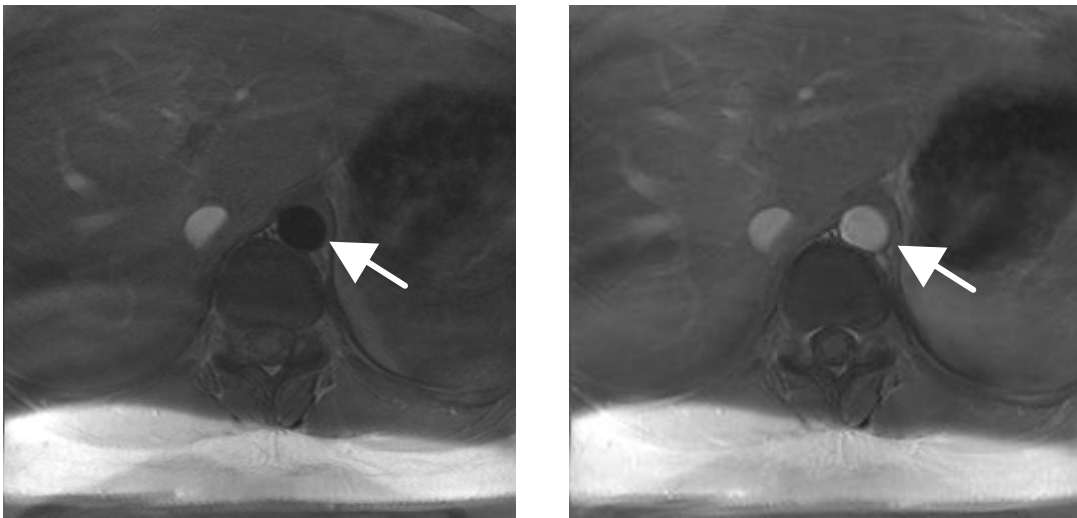


Fig. 3.9: MR FLASH Images of a Transversal Section

Transverse section of a black blood MR-FLASH image of the aorta (left arrow). The lumen appears black from the superior saturation band and the aortic boundary appears as a bright annulus around the lumen. The same transverse section recorded with bright blood MR-FLASH technique is depicted on the right hand side. The lumen appears bright from the inflow effect of the blood (right arrow).

The left image of Fig. 3.9 shows a typical axial black blood MR image of the aorta, where the lumen appears black from the superior saturation band and the aortic boundary appears as a bright annulus around the lumen. The right image of Fig. 3.9 shows the same aorta acquired by bright blood MR technique.

A TrueFISP image is depicted in Fig. 3.10 acquired from bright-blood technique. A image series of 18 images was acquired during using ECG-gating. TrueFISP imaging provides very good contrast and high signal as shown in the figure. The aorta wall is shown very clearly due to susceptibility artifacts between the blood and the surrounding tissue of the aorta.



Fig. 3.10: MR Image from TrueFISP Sequence

The depicted MR image is one of 18 acquired TrueFISP images during one heart cycle. Since the image is recorded applying bright-blood technique, the aorta appears as a bright circle in the center of the image (white arrow). The image was acquired with a field of view of $25 \times 25 \text{ cm}^2$ and a 256×256 matrix.

3.3 Determination of Aortic Compliance Using MRI

In this section, the results from MRI measurements are presented. Results from bright- and black-blood technique are compared with results from pulse-wave measurements. With these methods, compliance of the abdominal aorta of ten healthy volunteers aged from 27 to 38 was determined.

3.3.1 Automatic Image Segmentation of the Aortic Boundary

In Fig. 3.11 an example is shown where both bright- and black-blood images from the aorta are segmented. The pure image information that is used by the algorithm is the image gray value gradient.

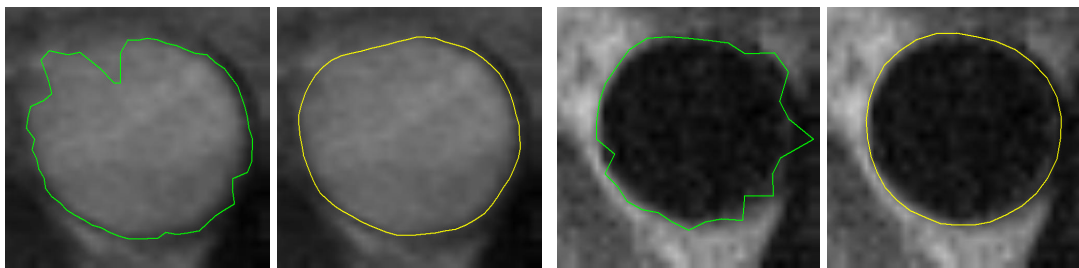


Fig. 3.11: Segmentation of Black- and Bright-Blood MR Images

The four images show segmented cross sectional area of a bright- (left two images) and black- (right two images) blood MR image of the aorta. The left image shows respectively the result from only considering the image information (here the image gradient ∇I).

Considering only the information from the image the resulting contour will fit along the maximum value of the gray value gradient as shown in Fig. 3.11. However, the

image gradient is not sufficient for image analysis. Only by applying both, the image and prior contour information, the correct contour can be found in the image.

3.3.2 Determination of Aortic Cross Sectional Area

To estimate the relative error of cross section measurements, the algorithm was applied several times to the same image but with different ‘seed points’ set by the operator and varying ‘balloon forces’.

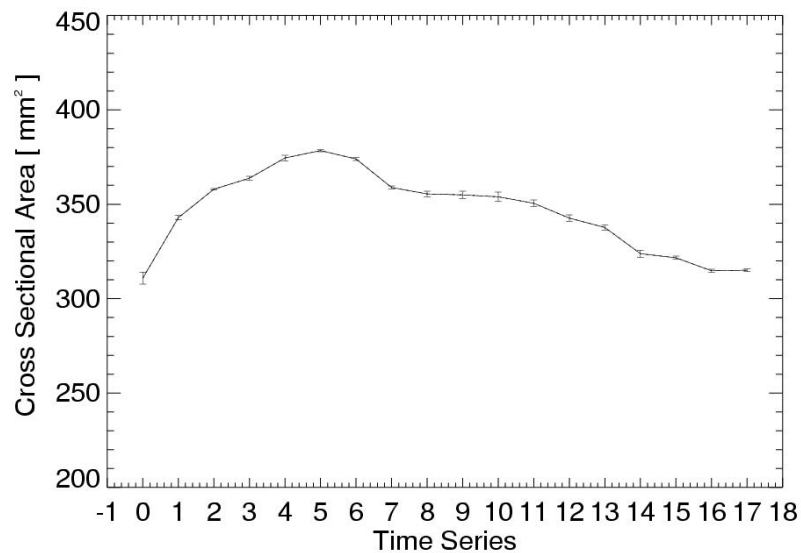


Fig. 3.12: Aortic Cross Sectional Area with Standard Deviation

The segmented aortic cross section during the cardiac cycle is depicted. The temporal change of the cross section between cardiac systole and diastole is shown with relative error determined from 5 segmentations using different ‘seed points’ of the same image. The errors come mainly from varying image quality during the cardiac cycle (flow artifacts). We found a standard deviation of $s_A = \pm 1.35 \text{ mm}^2$.

In addition, five image cubes from the same patient were acquired with each method described above. The standard deviation (Fig. 3.12) for aortic wall cross section

determination, was about 1 %. Pressure difference between systole and diastole was estimated by sphygmomanometry directly after the measurement using an arm cuff. To minimize the error in pressure estimation, an automatic pneumatic sphygmomanometer (Maglife C, Schiller Medical SA, Wissembourg Cedex France) was used. The error indicated by the manufacturer is $\pm 2\%$.

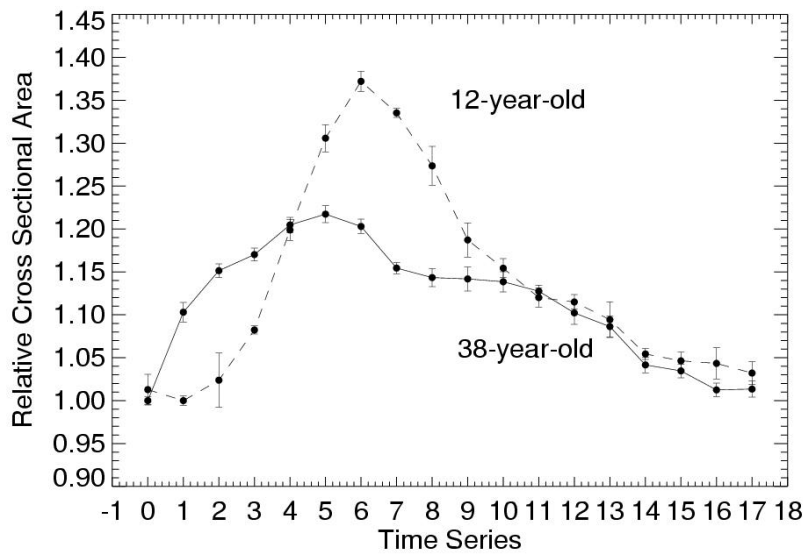


Fig. 3.13:Relative Aortic Cross Sectional Area

The values of aortic cross section area found by the algorithm are depicted and plotted during the entire cardiac cycle. The temporal change of the cross section between cardiac systole and diastole is shown. The dashed line represents the variance in aortic cross section of a 12-year-old patient. The solid line represents the values obtained from an adult volunteer. The indicated error were determined from several segmentations on the same image with different ‘seed points’.

A first result of these patient measurements was the significant difference of aortic cross sectional area expansion between a 38-year-old adult and a 12-year-old child. A comparison measurement of aortic cross section variance between them revealed an expected considerable decrease in aortic compliance with age as can be seen in Fig. 3.13. This is a preliminary result from a current patient study with young marfan patients.

3.3.3 Determination of Aortic Compliance from Ten Healthy Volunteers

Compliance of the abdominal aorta of ten healthy volunteers aged from 27 to 38 was determined from aortic cross section measurements and additionally using the pulse-wave velocity method. The former was conducted using a FLASH and TrueFISP sequence. The latter by using a gradient-echo phase contrast sequence of the FLASH type. The total measurement protocol took about 30 minutes.

Aortic Cross Sectional Measurements with FLASH and TrueFISP Sequences

After having localized the aorta with the localizer TrueFISP sequence, the acquisition slice was positioned directly over the diaphragm perpendicularly to the aorta (Fig. 3.4).

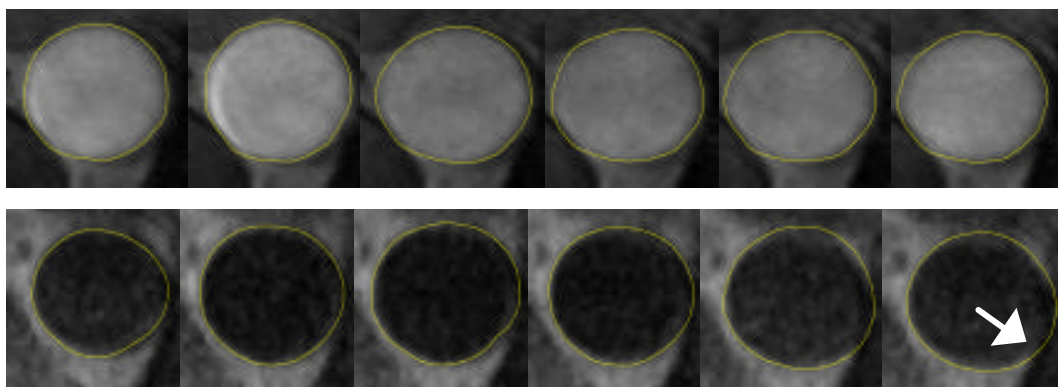


Fig. 3.14: Selected MR Images from the FLASH Sequence

Six images from a time series of 18 image are shown from each bright- (above) and black-blood (below) technique. The segmented aortic cross section through the entire cardiac cycle is drawn. The resulting contour appears as a bright annulus around the lumen. The MR image series from black blood technique (below) delivers lower contrast primarily at the end of the heart cycle. Flow artefacts (e.g. white arrow) on the first and last images of this series are also visible.

Images from black blood technique were then acquired. The presence of imaging artifacts and the low contrast between the outer arterial wall boundary and surrounding soft tissues made it impossible to get reliable results with this technique as seen in Fig. 3.14. In particular, these artifacts increase during diastole. But for the determination of the change in vessel cross sectional area and consequently for calculating aortic compliance, the measurement of diastolic cross section is crucial.

However, further measurements of a nine-year-old patient revealed that for very young subjects black blood technique provides much better results. In other relevant publications such as e.g. [8] and [25] black blood technique was always applied using spin-echo sequence. However, this image technique was not suitable for our objective, since it is essential for the determination of aortic compliance to acquire images throughout the entire cardiac cycle.

By applying the bright blood technique, it was possible to achieve sufficient image quality (Fig. 3.14) for all time frames over the entire heart cycle. Reliable results could be obtained from all ten healthy volunteers that were examined. Both the bright blood FLASH sequence and the bright blood TrueFISP sequence provide sufficient image quality for segmentation. After applying our active contour algorithm to each time frame of the acquired images, compliance of the aorta was calculated from equation (1.3).

Determination of Aortic Pulse Wave Velocity

In order to verify the resulting compliance from direct vessel distension measurements, pulse-wave velocity measurements were additionally performed to the same subjects. Two slices at a distance of $\Delta x = 56\text{mm}$ were placed around the acquisition slice from previous bright blood measurements shown in Fig. 3.4 on the left. For each slice, the onset of the pulse-wave was determined using the method described above. Fig. 3.15 shows an example of a pulse-wave with the fit lines defining the onset of the wave.

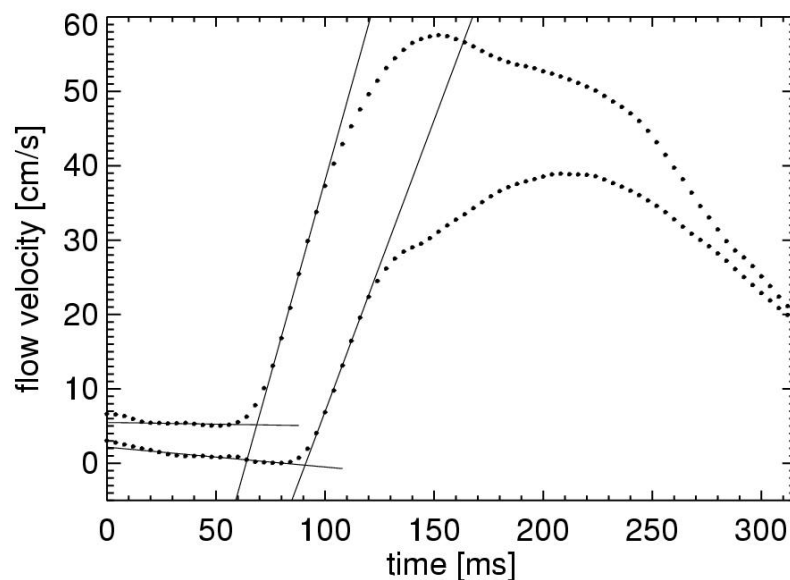


Fig. 3.15: Pulse Wave Measurements

Two typical corresponding flow profiles from two parallel slices at a spatial distance of $\Delta x = 54\text{mm}$ are depicted. The pulse-wave velocity can be calculated from the spatial distance Δx and the temporal difference Δt between the onset of the velocity peaks [5].

The pulse-wave velocity c is then calculated from the slice separation Δx and the time delay Δt between two selected flow curves as $c = \Delta x / \Delta t$. Compliance C was

determined using equation (1.4) assuming a constant blood mass density of $\rho = 1000 \text{ kg/m}^3$. As described elsewhere [5], the relative error of the pulse-wave velocity measurement is about 15 %. This is mainly due to the statistical uncertainty in the individual determination of the wave feet, considering the combined errors from two slices. We found in this work values for the pulse-wave velocity c between 3.75 and 6 m/s.

Comparison of Compliance Measurement Methods

The agreement of measured compliance between the presented methods has to be quantified in a reproducible way. The true compliance values are unknown. The obtained results from the measurements have to be evaluated by comparison. To this end, correlation methods are often used.

Mostly the very common pearsons correlation coefficient r is calculated as an indicator of agreement. Assuming a linear relationship between Y and X we can write $Y = aX + b$ which represents a straight line passing through the central section of the band of points. The pearsons correlation coefficient is then

$$r = \frac{\sum [(X - \bar{X})(Y - \bar{Y})]}{\sqrt{\sum (X - \bar{X})^2 \cdot \sum (Y - \bar{Y})^2}} \quad (3.6)$$

and represents the quality of correlation [30]. For straight lines there is a perfect positive correlation $r = 1$. No correlation would give $r = 0$.

However, by this method, the strength of a relation between the two variables is measured, not the agreement between them and we will have perfect correlation if the points lie along any straight line [3]. But for a first evaluation of the degree of agreement, pearsons correlation coefficient is very useful. In Table 3.2, the pearsons correlation coefficients r are listed for all three compliance measurement methods. The best data correlation results between the pulse-wave measurement and the

TrueFISP imaging method. The same result can be seen more qualitatively in Fig. 3.16. There, a plot of the data with the line of identity is shown for all three compliance measurements.

Table 3.2: Pearsons Correlation Coefficient

In this table the Pearsons Correlation Coefficient r was calculated for all three compliance measurement methods (FLASH-bright-blood, TrueFISP-bright-blood and pulse-wave measurements). The higher the coefficient r , the better the correlation of the methods.

Pears. Correl. Coeff. r TrueFISP-PulseWave Correlation	Pears. Correl. Coeff. r FLASH-PulseWave Correlation	Pears. Correl. Coeff. r TrueFISP-FLASH Correlation
0.94	0.88	0.83

Assuming perfect agreement of the methods, all points would lie on the bisecting line. The correlation plots reveal the deviation of data points from the bisecting line and thus the pearsons coefficient as printed in Table 3.2. For all measured volunteers within the age group of 20 to 30, compliance between $3 \cdot 10^{-5} \text{ Pa}^{-1}$ and $8 \cdot 10^{-5} \text{ Pa}^{-1}$ were observed. These values are in accordance with data given in the literature (e.g. [37]). The compliance shown in Fig. 3.16 for each of the three methods reveal good agreement of the values. However, a closer discussion of this result is necessary.

Another statistical approach was chosen, in addition to the determination of the pearsons correlation coefficient, emphasizing the difference between the measurement methods against their mean values.

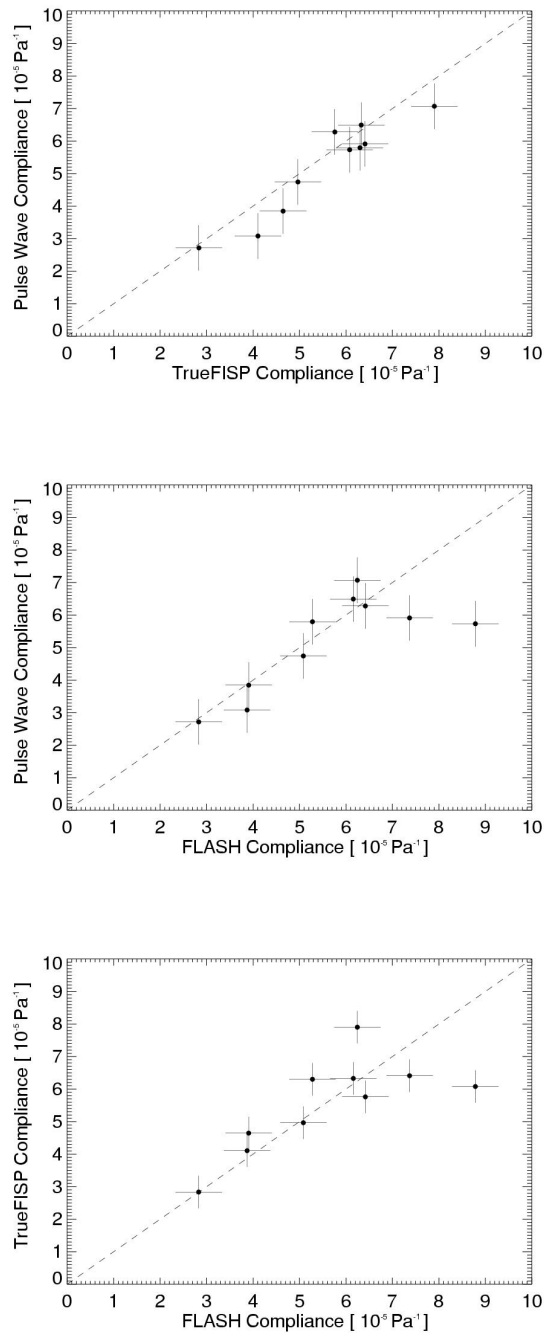


Fig. 3.16 Compliance Compared from three MR Methods

Compliance calculated from measurements of all three MR imaging methods are plotted respectively (FLASH-bright-blood, TrueFISP-bright-blood and Flow measurements (pulse-wave)). For each case the line of identity indicates perfect correlation of the compliance for the two techniques. The standard deviation in compliance measurements was $s_C = \pm 0.5 \cdot 10^{-5} \text{ Pa}^{-1}$ for cross sectional measurements and $s_C = \pm 0.7 \cdot 10^{-5} \text{ Pa}^{-1}$ for pulse-wave measurements.

Since we do not know the true value of compliance, the mean value of respectively two measurement methods is the best estimate available. A plot of the difference against either value separately will lead to a statistical artifact, as the differences are related to each other [3].

Table 3.3: Mean of Differences

The table shows the mean of differences \bar{d} between the three measurement methods (FLASH-bright-blood, TrueFISP-bright-blood and Flow measurements (pulse-wave)) and standard deviation s , using the Bland Altman method.

Compliance	Mean of Difference \bar{d} [10^{-5} Pa^{-1}]	Standard Deviation of Difference s [10^{-5} Pa^{-1}]
TrueFISP – PulseW.	0.325	0.473
FLASH – PulseWave	0.401	1.110
TrueFISP – FLASH	-0.049	1.213

Since there is no obvious relation between the difference and the mean, the lack of correlation can be calculated by the mean of all differences \bar{d} between two methods and the standard deviation of these differences (s). It is expected that most of the differences lie between $\bar{d} - 2s$ and $\bar{d} + 2s$. If we assume a Gaussian distribution, 95 % of differences will lie between these limits, which is called ‘confidence interval’ (CI).

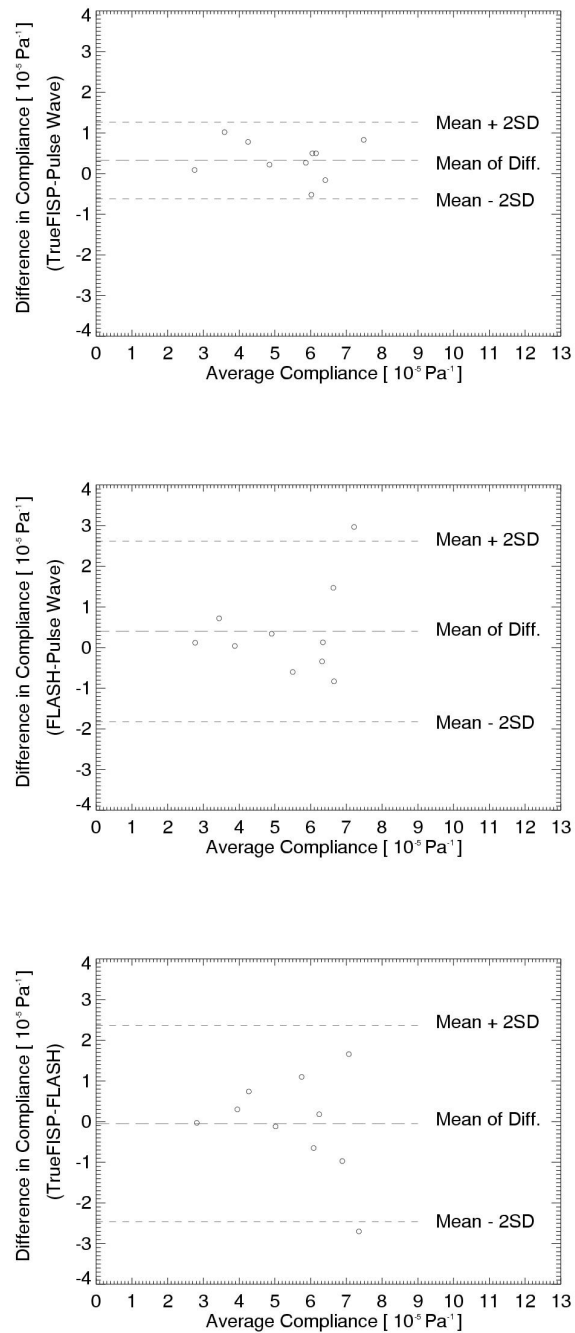


Fig. 3.17: Bland-Altman Plot of Compliance

A Bland-Altman plot of the difference between each two methods versus their mean is shown for all three MR techniques (FLASH-bright-blood, TrueFISP-bright-blood and Flow measurements (pulse-wave)). Also shown is the mean difference (middle line) and the confidence interval (CI).

The results of using the Bland and Altman method are presented in Table 3.3 and Fig. 3.17. In Table 3.3, the mean of difference in compliance is listed along the 95 % confidence interval and the standard deviation of the difference. The table reveals that the mean of difference is small for all three methods. The detailed Bland and Altman plot in Fig. 3.17. shows, that the mean of difference is distributed evenly for all three plots. The strongest correlation in compliance is shown by TrueFISP and pulse-wave measurements. These two methods reveal a very evenly distribution and a very small standard deviation. The TrueFISP measurement averages the signal better than the FLASH sequence does and provides also stronger signal. The FLASH imaging method has the largest lack of correlation compared to the other techniques. Assuming that all differences in compliance of our three methods lie within the CI (which is only the case for one), we could use all three methods for compliance measurements interchangeably. But the maximum difference of $2.8 \cdot 10^{-5} \text{ Pa}^{-1}$ in compliance as shown in Fig. 3.17 is unacceptable for clinical purposes.

3.4 Results from CT Measurements

Multi-slice CT (MSCT) with retrospective multi-phase ECG-gating can provide cardiac images at high temporal resolution [6]. The CT images from patients used in this work stem from CT angiography measurements which are widely used in the diagnosis of aortic diseases such as aortic aneurysm. As no blood pressure data from the patients were available from these measurements, we determined only the change in cross sectional area of the aorta and not the aortic compliance from equation (1.3).

In the first section these CT measurements are validated by means of a phantom setup. The contour algorithm is then applied to these images. In the following section, preliminary results of its application to patients data are presented. All experiments were performed using a multi-slice spiral CT scanner (SOMATOM Volume Zoom; Siemens Medical Solutions, Erlangen, Germany). Retrospective ECG-gating was added to an otherwise standard CT angiography protocol. Since the temporal resolution of the acquired images depends on the relation between heart rate and scanner rotation time, 4 rotations yield a temporal resolution between 90 and 250 ms. For the phantom experiments, a heart rate of 70 beats per minute was used and hence a temporal resolution of 140 ms was obtained. Taking oversampling into consideration as explained in Fig. 2.7, 20 time frames were calculated. The spatial resolution was $0.39 \times 0.39 \times 10 \text{ mm}^3$.

3.4.1 CT Measurements with Phantom Setup

In order to test the accuracy of aortic cross sectional segmentation using CT imaging, a physical phantom was constructed by [26]. It provides an artificial pulsatile circulation through ex-vivo porcine aortic specimens. A schematic drawing of the phantom setup is shown in Fig. 3.18. Water flows from a reservoir into a computer-controlled pulsatile pump. Two valves and a pneumatically driven piston provide a

pulsatile flow entering the porcine aortic specimen. The specimen is located inside a water-filled chamber.

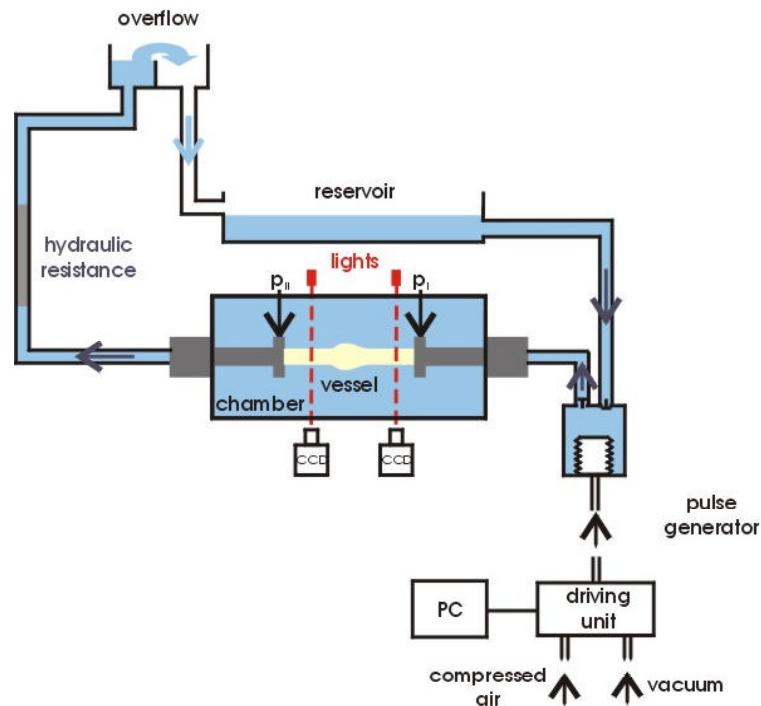


Fig. 3.18: CT Phantom Setup

The figure shows a schematic drawing of the phantom setup used for the determination of aortic elasticity. The aortic specimen is located inside a water-filled chamber. A computer-controlled pulsatile pump, consisting of a cylinder with two valves and a piston, pipes water from a reservoir in the porcine aortic specimen.

Systolic pressure can be tuned by a hydraulic resistance, diastolic pressure by an overflow chamber, which can be adjusted in height. Seven specimens of porcine aorta with a length of approximately 20 cm were used for the experiment. A pulse pressure of 40 mmHg and a pump frequency of 70 beats per minute was applied. The entire phantom setup was put onto the patient table of the CT scanner. The scanning parameters were 120 kVp, 150 mAs, with 2.5 mm collimation, a pitch of 0.375, and a scan length of 25 cm.

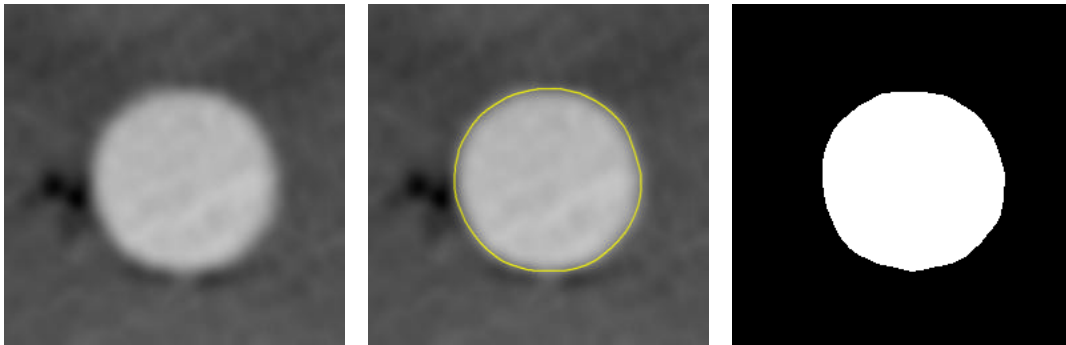


Fig. 3.19: CT Images from Phantom Setup

The resulting CT images from the phantom setup (left) are first segmented by the developed active contour algorithm (middle) and using a simple gray-scale threshold (right). The cross sectional area was then calculated from both methods,

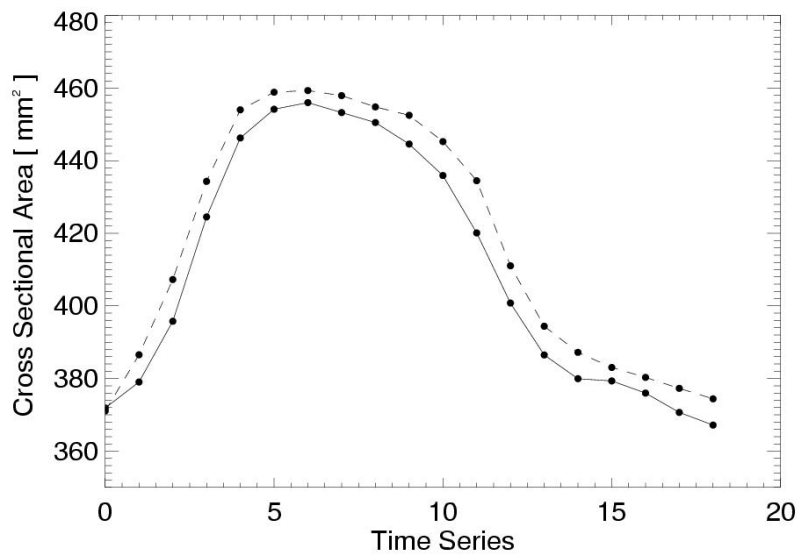


Fig. 3.20: Temporal Change of Aortic Cross Sectional Area

The resulting aortic cross sectional area from the porcine aortic specimens is shown. The solid and dashed line represent data from the threshold method and active contours respectively. A standard deviation of the cross sectional area, resulting from several segmentations on the same CT image, revealed a value of $s_A = \pm 0.5 \text{ mm}^2$. This value is smaller than the shown symbols.

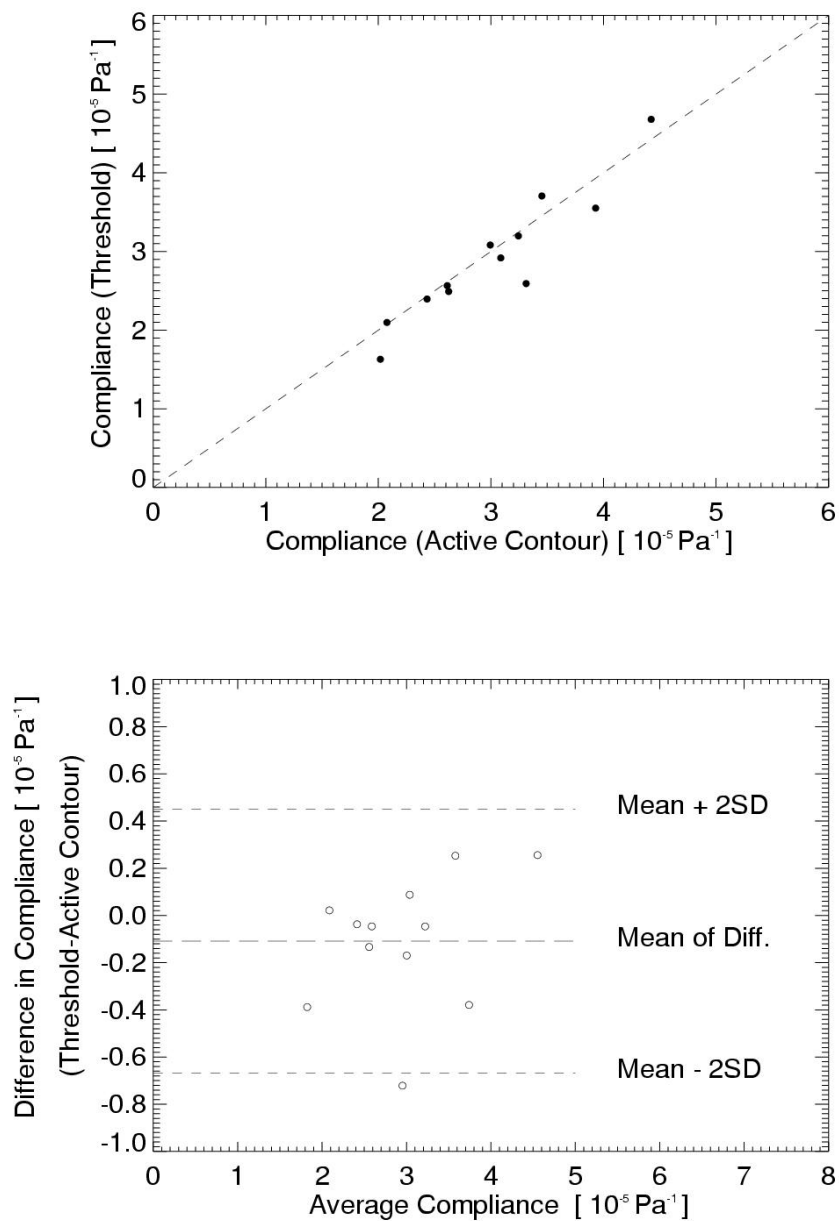


Fig. 3.21: Results from CT Phantom Measurements

The plot on the top shows the calculated compliance from both segmentation methods. The Pearson's correlation coefficient $r=0.94$ reveals a very good correlation between the methods. The standard deviation is in the order of $s_C=\pm 0.02 \cdot 10^{-5} \text{ Pa}^{-1}$ (see text) and thus smaller than the size of the symbols. The Bland-Altman plot of the difference in compliance between the two methods versus their mean is shown on the bottom.

For retrospective gating, an artificial ECG-signal was recorded during the measurement using a separate PC. For each of the seven specimens, two positions were analyzed, resulting in 12 compliance values.

Since the resulting images from this phantom measurements revealed good contrast between the surrounding water and the contrast-medium inside, a simple threshold segmentation was used to compare the results with those from our active contour algorithm (see Fig. 3.19). In Fig. 3.20 a plot of the resulting aortic cross sectional area as a function of time for both segmentation methods is shown.

To evaluate the error made by cross sectional area determination, the segmentation was made several times on the same image with different ‘seed points’. A standard deviation of $s_A = \pm 0.5 \text{ mm}^2$ was found, which is smaller than the size of the data points in Fig. 3.20.

Table 3.4: Results from Phantom Measurements

The results from applying the active contour and a simple threshold method on the CT images obtained from phantom measurements. The Pearson's correlation coefficient from Fig. 3.21 (top) and the results from the Bland-Altman plot in Fig. 3.21 (bottom) indicate the agreement of correlation between the two segmentation methods.

Pearsons Correl. Coeff. r	Mean of Difference \bar{d}. [10⁻⁵ Pa⁻¹]	Standard Deviation of Difference s [10⁻⁵ Pa⁻¹]
0.94	- 0.1	0.28

The mean compliance of all measured aorta was $(2.9 \pm 0.8) \cdot 10^{-5} \text{ Pa}^{-1}$ for the threshold method and $(3.0 \pm 0.7) \cdot 10^{-5} \text{ Pa}^{-1}$ for the segmentation by our active contour algorithm. The determined compliance of all 12 measurements are plotted in Fig. 3.21. There, the results in compliance are mutually compared (top). The line of

identity indicates the agree of correlation for both segmentation methods. A repeated segmentation of the obtained CT images revealed for both methods a standard deviation of only $s_C = \pm 0.02 \cdot 10^{-5} \text{ Pa}^{-1}$. Therefore the error bars in Fig. 3.21 are smaller than the indicated data points.

A more quantitative analysis is shown in Fig. 3.21 (bottom). The calculated Pearson's correlation coefficient of $r=0.94$ reveals a very good agreement of the two applied segmentation methods. The Bland-Altman plot shows the average of compliance versus the difference between the two segmentation methods. Since the mean of differences in compliance is $\bar{d} = -0.1 \text{ pa}^{-5}$ there is no substantial bias between the two methods. Most of the differences (95%) lie between $\bar{d} - 2s$ and $\bar{d} + 2s$ if a Gaussian distribution is assumed [3]. The deviation of compliance was found to be $2s = 0.56 \text{ pa}^{-5}$ indicating a very good correlation between the two methods.

The results are summarized in Table 3.4. There, the calculated Pearson's correlation coefficient is indicated, as well as the found mean of difference and the standard deviation of difference.

3.4.2 CT Measurements with Patients

CT raw data from routine angiography measurements (protocol: 120 kVp, 150 mAs, 1 mm collimation, pitch 0.375) were used to obtain a time resolved image set for aortic cross sectional determination. Thus images from the upper part of the descending thoracic aorta can be analyzed.

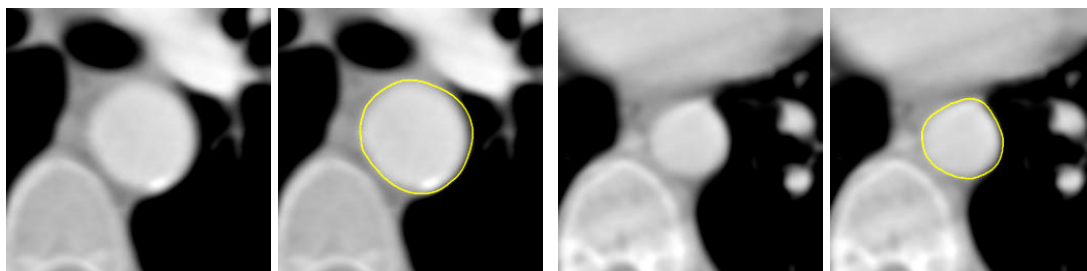


Fig. 3.22: Segmentation of Aorta Cross Sectional Area

The images show CT cross-sections of the thoracic aorta of a 70-year-old patient with coronary heart disease (left) and a young healthy patient (right images). On the right of each image, the result of the automatic active contour segmentation is depicted. The shown contour is here slightly larger around the aorta than the found contour really is, for the sake of depiction.

Preliminary results from CT measurements applied to two patients are presented in the following. The images in Fig. 3.22 show the aortic cross sectional measurements of a 70-year-old patient with coronary heart disease and a young patient without aortic disease. It can be seen, that the developed active contour model is able to find the aortic boundary without any problems. The result from the segmentation algorithm is presented in Fig. 3.23, where the relative vessel area is plotted versus the time frames within the cardiac cycle from all 20 images. From this plot, the considerably reduced vessel area change in the older patient is evident. Also the increased error in relative cross sectional area determination. Compared to images from the phantom measurement (Fig. 3.19), the contrast is much lower in images

from patients (Fig. 3.22). As no blood pressure data were available from these measurements, the compliance could not be computed.

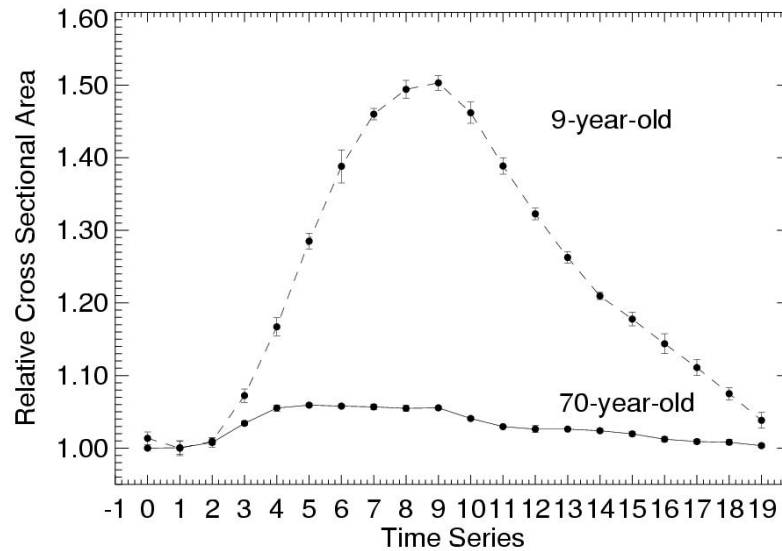


Fig. 3.23:Relative Aortic Cross Sectional Area

Relative cross sectional area from CT measurements of two patients at different age. The plot of all 20 aortic cross sections variance through the entire heart cycle is shown. The change of vessel area of the older patient (70 -year-old) is considerably reduced compared to the nine-year-old patient. The error shown here is much higher compared to the phantom measurement, because of less contrast between the aorta and the surrounding tissue.

Chapter 4

Discussion

The elasticity of the aortic wall is an important functional parameter, which is negatively correlated with ischaemic heart disease, as well as age. Thus, the decrease of the aortic compliance might be able to predict atherosclerotic changes before they become morphologically apparent. Furthermore, it might be useful in the characterization of aortic aneurysms.

Elasticity is usually quantified by the compliance C and can be determined by ex-vivo measurements using isolated specimens [32, 41, 39]. Recently there has been a lot of progress in non-invasive imaging of the vascular system using MRI and multi-slice CT. However, these methods do not provide information about the function of the vessel wall, such as the compliance. It would therefore be interesting to measure compliance non-invasively.

Several methods have been proposed, such as pulse-wave velocity measurement employing either MR velocity mapping or Doppler ultrasound. Also, methods have been proposed which monitor the change of the vessel cross-sectional area during the cardiac cycle, using MRI and ultrasound. From the change in cross-sectional area between systole and diastole and estimating the corresponding intra-arterial pressure difference, compliance can be determined.

In this work we have presented non invasive MR and CT measurements to determine aortic compliance. An active contour algorithm was developed to segment fully automatically the aortic boundary through the entire cardiac cycle. This algorithm could be applied successfully on both MR and CT images. To obtain MR images with sufficient quality, several imaging techniques have been implemented, such as bright- and black-blood MRI with fast FLASH and TrueFISP sequences. Furthermore, the active contour algorithm was applied to multi-slice CT images based on retrospective multi-phase ECG-gating. The accuracy of this method was tested on porcine aortic specimens using a phantom setup.

Automatic Determination of Aortic Cross Sectional Area

Since manual outlining of the aortic boundary is a very time-consuming process and depends on operator variability, it is not applicable in larger patient studies. In this work an active contour algorithm was developed for fully automatic vessel segmentation through the entire heart cycle. In the past, an automatic outlining of the aortic wall has been rejected because of imaging artifacts and low contrast between the arterial wall and surrounding tissue. Thus, in previous work the outlining of the aortic border was conducted manually using a mouse [8] or by semi-automatic techniques, where the initial curve has to be defined near the desired edge by an operator [25]. However, this approach requires as much time as tracing the contour manually and the reproducibility is still limited by the operator's bias. Furthermore, an operator defining edges tends to consider only small local sections of the aortic boundary, whereas an automatic algorithm considers the entire boundary during adjustment to the aortic wall. Thus, only a fully automatic segmentation can be highly reproducible.

In our model, the operator sets only one ‘seed point’. Nevertheless, our experiments revealed that depending on image quality it is necessary to intervene. But in order to limit the required interaction of the operator, only one parameter can be tuned additionally. This parameter influences the ‘balloon force’ of the inflating contour. It is hence possible to push the curve into desired areas of the image or respectively away from problematic image areas. For the images used in this work, this operator interaction was always sufficient to find the desired contour. Only for images with strong artifacts it does not work, but on these images the aortic contour is hardly visible even with the eye. And the human perception finally evaluates the resulting contour.

With the developed active contour model some problems inherent in existing models could be overcome. The problem of clustering of vertices near strong image features could be solved by allowing each vertex to move only radial from the ‘seed point’ to the aortic boundary. Furthermore, to avoid shrinking or even imploding of the contour due to the internal force, the internal energy term was set to be low for the parts of the contour where the curvature is circular. Another problem of the original ‘snake’ model was an oscillating around local minimums during the iteration process. This could be solved by performing the deformation process as a time integrating process.

The application of the algorithm to computer-generated images revealed, that for SNR of better than 3, segmentation of a simple circle is reproducible and almost independent of the initial ‘seed point’. Applying the algorithm on the identical MR image but with different ‘seed points’, a variability of the cross sectional area of less than 1% was found for both FLASH and TrueFISP MR images, but also for the CT measurements, depending always on image quality.

MRI Measurements

MRI of the aorta is the first technique to directly and noninvasively measure vascular compliance via the change in aortic cross sectional area without harmful radiation. MR cross section measurements are usually made by averaging images around the diastole and systole of the heart. Thereby, two separate spin-echo images are required as near as possible to the systolic and diastolic heart phase. Thus, with these conventional spin-echo sequences, a temporal resolution of the change in aortic cross sectional area is not possible. To obtain data with a sufficient temporal and spatial resolution, fast imaging sequences are necessary. They have lower inherent image contrast, but superior temporal resolution.

In this work we showed that it is possible to acquire MRI images through the entire cardiac cycle without using any contrast agent. We used gradient-echo sequences such as FLASH and TrueFISP with bright- and black-blood techniques to enhance contrast between the aortic boundary and the surrounding tissue. To this end, temporal image series were acquired perpendicular to a chosen part of the aorta (above the diaphragm) and then segmented.

The experiments revealed that bright-blood technique delivers a more homogenous blood signal and less artifacts than black-blood technique. Using the latter, image quality was found to be not good enough for vessel segmentation, primarily during diastole the artifacts near the aortic boundary are substantial. However, younger patients provided much better images with less artifacts, although the determined blood flow velocity was lower for younger subjects and hence the condition according to equation (3.5) is less true.

We speculate that a reason for that might be turbulent blood flow due to e.g. plaques on the aortic wall with increasing age. These artifacts may hinder the blood flow and thus less saturated blood is flowing into the image slice. The relatively static but turbulent blood flow in diastole induces artifacts. Since this flow void cannot be distinguished from the saturated static surrounding tissue, contrast is getting poorer as can be seen on the black-blood images in Fig. 3.14. However, this effect influences equally the images made by bright-blood technique. That is why also bright-blood images from younger subjects provide better contrast. Nevertheless, for older patients this effect seems to be stronger using black-blood technique than in bright-blood images.

Ten volunteers with no known cardiovascular disease were scanned using the bright-blood imaging method with FLASH and TrueFISP. To ensure that the aortic area is measured at the same points in the cardiac cycle for each volunteer, 18 images were computed from the ECG gated acquisitions for all subjects. In order to compare the resulting compliance from these direct vessel distension measurements, pulse-wave velocity measurements of high spatial resolution were additionally performed to the same subjects.

We found a mean value for the pulse-wave velocity of 4.5 m/s which is in accordance with data from literature [33]. The deviation expected in pulse-wave velocity determination is on the order of 15 % and is due to the combined statistical uncertainty in the individual determination of the two wave feet [5]. The image quality was totally sufficient for the determination of the image phase. An increase with age of the pulse-wave velocity could be determined with values up to 6 m/s for the oldest volunteer (38-year-old).

The disadvantage of pulse-wave velocity determination is, that it can only be measured reproducibly over a relatively long arterial segment and requires high-fidelity fit lines defining the onset of the wave. The operator needs a lot of experience to determine the wave foot. That is why the error in compliance

determination is higher for pulse-wave measurements than for cross sectional area determination. We found a standard deviation in aortic compliance determination of 7% ($s_C = \pm 0.7 \cdot 10^{-5} \text{ Pa}^{-1}$) for pulse-wave measurements and 5% ($s_C = \pm 0.5 \cdot 10^{-5} \text{ Pa}^{-1}$) for cross sectional measurements. The operator's bias is less important for segmentation, as the final curve is smoothed and the operator has the possibility to evaluate immediately the found contours during the heart cycle. Nevertheless, image quality gets more important and mainly image artifacts can distort the result, whereas, using pulse-wave measurements, image quality has far less impact on the result.

Applying the three mentioned imaging methods, for all ten volunteers within the age group of 20 to 30, compliance between $C = 3 \cdot 10^{-5} \text{ Pa}^{-1}$ and $C = 8 \cdot 10^{-5} \text{ Pa}^{-1}$ were determined as seen in Fig. 3.16 and Fig. 3.17. These values are in excellent accordance to data given in [37]. There, the age-dependency of aortic compliance (which is called aortic distensibility in [37]) is presented and corresponds to the values found for the age group of the volunteers in this work.

Furthermore, preliminary results from two patient studies in MRI and CT confirm the age-dependency of aortic compliance. The relative change in cross sectional area of the aorta from MR measurements shown in Fig. 3.13 reveal values of 1.37 for a 12-year-old child and 1.16 for a 38-year-old adult. The CT measurements have shown values of 1.07 for a 70-year-old patient and 1.5 for a 9-year-old child (Fig. 3.23). Thus, there is a substantial decrease in change of aortic cross sectional area with age. This first result from two ongoing studies reveal the reproducibility of both MRI and CT compliance measurement.

However, assuming that all differences in compliance of our three methods are lying within a small 'confidence interval' of the Bland-Altman plot in Fig. 3.17, all three methods for compliance measurements are interchangeable. But the maximum difference of $2.8 \cdot 10^{-5} \text{ Pa}^{-1}$ in compliance as found in Fig. 3.17 is unacceptable for clinical purposes. Only TrueFISP and pulse-wave measurements provide a suitable

‘confidence interval’ of $\pm 0.9 \cdot 10^{-5} \text{ Pa}^{-1}$. Some values are even identical, which is an astonishing result, considering the difference of the two methods. Thus, these two methods reveal a very evenly distribution and very small standard deviation. They show the best correlation in compliance.

The FLASH imaging method shows the worst correlation compared to the other techniques. Results from FLASH imaging provide the largest deviation of compliance compared with the two other methods. The confidence interval is larger than $\pm 2 \cdot 10^{-5} \text{ Pa}^{-1}$. Since the image quality is the major factor affecting reproducibility of aortic wall segmentation FLASH images provide poor contrast and more artifacts and hence, it is difficult to define the endothelial border of the aorta even with the eye. TrueFISP images (as shown in Fig. 3.10) provide much better signal and image contrast. On the other hand, the susceptibility artifacts from TrueFISP between different tissues may intensify the dark annulus around the aorta (Fig. 3.10) in addition to the typical T2/T1 weighted TrueFISP contrast.

Another reason for the slightly worse performance using the FLASH sequence may be that the signal of flowing blood becomes significantly higher during systole, because of higher blood flow velocity as shown in Fig. 3.15. Since the aortic boundary segmentation is made by tracking around the bright respectively black signal from the flowing blood, a problem may be that the vessel appears larger than it is during systole. This might be the reason for the larger difference (confidence interval mentioned above and in shown in Fig. 3.17), when comparing the two result in compliance of the two methods. Although the accuracy in cross sectional determination is similar for FLASH and TrueFISP the resulting compliance differ. The TrueFISP sequence is less susceptible to this problem because of the better contrast. Thus, while both methods (FLASH and TrueFISP) demonstrated good correlation (Fig. 3.16), the TrueFISP technique performed better. That is why we have more confidence in the TrueFISP technique (see Table 4.1 below)

Misalignment of the slice from the perpendicular may cause overestimation of the aortic cross sectional area. But this error is expected to be low (less than 1.5 % for an angle of 10° from the perpendicular), because both the systolic and diastolic images are affected and the compliance is computed by the relative change in cross section.

Another uncertainty might be the indirect measurement of arterial pressure in humans by sphygmomanometry. However, comparisons with direct pressure measurement using an intra-arterial manometer have revealed similar accuracy of both methods [32]. Furthermore, it might be a problem, that the MRI compliance measurements presented in this work are not real time techniques. The acquired images are averaged through a number of cardiac cycles. And thus the pulse pressure measured only one time before and after the session does not truly reflect the blood pressure, which may change during the image acquisition. Therefore, in an ongoing patient study, we will average a number of values obtained during the measurement by an automatic pneumatic sphygmomanometer already used in this work. We use the same tool for the CT patient study. An error of less than $\pm 2\%$ was indicated by the manufacturer.

CT measurements

Although it is possible to measure aortic compliance with multi-detector CT [6], this method has not yet been applied to compliance measurements. However, CT angiography is widely used in clinical routine and might therefore be a practicable method for compliance measurements. Thus, morphological and functional information could be acquired at the same time by integrating compliance measurements into a routine CT angiography study using retrospective multi-phase ECG-gating. The total examination lasts for less than one minute.

The accuracy of computed tomography for compliance determination was tested by means of an experimental phantom setup, which is able to generate an artificial

pulsatile circulation through ex-vivo porcine aortic specimens. The limitation of this phantom study is the dependency of the temporal resolution of ECG-gated CT on the heart rate [21]. Although the CT method may perform worse at certain heart rates, the applied temporal resolution of 140 ms is typical for a retrospective multi-phase ECG-gating algorithm.

Applying the developed active contour algorithm on 12 phantom measurements, a mean value of $C=(3.0 \pm 0.7) \cdot 10^{-5} \text{ Pa}^{-1}$ for the compliance was found, which is in accordance with values reported in the literature [28]. By comparison with results from MRI compliance measurements in this work, the CT values are in the lower area of compliance. It indicates that porcine aorta is a reasonable model.

Applying additionally a simple threshold segmentation, we found a mean compliance of $C=(2.9 \pm 0.8) \cdot 10^{-5} \text{ Pa}^{-1}$. This good correlation between the two segmentation methods emphasizes the reliability of the CT method for compliance determination. A Bland-Altman analysis reveals that the error in compliance measurements can be expected to be about $\pm 0.56 \cdot 10^{-5} \text{ Pa}^{-1}$. Since the values found from MRI measurements in this work and from literature lie between $C=3 \cdot 10^{-5} \text{ Pa}^{-1}$ and $C=8 \cdot 10^{-5} \text{ Pa}^{-1}$ a sensitivity of $0.56 \cdot 10^{-5} \text{ Pa}^{-1}$ is sufficient. Primarily, major compliance changes related to aortic diseases can be detected very accurately. However, the good correlation is not surprising, as the phantom setup provides very good image contrast, which is not available using patient data.

Preliminary results from CT measurements applied to two patients reveal that changes due to age and vascular disease can be detected. A simple threshold method for aortic boundary detection is not feasible with patient data, because of the weak contrast of surrounding tissue. However, the active contour algorithm is able to segment without problems the aortic boundary even when calcifications are present. However, a comparison of the relative cross sectional area determination (as no blood pressure data were available from CT measurements) from MRI (Fig. 3.13) and CT (Fig. 3.23) revealed a similar deviation. We found an error of ± 0.012 for

relative cross section in CT and ± 0.012 for relative cross section in MR. As for compliance determination, only the blood pressure has to be additionally considered, the same error in compliance determination for MR and CT measurements can be assumed.

An ongoing systematic study of patients with aortic aneurysms is expected to show that CT compliance measurements in patient is a accurate method to detect vascular diseases early. In this work it was shown, that CT is a feasible method for compliance measurements.

Table 4.1: Evaluation of the Different Methods

The table shows the most important criteria for compliance measurements and a conclusion in the last line. The symbol '+' always means advantageous and thus e.g. less dependence on operator bias. The symbol '-' means disadvantageous and thus e.g. a strong radiation; 'O' lies somewhere between but could be improved.

	MR Pulse Wave	MR TrueFISP	MR FLASH	CT
Image Quality	+	++	O	+
Operator Bias	-	+	+	+
Radiation	+	+	+	-
Compliance Accuracy	+	++	O	+

Chapter 5

Summary and Outlook

Elasticity of the aortic wall is an important functional parameter, which can be quantified by compliance measurements. The elasticity of vessels is decreasing with age and depends on cardiovascular diseases. A decreased compliance of the aorta might be able to predict atherosclerotic changes before becoming morphologically apparent. Currently, the methods for compliance measurements are limited and mostly invasive. In this work we present a method for non-invasive aortic compliance measurements from MR and CT images.

MR imaging is a very accurate and non-invasive technique for the assessment of the aortic cross sectional area. Using retrospective ECG-gating, we could acquire time resolved images from the aorta. By means of FLASH and TrueFISP sequences, images with sufficient temporal (60ms) and spatial (0.7mm) resolution could be acquired for image processing. To enhance contrast between endothelium and lumen, bright- and black-blood techniques were implemented. However, only the bright-blood method presented sufficient image quality. The black-blood technique provided useful images only from very young subjects.

A segmentation algorithm was developed to outline the vessel wall automatically and determine the change of vessel cross-sectional area between systole and diastole. Applying our contour model to the MR images, a variability of cross sectional area

determination of less than 1% was found for both FLASH and TrueFISP MR images, but also for the CT measurements.

Optimizing the temporal resolution to 60ms we obtained a relative error of 7% from TrueFISP- ($1.0 \times 1.0 \times 10 \text{mm}^3$, $\text{SNR} > 12$), FLASH- ($0.7 \times 0.7 \times 10 \text{mm}^3$, $\text{SNR} > 12$) and multi-slice CT- ($0.39 \times 0.39 \times 10 \text{mm}^3$, $\text{SNR} > 25$) measurements at volunteers. Pulse wave measurements yielded an error of 9%. This is mainly due to the operator's bias, when determining the wave foot of the pulse wave and thus, depends on the operator's experience. In a study of ten volunteers, a compliance between $C = 3 \cdot 10^{-5} \text{ Pa}^{-1}$ and $C = 8 \cdot 10^{-5} \text{ Pa}^{-1}$ was determined, depending on age. The results of the TrueFISP and the pulse-wave measurements agreed very well (confidence interval of $1 \cdot 10^{-5} \text{ Pa}^{-1}$) while the results of the FLASH method more clearly deviated from TrueFISP and pulse-wave (confidence interval more than $2 \cdot 10^{-5} \text{ Pa}^{-1}$) An increasing in compliance with age could be found from MR and CT measurements. Also multi slice CT was applied to compliance measurements. A phantom setup provided images with ideal contrast for aortic wall segmentation. The confidence interval of $0.56 \cdot 10^{-5} \text{ Pa}^{-1}$ found at a mean value of $C = 3.0 \cdot 10^{-5} \text{ Pa}^{-1}$ is sufficient to detect changes in compliance related to aortic diseases. But could not be achieved for patient data.

Preliminary results from two independent patient studies in MR and CT could confirm an age-dependent decrease of aortic compliance. The characterization of aortic aneurysms may be interesting, since so far no suitable parameter can reliably predict the individual risk of sudden aneurysm rupture so far. Furthermore, arterial compliance is negatively correlated with a number of diseases including atherosclerosis and hypertension. Therefore, an accurate determination of aortic compliance is indispensable.

The limitation of aortic cross sectional segmentation lies more in image quality than in image processing. Our experience with the active contour model revealed, that the algorithm only fails when the aortic wall is also not perceptible with the eye. Future efforts have to be made rather in imaging than in processing. The big advantage of

the TrueFISP sequence is the very good vessel contrast. Although the resolution of CT is favorable to cross section measurements, the contrast is poor for aortic cross section measurements. Future intravascular contrast agent might solve this problem. Determining the aortic compliance from pulse wave velocity is also a very accurate technique, as shown in this work, as image quality is not a restriction factor. The main error comes from the operator bias. There is no way to limit this uncertainty due to the determination of the wave foot. However our experiments revealed, that some experience of the operator improves the result considerably. Thus pulse-wave and TrueFISP measurements might be most advantageous for future studies in this field.

List of Figures

FIG. 1.1: VOLUME-PRESSURE RELATIONSHIP OF THE AORTA.....	7
FIG. 1.2: ZEEMAN ENERGY LEVELS.....	15
FIG. 1.3: ON-RESONANCE SPIN FLIP.....	19
FIG. 1.4: SPIN RELAXATION PROCESS	21
FIG. 1.5: COMPUTED TOMOGRAPHY.....	27
FIG. 1.6: CT MEASUREMENT SETUP.....	28
FIG. 1.7: THE HOUNSFIELD SCALE.....	30
FIG. 1.8: WINDOWING OF CT HOUNSFIELD VALUES	31
FIG. 2.1: GRADIENT ECHO SEQUENCE.....	45
FIG. 2.2: TRUEFISP SEQUENCE.....	47
FIG. 2.3: PRINCIPLE OF ECG-TRIGGERING.....	50
FIG. 2.4: PRINCIPLE OF ECG-GATING.....	51
FIG. 2.5: DIFFERENT SCANNER GENERATIONS.....	54
FIG. 2.6: PRINCIPLE OF SPIRAL CT	56
FIG. 2.7: RETROSPECTIVE CARDIAC GATING AND CT IMAGE FORMATION.....	57
FIG. 2.8: IMAGE FEATURE MAP	59
FIG. 3.1: SMOOTHED CURVE FROM AORTIC CROSS SECTIONAL AREA	66
FIG. 3.2: SIMULATED IMAGES	68
FIG. 3.3: SIMULATION HISTOGRAM.....	69

FIG. 3.4: MR LOCALIZER IMAGE OF A SAGITTAL SECTION.....	72
FIG. 3.5: FLASH SEQUENCE WITH BLACK BLOOD TECHNIQUE.....	73
FIG. 3.6: EFFECTIVE THICKNESS OF SATURATION LAYER.....	74
FIG. 3.7: ECG TRIGGERED MR IMAGES.....	77
FIG. 3.8: PHASE IMAGES.....	78
FIG. 3.9: MR FLASH IMAGES OF A TRANSVERSAL SECTION.....	80
FIG. 3.10: MR IMAGE FROM TRUEFISP SEQUENCE.....	81
FIG. 3.11: SEGMENTATION OF BLACK- AND BRIGHT-BLOOD MR IMAGES.....	82
FIG. 3.12: AORTIC CROSS SECTIONAL AREA WITH STANDARD DEVIATION.....	83
FIG. 3.13:RELATIVE AORTIC CROSS SECTIONAL AREA	84
FIG. 3.14: SELECTED MR IMAGES FROM THE FLASH SEQUENCE.....	85
FIG. 3.15: PULSE WAVE MEASUREMENTS.....	87
FIG. 3.16 COMPLIANCE COMPARED FROM THREE MR METHODS.....	90
FIG. 3.17: BLAND-ALTMAN PLOT OF COMPLIANCE.....	92
FIG. 3.18: CT PHANTOM SETUP.....	95
FIG. 3.19: CT IMAGES FROM PHANTOM SETUP.....	96
FIG. 3.20: TEMPORAL CHANGE OF AORTIC CROSS SECTIONAL AREA.....	96
FIG. 3.21: RESULTS FROM CT PHANTOM MEASUREMENTS.....	97
FIG. 3.22:SEGMENTATION OF AORTA CROSS SECTIONAL AREA	100
FIG. 3.23:RELATIVE AORTIC CROSS SECTIONAL AREA	101

List of Tables

TABLE 1.1: RELAXATION PARAMETERS.....	22
TABLE 3.1: VALUES OF SATURATION SLICE THICKNESS.....	75
TABLE 3.2: PEARSONS CORRELATION COEFFICIENT.....	89
TABLE 3.3: MEAN OF DIFFERENCES.....	91
TABLE 3.4: RESULTS FROM PHANTOM MEASUREMENTS	98
TABLE 4.1: EVALUATION OF THE DIFFERENT METHODS.....	112

List of References

- [1] Berne R M, Matthew N L (edts.).
Physiology
Mosby St. Louis USA 4th edition (1998)

- [2] Blake A.
Active Contours.
Springer, London, 2nd printing (2000)

- [3] Bland J M, Altman D G.
Statistical methods for assessing agreement between two methods of clinical
measurement.
Lancet i 307-10 (1986)

- [4] Bock M, Schad L R, Müller E and Lorenz W J.
Pulsewave velocity measurement using a new real-time MR-method.
Magnetic Resonance Imaging 13 21-9 (1995)

- [5] Boese J M, Bock M, Schoenberg S O and Schad L R.
Estimation of aortic compliance using magnetic resonance pulse wave
velocity measurement
Phys. Med. Biol. 45 1703-13 (2000)

- [6] Boese JM, Bahner ML, Albers J, et al.
Optimization of temporal resolution in CT using retrospective ECG-gating.
Radiology 40 123-9 (2000)

- [7] Cohen L D.
On Active Contour Models and Balloons Image Understanding.
Image Understanding 53 211-8 (1991)

- [8] Forbat S M, Mohiaddin R H, Yang G Z, Firmin D N and Underwood S R.
Measurement of regional aortic compliance by MR imaging: a study of reproducibility.
Magnetic Resonance Imaging 5 635-9 (1995)
- [9] Glasser S P, Arnett D K, Mc Veigh G E, Finkelstein S M, Bank A J, Morgan D J and Cohn J N.
Vascular Compliance and cardiovascular disease: a risk factor or a marker ?
Am J. Hypertens. 10 1175-89 (1997)
- [10] Goldstone J.
Surgery ed. L J Greenfield
Baltimore, MD: Lippincott, Williams and Wilkins. (1993)
- [11] Haacke M E, Brown R W, Thompson M R, Venkatesan R.
Magnetic Resonance Imaging, Physical Principles and Sequence Design.
John Wiley & Sons, New York (1999)
- [12] Haase A, Frahm J, Matthei D, Hannicke and Merboldt K D.
FLASH imaging: Rapid imaging using low flip angle pulses.
J. Magn. Reson. 67 256 (1986)
- [13] Hallock P and Benson I C J.
J. Clin Invest 16 595 (1937)
- [14] Hansen F, Mangell P, Sonesson B and Länne T.
Diameter and compliance in the human common carotid artery variations with age and sex.
Ultrasound Med. Biol. 21 1-9 (1995)
- [15] Hardy C J, Bolster B D Jr, Mc Veigh E R, Adams W J and Zerhouni E A.
A one-dimensional velocity technique for NMR measurement of aortic distensibility
Magn. Reson. Med. 31 513-20 (1994)
- [16] Hardy C J, Bolster B D Jr, Mc Veigh E R, Iben I E and Zerhouni E A.
Pencil excitation with interleaved fourier velocity encoding: NMR measurement of aortic distensibility
Magn. Reson. Med. 35 814-19 (1996)
- [17] Hounsfield G N.
Computerized transverse axial scanning (tomography). Part I.
Br J Radiol. 46 1016 (1973)

-
- [18] Jähne B, Haußecker H and Geißler P (eds.).
Handbook of Computer Vision and Applications.
Volume 2 Signal Processing and Pattern Recognition.
Academic Press (1999)
- [19] Jähne B.
Digital Image Processing.
Springer, 5th edition (2002)
- [20] Jähne B.
Handbook of Digital Image Processing for Scientific Applications.
CRC Press Boca Raton FL (1997)
- [21] Kachelriess M, Ulzheimer S, Kalender W A.
ECG-correlated image reconstruction from subsecond multi-slice spiral CT
scans of the heart.
Med Phys 27 1881-902 (2000)
- [22] Kalender W A.
Computed Tomography.
Springer Erlangen (2000)
- [23] Kass M, Witkin A and Terzopoulos D.
Snakes: Active Contour models.
Int. Journal of Computer Vision 1 321-31 (1987)
- [24] Keller A, Wilke J, Blumenstein R and Raue I.
Konventionelle Röntgen-Funktionsdiagnostik- Videometrie.
Z. Ges. Inn. Med. 47 480-3 (1992)
- [25] Ladak H M, Thomas J B, Mitchell J R, Rutt B K and Steinman D A.
A semi-automatic technique for measurement of arterial wall from black
blood MRI .
Med. Phys. 28 1098-107 (2001)
- [26] Leitermann D et al.
Center of Biomedical Engineering.
Czech Technical University Prag Czech Republic
- [27] Lobregt L and Viergever Max A.
A Discrete Dynamic Contour Model.
IEEE Transactions on Medical Imaging 14 12-24 (1995)

- [28] Milnor W R.
Hemodynamics.
Baltimore M D: Williams & Wilkins 2nd edn (1989)
- [29] Mohiaddin R H, Firmin D N and Longmore D B.
Age-related changes of human aortic flow wave velocity measured noninvasively by magnetic resonance imaging.
J. Appl. Phys. 74 492-7 (1993)
- [30] Mould R F.
Introductory Medical Statistics.
Institute of Physics Publishing Bristol 3rd edition (1995)
- [31] Nayler G, Firmin D N, Longmore D B.
Blood flow imaging by cine magnetic resonance.
J. Comput. Assist. Tomogr. 10 715-22 (1986)
- [32] Nichols W W and O'Rourke M F.
McDonald's Blood Flow in Arteries
Arnold London 3rd edn (1990)
- [33] O'Rourke M F and Mancia G.
Arterial stiffness.
J. of Hypertension 17 1-4 (1999)
- [34] Oppelt A, Graumann R, Barfuss H, Fischer H, Hertl W and Schajor W.
FISP: A new fast MRI sequence.
Electromedica 3: 15 (1986)
- [35] Radon J H.
Über die Bestimmung von Funktionen durch ihre Integralwerte längs gewisser Mannigfaltigkeiten.
Ber. vor Sächs. Akad. Wiss. 69 262-77 (1917)
- [36] Reiser M and Semmler W (eds.).
Magnetresonanztomographie.
Springer Berlin (1992)

- [37] Resnick L M, Militianu D, Cunnings A J, Pipe JG, Evelhoch J L and Soulen R L.
Direct magnetic resonance determination of aortic distensibility in essential hypertension: relation to age, abdominal visceral fat, and is situ intracellular free magnesium.
Hypertension 30 654-9 (1997)
- [38] Ross R.
The pathogenesis of atherosclerosis: a perspective for the 1990's.
Nature 362 801-9 (1993)
- [39] Sramek B B, Valenta J, Klimes F (eds.).
Biomechanics of the Cardiovascular System.
Czech Technical University Press Prague (1995)
- [40] Urchuk S N and Pewes D B.
A velocity correlation method for measuring vascular compliance using MR imaging
Magn. Reson. Imaging 5 628-34 (1995)
- [41] Valerinova D.
Experimental Measurement of the Mechanical Properties of Arteries.
4th Int Conf on Hemodynamics Mexico City (1998)
- [42] Vlaardingerbroek M T and den Boer J A.
Magnetic Resonance Imaging.
Springer Berlin (1995)
- [43] Wright J S, Cruickshank J K, Kontis S, Dore C and Gosling R G.
Aortic compliance measured by non-invasive Doppler ultrasound: description of a method and its reproducibility.
Clin. Sci. Colch. 78 463-8 (1990)

Acknowledgement

First I would like to thank Prof. Dr. Dr. Christoph Cremer for representing my work at the faculty for physics and astronomy. He also supported my admission to the 'Graduiertenkolleg Tumordiagnostik und -Therapie unter Einsatz dreidimensionaler radiologischer und lasermedizinischer Methoden' from the DFG which made this work possible.

I cannot begin to fully express my gratitude toward my supervisor, Prof. Dr. Lothar Schad, whose knowledge and personality have truly been inspirational. His support and his patience have given me the freedom to work scientifically. He also attentively reviewed this work and gave me a lot of helpful suggestions.

I would like to thank Prof. Dr. Schlegel and Prof Dr. Bille for admission to the 'Graduiertenkolleg' and Susanne Schmid for the wonderful organization. Prof. Dr. van Kaick offered me a vacancy and additional financial support. I am very thankful to him. I am very grateful to Dr. Jan Boese for his great support during my work. He supplied many engaging ideas and always had a solution to any scientific problem. I have enjoyed the many discussions I have had with Andre Bongers. I think I have learned the most about MRI from these. He also reviewed this work very attentively and gave me a lot of ideas. Also, Dr. Achim Bankamp, made great effort in reviewing this work and in helping me to organize it. Furthermore, Peter Siegler examined very precisely my work. I am very thankful for their support. I learned very much from the discussion with Hanno Scharr from the IWR in Heidelberg, as well as from Tobias Kunert and Dr. Andreas Mahr from the DKFZ. I am very grateful for their ideas concerning image processing problems in my work. I am very thankful to Tessa Wegener and Kate Lawson from the USA who transformed my work from 'disco-English' into a masterpiece of literature and thus saved my reputation. Last, but not least, I want to thank the entire MR group in the DKFZ for the cooperative and friendly working environment.

